Chair of Physics

Doctoral Thesis

Single Crystalline 2D Material Nanoribbon Networks: Optical and Electrical Properties

March 15, 2024

M. Awais Aslam

MONTANUNIVERSITÄT LEOBEN
www.unileoben.ac.at

AFFIDAVIT

I declare on oath that I wrote this thesis independently, did not use any sources and aids other than those specified, have fully and truthfully reported the use of generative methods and models of artificial intelligence, and did not otherwise use any other unauthorized aids.

I declare that I have read, understood and complied with the "Good Scientific Practice" of the Montanuniversität Leoben.

Furthermore, I declare that the electronic and printed versions of the submitted thesis are identical in form and content.

Date 09.03.2024

Signature Author
Muhammad Awais Aslam

I’m not super. Any talents I have, I worked for – it seems a long time since I thought of myself as a hero.

Oliver Queen

For my parents Asifa and Aslam.

For my siblings Aysha, Mydda and Bilal.

For my wife Famia.

For science. For survival.

ACKNOWLEDGMENTS

This thesis is a result of many joint efforts and would not have reached this scientific level without the ample assistance from many people. I am grateful to all these people with whom I got a chance to work. The following list is just an attempt to thank few of them.

I would like to thank *Christian Teichert* for his constant motivation and support during my time at Montanuniversität. He trusted in my capabilities and advised me at critical junctures. Apart from his enthusiasm for science, his compassionate nature towards the sufferings of humans around the globe will always be inspiring for me.

I am grateful to *Raul Rodriguez* for always reviewing my work critically and providing me with essential feedback. Also for his wise words during his visit to Leoben which helped me keep a work-life balance.

I would also like to thank ”Captain”, *Markus Kratzer*, for being a constant companion in all aspects of my PhD. I am grateful for his support for both scientific and personal matters. If all PhD students could have a ”Markus” in their life, nobody would leave a PhD mid-way. I am also grateful to all the members of Chair of Physics especially *Oskar Paris* for always lending his support in all technical and administrative matters.

I am glad that I had the companionship of friends like *Zubair* and *Abbas* who have been the source of many laughters during my rainy days in Leoben.

Last but not least, I am highly indebted to *Aleksandar Matkovic* without whose supervision, help and guidance this work would have not been possible. He provided me with the freedom to learn and grow as a researcher and helped me mature as a scientist. He always patiently listened to my questions which at times had no substantial meaning - I always realized later. His attitude towards science gave me the confidence to pursue and solve challenging research questions. I am grateful that God gave me a guide and teacher every PhD student dreams of.

My deepest gratitude goes to my parents *Asifa and Aslam*, thank you for all your prayers

and for always having my back. No words will ever be sufficient to express my gratitude towards you.

Finally, thank you, *Famia* for always being by my side through thick and thin, without you this would have not been possible.

TABLE OF CONTENTS

Acknowledgments vi

List of Abbreviations x

Abstract xii

Kurzfassung xiv

Chapter 1: Introduction 1

1.1 2D materials 1

1.2 Nanoribbons of 2D materials 3

1.3 Potential of 2D material nanoribbons in various fields 5

Chapter 2: Fabrication pathways for 2D material nanoribbons 10

2.1 Bottom-up Methods 10

2.1.1 Chemical Synthesis 10

2.1.2 Ledge Dependent Epitaxy (LDE) 11

2.1.3 Vapour Liquid Solid (VLS) growth 11

2.2 Top-Down Methods 12

2.2.1 Electron Beam Lithography 12

2.2.2 Unzipping nanotubes 12

Chapter 3: Methodologies 14

3.1 2D Material Exfoliation and Growth 14

3.1.1 Exfoliation 14

3.1.2 Chemical Vapor Deposition 15

3.2 Hot Wall Epitaxy 15

3.2.1 6P Nanoneedle formation 17

3.3 Reactive Ion Etching 18

3.4 Atomic Force Microscopy 19

3.4.1 Kelvin Probe Force Microscopy 21

3.5 Raman spectroscopy 22

3.6 Electrical characterization 25

Chapter 4: Summary and conclusion 28

References 35

Chapter 5: Publications 46

5.1 Single-crystalline nanoribbon network field effect transistors from arbitrary two-dimensional materials 46

5.2 The Crucial Role of Collective Water Molecule Dynamics in a Graphene Nanoribbon Switch 57

5.3 All van-der-Waals semiconducting $PtSe_2$ field effect transistors with low contact resistance 66

5.4 Multi–layer palladium diselenide as a contact material for two–dimensional tungsten diselenide field–effect transistors 75

5.5 List of co-author publications 90

LIST OF ABBREVIATIONS

AFM Atomic Force Microscopy

BEoL Back End of Line

CVD Chemical Vapor Deposition

CMOS Complementary Metal Oxide Semiconductor

CIPS $CuInP_2S_6$

DHTA7 dihydrotetraazaheptacene

DFT Density Functional Theory

FETs Field Effect Transistors

Gr NRs Graphene Nanoribbons

hBN Hexagonal Boron Nitride

HWE Hot wall epitaxy

I_D Drain Current

IRDS International Road map for Devices and Systems

KPFM Kelvin Probe Force Microscopy

LDE Ledge Dependent Epitaxy

ML Monolayer

MoS_2 Molybednum Disulphide

PDMS Poly-dimethylsiloxane

$PtSe_2$ Platinum Diselenide

TMDCs Transition Metal Dichalcogenides

VLS Vapour Liquid Solid

VLSI Very Large Scale Integration

V_{DS} Drain Source Voltage

V_{SG} Source Gate Voltage

WSe_2 Tungsten Diselenide

2D Two-dimensional

2D-FFT 2D Fast Fourier Transform

6P para-hexaphenyl

Abstract

Two-dimensional (2D) material nanoribbons offer vast opportunities ranging from next-generation quantum electronics to enhanced sensing. However, the existing fabrication routes are mostly restricted to graphene nanoribbons where the majority of methods rely on solution processed nanoribbons which hinders their integration into devices. Methods opted for the fabrication of other 2D material nanoribbons do not offer sufficient quality, yield and control over the nanoribbons' edge terminations. This has been a bottleneck in the experimental studies of nanoribbons to explore their electrical and optical properties.

This work aims to propose a universal approach to synthesize networks of nanoribbons from arbitrary 2D materials while maintaining high crystallinity, narrow size distribution, and straightforward device integrability. Moreover, the resulting devices do not suffer from junction resistance issues. This is supported by *in-operando* Kelvin Probe Force Microscopy of nanoribbon field effect transistors (FETs). The single crystalline nature of the nanoribbons is verified by Raman spectroscopy. By relying on self-aligning organic nanostructures as masks, the possibility of controlling the predominant crystallographic direction of the nanoribbon's edges is also demonstrated. Electrical characterization shows record charge carrier mobilities and very high ON-currents despite extreme width scaling.

Particularly, for graphene nanoribbons a well-defined and highly controllable system of hexagonal boron nitride encapsulated graphene nanoribbon networks with water terminated edges is also presented. The system exhibits a robust hysteresis of the remnant dipolar fields, which affect and modulate the conductivity of graphene nanoribbon networks. So far, such ambipolar behaviour in graphene nanoribbons has been only predicted theoretically. The undertaken experimental approach sheds light on the mechanisms governing the ferroelectric behavior in graphene nanoribbons and supports it theoretically via molecular dynamic simulations. This offers insights for the design of ferroelectric heterostructures and neuromorphic circuits.

The thesis also presents studies on two emerging 2D materials namely, $PtSe_2$ and $PdSe_2$ for the integration into all van-der-Waals semiconducting FETs with high-performance transport characteristics. $PtSe_2$ is proposed as an alternative channel material below thicknesses of 4 nm, a critical thickness limit below which Si electronics performance start to deteriorate. Whereas, $PdSe_2$ is proposed as an electrode material for p-type WSe_2 FETs. The work is inspired by the need to address the challenges faced for the co-integration of 2D materials into back end of line processes used in Silicon technology.

Kurzfassung

Zwei-dimensionale (2D) Nanobänder bieten enorme Möglichkeiten, die von der nächsten Generation der Quantenelektronik bis hin zu verbesserter Sensorik reichen. Allerdings sind die bestehenden Herstellungswege jedoch meist auf Graphen-Nanobänder beschränkt, wobei die meisten Methoden auf der Verarbeitung von Nanobändern in Lösung beruhen, was ihre Integration in Bauelemente erschwert. Methoden, die für die Herstellung von Nanobändern aus anderen 2D-Materialien gewählt wurden, bieten keine ausreichende Qualität, Ausbeute und Kontrolle über die Kantenzustände. Dies war bisher ein Engpass bei den experimentellen Untersuchungen von Nanobändern zur Erforschung ihrer elektrischen und optischen Eigenschaften.

Ziel dieser Arbeit ist es, einen universellen Ansatz zur Synthese von Nanoband-Netzwerken aus beliebigen 2D-Materialien vorzuschlagen aus unter Beibehaltung hoher Kristallinität, enger Größenverteilung und einfacher Integrierbarkeit in Bauelemente. Darüber hinaus die unterliegen Bauelemente nicht mehr Widerstandsproblemen. Dies wird durch die in-operando Kelvin Probe Force Microscoie von Nanoband-Feldeffekttransistoren (FETs). Belegt Die einkristalline Natur der Nanobänder wird durch Raman-Spektroskopie verifiziert. Durch die Verwendung von selbstausrichtenden organischen Nanostrukturen selbstausrichtenden organischen Nanostrukturen als Masken ist es möglich, die vorherrschende kristallografische Richtung der Kanten der Nanobänder zu steuern, wie ebenfalls demonstriert wird. Die elektrische Charakterisierung zeigt Rekord beweglichkeiten der Ladungsträger und sehr hohe ON-Ströme trotz extremer Breitenskalierung.

Insbesondere für Graphen-Nanobänder wird ein wohldefiniertes und gut kontrollierbares System mit hexagonalen Bornitrid-verkapselten Graphen-Nanoband-Netzwerken mit wasserterminierten Kanten vorgestellt. Das System weist eine robuste Hysterese der verbleibenden dipolaren Felder auf, die Leitfähigkeit von Graphen-Nanoband-Netzwerken beeinflussen und modulieren. Bislang wurde ein solches ambipolares Verhalten in Graphen-

Nanobändern bisher nur theoretisch vorhergesagt. Der unternommene experimentelle Ansatz wirft ein Licht auf die Mechanismen, die das ferroelektrische Verhalten in Graphen-Nanobändern bestimmen und unterstützt es theoretisch durch molekular-dynamische Simulationen. Dies bietet Erkenntnisse für das Design ferroelektrischer Heterostrukturen und neuromorpher Schaltungen.

In dieser Arbeit werden auch Studien zu zwei neuen 2D-Materialien, nämlich $PtSe_2$ und $PdSe_2$, vorgestellt, die sich für die Integration in alle van-der-Waals Halbleiter Feldeffekttransistoren (FET) mit leistungsstarken Transporteigenschaften. $PtSe_2$ wird als alternatives Kanalmaterial unterhalb einer Dicke von 4 nm vorgeschlagen, einer kritischen Dicke, unterhalb derer die Leistung von Si-Elektronik zu verschlechtern. $PdSe_2$ hingegen wird als Elektrodenmaterial für p-Typ WSe_2-FETs vorgeschlagen. Die Arbeit wurde durch die Notwendigkeit inspiriert, die Herausforderungen zu bewältigen, die sich bei der Ko-Integration von 2D-Materialien in Back-End-of-Line-Prozesse, die in der Siliziumtechnologie verwendet werden.

CHAPTER 1
INTRODUCTION

1.1 2D materials

The concept of two-dimensional (2D) materials, composed of a single layer or few atomic layers, was catalyzed by the discovery of graphene – a one-atom-thick layer of carbon arranged in a hexagonal lattice [1]. Geim and Novoselov introduced a simple yet elegant way of isolating single layers of 2D materials by using micromechanical exfoliation the so called the scotch tape method. Since then, a rich variety of 2D materials have been unveiled, including Transition Metal Dichalcogenides (TMDCs) like Molybednum Disulphide (MoS_2) and Tungsten Diselenide (WSe_2), among others. In the field of nanoscale science and engineering, 2D materials have played an essential role in laying down the foundations for the ”age of nanotechnology”. From cancer immunotherapy [2] to quantum processes [3, 4], 2D materials are expected to have a pronounced influence on different fields of science for the times to come.

These materials possess extraordinary electronic, mechanical, thermal, and optical properties that differ from their bulk counterparts. These properties open up possibilities in nanophotonics [5, 6], energy efficiency [7, 8], spintronics [9, 10] and nanoelectronics [11, 12], to name a few. In nanoelectronics, 2D materials are expected to lead the extension of the scaling law (Moore’s law) by allowing channels to be scaled to single atomic thicknesses. This is not possible with Si as its performance deteriorates below 4 nm [13]. In this regard, the recent version of the International Road map for Devices and Systems (IRDS) lists two-dimensional (2D) materials as probable candidates for standard Complementary Metal Oxide Semiconductor (CMOS) technology in the coming years [14].

Figure 1.1 shows a time line of major works done during the past decade related to 2D

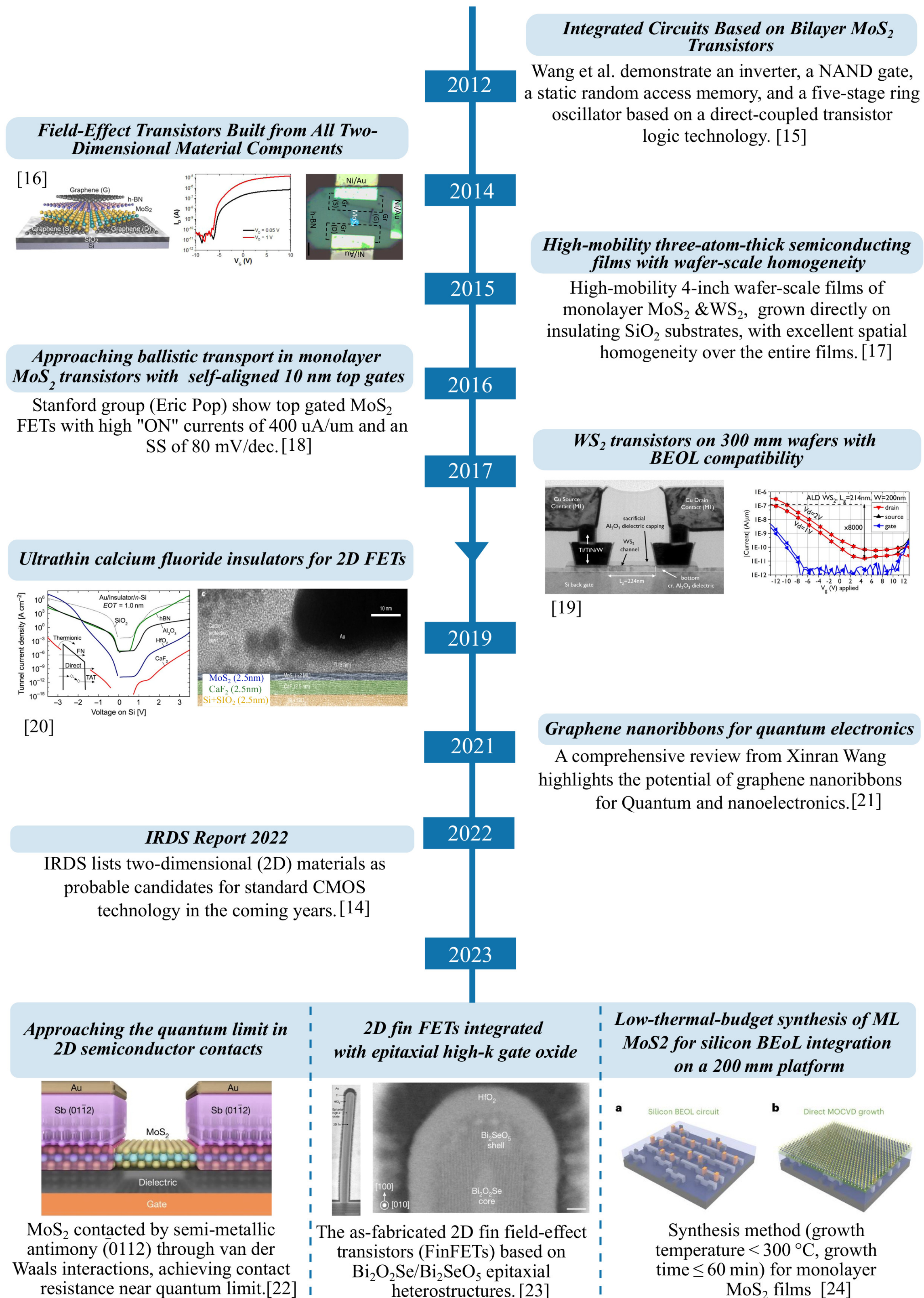

Figure 1.1: Time line for the evolution of 2D material based nanoelectronics during the last decade. Compiled from: [14–24]

materials which have helped further the cause for the integration of 2D materials in nanoelectronics. Intensive efforts have been made in the last decade to make the 2D material based very large-scale integration (VLSI) technology a reality. However, high contact resistances [25, 26] and growth temperatures [27, 28] are the foremost challenges hindering the co-integration of 2D materials into CMOS technologies. Although, contact engineering methods [22, 29–31] and doping techniques [32, 33] have helped to approach the quantum limits of contact resistance for various monolayer TMDCs, yet their integration is limited by the high growth temperatures which are not compatible with the back end of line (BEoL) processes [28, 34]. Therefore, a semiconducting 2D material is needed which overcomes both of the challenges listed above. To bridge this gap, the work of this thesis highlights the potential of $PtSe_2$ in this regard. The work is represented in the "Publications" section as the third publication titled *"All van-der-Waals semiconducting $PtSe_2$ field effect transistors with low contact resistance"*.

However, not only the device dimensions are expected to shrink further to keep Moore's alive. There is also an urgent need to employ materials which offer unique properties essential for quantum electronics, neuromorphic computing, ferroelectricity and enhanced sensing capabilities. These properties have been predicted to be a hallmark of atomically thin strips of 2D materials, namely nanoribbons.

1.2 Nanoribbons of 2D materials

Nanoribbons are typically few atoms thick, with their widths restricted below a few hundred nanometers. The field of 2D material nanoribbons has been mainly driven by the need to fabricate graphene nanoribbons (Gr NRs). Although graphene offers exceptional mobilities and conductive properties however, an absence of band gap makes it impossible to be used in logic circuits. An energy gap can be induced in graphene due to quantum confinement and edge effects. While fulfilling the stringent requirement of device sizes, Gr NRs present an optimal platform with reduced widths but sufficient lengths to be integrated into

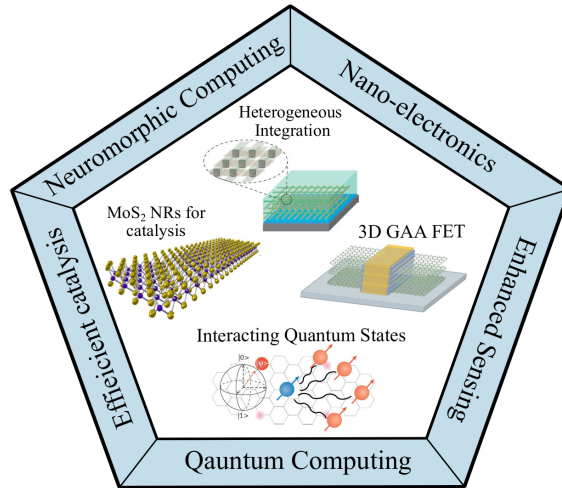

Figure 1.2: Wide range of applications for nanoribbons. The icons inside the schematic are adopted from [21].

electrical applications.

This was first shown theoretically in 2006 by Son et al. [35]. They demonstrated through ab-initio calculations that the edges and quantum confinement effects are responsible for the creation of band gaps in Gr NRs with armchair-shaped edges. Contrarily, for zig-zag edges the band gap is a result of staggered sublattice potential on the hexagonal lattice caused by edge magnetization [35].

The first experimental demonstration of an induced band gap was done in 2007 by Han et al. [36] by lithographical patterning of graphene into nanoribbons. Gr NRs also allow various functionalities including long mean free path, localized spin and topological edge states. Therefore, successful synthesis of Gr NR and their implementation in devices has brought them at the forefront as building blocks for information processing in quantum and classical electronics [21].

Owing to the exotic properties offered by the graphene nanoribbons, the scientific community has placed great efforts for the studies of other 2D material NRs as well. Figure 1.2 shows a schematic illustration of the various applications and functionalities offered by 2D materials. This has lead to the observations of ferromagnetism [37, 38] and efficient

catalysis [39, 40]. Moreover, a recent study [41] has shown an induced band gap in hexagonal boron nitride (hBN) nanoribbons due to the adsorption of water on the edges. This also highlights the strong influence of edge termination on the bulk properties of nanoribbons and can be used as a harnessing tool to tune the properties of nanoribbons of different materials.

The following section enlists the prospects of 2D material nanoribbons in various fields.

1.3 Potential of 2D material nanoribbons in various fields

Nanoelectronics: Apart from the aspect of miniaturization, nanoribbons can allow the integration of heterostructures in atomically precise nanoelectronics [42, 43]. They are also important as they can offer high degree of electrostatic control and therefore, low power consumption. NRs with widths of few nanometers are expected to exhibit high mobilities of up to 100 cm^2/Vs [44].

Sensors: With ever increasing needs for real time, fast response and high sensitivity sensors nanoribbons can provide the ideal platform. Various studies have been undertaken in this regard to utilise the critical aspect ratios of NRs. High surface area to volume ratio and large number of edges provide an ideal platform for the gases, volatile organic compounds and biological sensing [45–47]. Furthermore, 2D materials can be selectively functionalized to offer multi-analyte binding sites. In 2021, Zhao et al. demonstrated wafer-scale nanoribbon bio-sensors with high sensitivity for a broad range of biological targets [47]. The overview presented in the figure 1.3 highlights a wide range of sensing capabilities of 2D material nanoribbons.

Quantum Transport Phenomena: Gr NRs are particularly promising for creating topological states and managing quantum coherence. This is due to the negligible contribution of spin-orbit coupling and hyperfine interaction which are the primary sources of decohorence in Gr NRs systems. Secondly, it is possible to fine-tune the bandwidth of the topological electronic band at the energy scale of proximity-induced spin-orbit coupling.

2D material Nanoribbon	Type of Sensor	Reference
Gr	N_2, Alcohols	[46]
In_2O_3	Serotonin	[47]
MoS_2	NO_2, NH_3	[48]
Gr	Volatile Organic Compounds	[49]
MoS_2	DNA Sequencing	[50]

Figure 1.3: Gas sensing applications for 2D material nanoribbons. [46–50]

Spin-polarized edge states of zigzag-oriented Gr NRs and topological boundary states at Gr NRs junctions can both be crucial components of quantum information systems. Third, once created, Gr NRs quantum states may be easily combined with other 2D materials to form multi-qubit architectures [21].

Zhang et al. [51] have shown that quantum phenomena such as Coulomb blockade, excited states of vibrational origin and Franck-Condon blockade can be observed in graphene nanoribbons. The authors achieved this by contacting individual graphene nanoribbons by carbon nanotubes highlighting the immense potential of nanoribbons for integration into large scale systems. Apart from graphene nanoribbons, several studies [52, 53] have also demonstrated the potential of MoS_2 NRs for spintronics and quantum transport via the observation of coloumb blockade phenomena up to 60 K (see Figure 1.4).

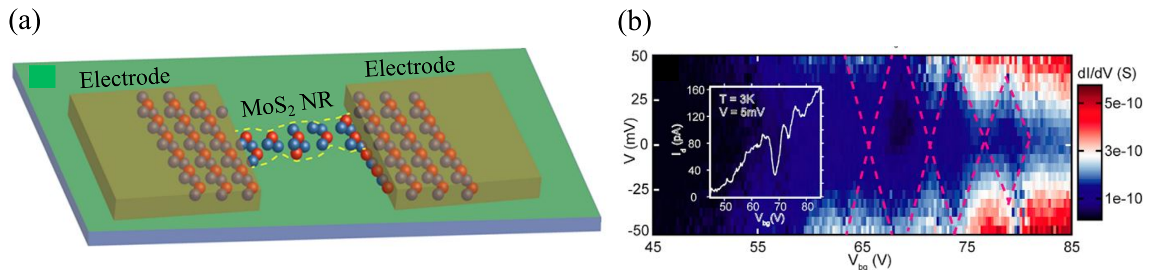

Figure 1.4: (a) Schematic representation of a MoS_2 NR device. (b) shows the observation of characteristic "coloumb diamonds" in the conductance plot at 3K. The phenomena can be attributed to strong influence of rough edges on the channel. The figure is adopted from Ref. [53].

Ferroelectricity: The field of 2D-material ferroelectricity holds great promise for the realization of neuromorphic computing, nonvolatile random access memory storage systems and memcapacitors [45, 54, 55]. However, studies experience various challenges. The foremost is to find 2D materials which exhibit robust intrinsic ferroelectricity at room temperature down to one atomic layer. In this regard, distorted $MoTe_2$ [56] has been the stand out candidate as it fulfils both the criteria of few atom thickness as well as temperature tolerance. However, its lack of air stability is a big obstacle for integration into devices [57]. Many other systems have also been explored as gate tunable platforms but they employ ferroelectric substrates such as perovskite oxides to induce bi-stability in van der Waal materials. This not only increases the thickness of the system but also leads to uncontrolled and unintentional doping which can be detrimental towards the device properties [58]. In addition, existing ferroelectric perovskites do not show polarization effects below a critical thickness which hinders their usage in nanoelectronics of the future [59].

Similarly, many of the 2D materials discovered for ferroelectricity have Curie temperatures above or below room temperature [60–63]. This undermines their importance as most of the target applications are expected to operate at ambient. In this regard, $CuInP_2S_6$ (CIPS) has recently emerged as a very promising candidate exhibiting room temperature ferroelectricity, yet its whole principle for ferroelectricity depends upon migration of Copper ions. This can have serious implications with regards to applications as this results in a change of volume and topography [64]. Amidst all these options, twisted 2D material stacks have presented themselves as an interesting platform for ferroelectricity [65–67]. However, the understanding of such systems is only at a nascent stage and involves making stacks of 2D materials which can be upto 50 nm thick [65].

Considering the challenges presented above, Gr NRs can be the ideal candidates. However, ferroelectricity in Gr NRs has only been predicted theoretically. Jose et al. predicted a hysteretic behavior via Density Functional Theory (DFT) calculations to occur for confined systems such as Gr NR once they are terminated via polar molecules [68].

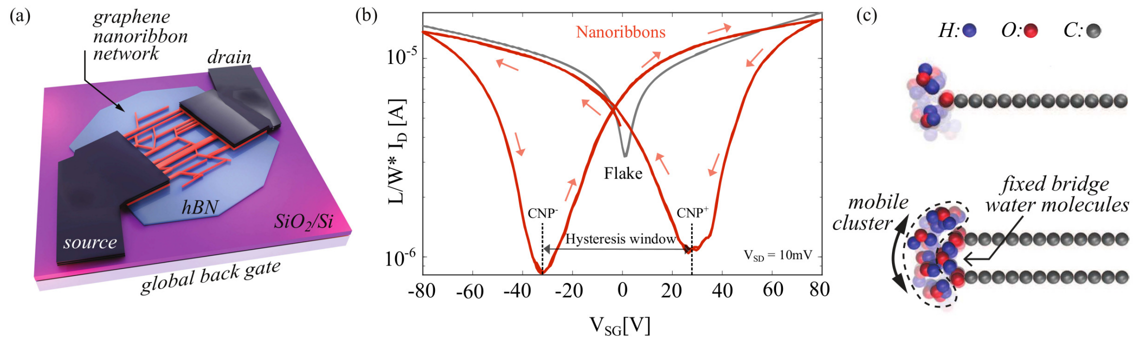

Figure 1.5: (a) Schematic representation of nanoribbon filed effect transistor. (b) Semi-log scale of the same monolayer graphene device before and after being patterned into the network of nanoribbons. The measurements were carried out at 300 K in vacuum, and two subsequent sweeps are presented. I_D (Drain current) is normalized with respect to the length (L) over width (W) ratio of the nanoribbon network. (c) MD simulation models exhibiting typical local configuration of water clusters in absence of the external electric field for a mono and bi-layer graphene FET. Adopted from author's publication number 2.

The confirmation to this phenomena is experimentally shown by the author in the publication number 2 of the thesis titled *"The Crucial Role of Collective Water Molecule Dynamics in a Graphene Nanoribbon Switch"* where water induced ferroelectricity in Gr NRs has been reported. The results are further supported by complex molecular dynamic simulations. A well defined and highly controllable system of hBN encapsulated Gr NR networks with water terminated edges was investigated (see Figure 1.5). The system exhibits a robust hysteresis of the remnant dipolar fields, which affect and modulate the conductivity of Gr NR networks. We have observed an unusual behaviour, namely, the hysteresis window appears to be temperature independent in a large and technology relevant range, only if the ribbons are having bi-layer or thicker graphene stacks. This is attributed to a collective behaviour of water dipoles, enabled by the "bridge" molecules that adsorb between the two layers. With large-scale molecular dynamics simulations, key features observed in the experiments were replicated. The study proposes that the molecules can collectively stay bound in one state by intermolecular Coulomb interactions, yielding a ferroelectric effect that is not thermally activated.

Considering the wide range of technological relevance in various fields, there is a need

to devise a universal method for the fabrication of 2D material nanoribbon networks which offers:

(i) Sufficient quality,

(ii) Narrow widths,

(iii) High density,

(iV) Controlled over the edge termination and

(v) High yield .

The following chapter provides a brief overview of the methods widely used to fabricate nanoribbons with potential advantages and disadvantages.

CHAPTER 2

FABRICATION PATHWAYS FOR 2D MATERIAL NANORIBBONS

There are two main methods related to the fabrication of 2D material nanoribbons. These can be divided into either bottom-up or top-down approaches depending on the type of the fabrication method. The section below highlights the pathways and their pros and cons.

2.1 Bottom-up Methods

2.1.1 Chemical Synthesis

Chemical synthesis of NRs offers precise edge control and widths down to few atomic units can be realized. The reactions are thermally activated on Au (111) surface involving intramolecular cyclohydrogenation of polyenylene polymers [69]. The reaction steps are carried out in ultra high vacuum conditions. The schematic in Figure 2.1 shows a representation of the reaction steps involved in the fabrication of graphene nanoribbons.

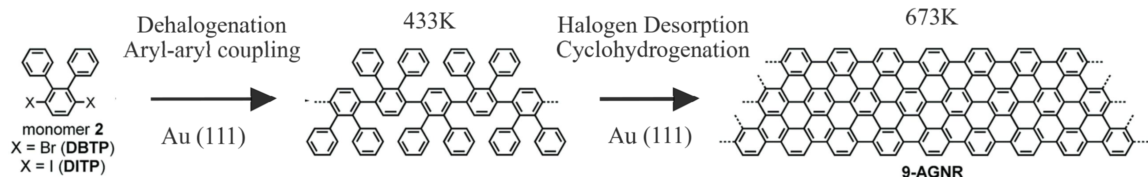

Figure 2.1: Steps involved in the chemical synthesis of graphene nanoribbons. The figure is adopted and modified from reference [69].

The integration of such solution processed nanoribbons in devices is a challenge which results in low yields and precise control of the channel. Moreover, the synthesized NRs need to be transferred from the metal substrate to a substrate relevant to the device architecture such as Si or hBN. Moreover, chemical synthesis routes focus almost exclusively on Gr NRs, facing significant obstacles to develop more complex 2D materials or NR het-

erostructures. The device channels also suffer from electrical percolation issues and high junction (node) resistance.

2.1.2 Ledge Dependent Epitaxy (LDE)

LDE utilises the possibility of a 2D material growth to be oriented by the substrate that is used. Recently, Aljarb et al. have shown chemical vapor deposition asssited vicinal epitaxy of MoS_2 nanoribbons [70]. It is critical to have thermodynamic control of TMDC seeding orientation and as well as kinetics of growth. The schematic representation in Figure 2.2 shows the synthesis route adopted.

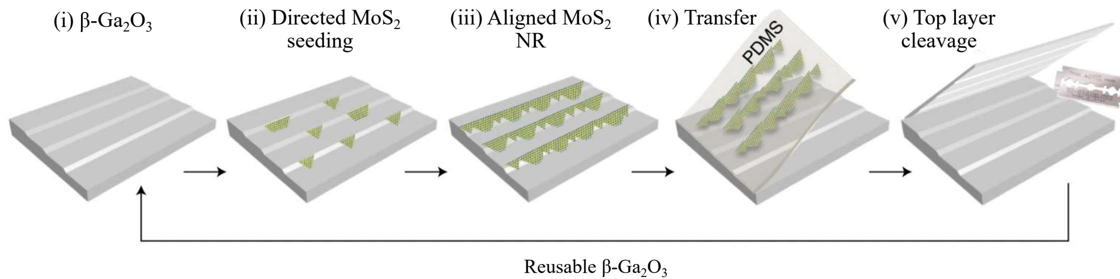

Figure 2.2: (a) A schematic representation of LDE. The figure is adopted from reference [70].

Although, the NRs produced by this approach are single crystalline, the ribbon widths are rather large and non-uniform. The growth of these ribbons is also dependent on specific substrate, requiring an additional transfer step for their integration into device architectures [71].

2.1.3 Vapour Liquid Solid (VLS) growth

VLS method produces one dimensional (1D) nanostructures by precipitation from supersaturated catalytic liquid droplets. Previously, it has been used by the scientific community to synthesize Si or SiGe nanowires. Van der Waals layered compounds such as hBN [72], SnS_2 [73] and Bi_2Se_3 [74] have also been grown by VLS mode. The growth products are

frequently arbitrarily oriented multilayered nanotubes or nanoribbons, typically made up of tens to hundreds of monolayers. It offers very little thickness control for the grown 2D material [75].

Recent reports [52, 75] have demonstrated VLS growth of mono and bilayer MoS_2 NRs on freshly cleaved NaCl single crystal and SiO_2, respectively. The widths achieved ranged from hundreds of nanometers to a few nanometers. Although, the direct growth of NRs on SiO_2 is promising the use of salt and metal precursors can be detrimental for the device fabrication where clean surfaces are required to pattern or transfer metal electrodes. Moreover, an inhomogeneous thickness is obtained along the length of the nanoribbon.

2.2 Top-Down Methods

2.2.1 Electron Beam Lithography

Lithography is a widely used technique to pattern at the nanometer scale. Several lithography approaches have been employed in quest to achieve 2D material NRs with widths of few hundred nanometers. These methods include scanning probe lithograpy and e-beam lithography [76, 77]. Lithography offers a significant advantage over other methodologies with regards to its applicability as it can be employed on all kinds of 2D materials. However, it does not offer a straight forward control over NR's alignment with respect to high symmetry directions of the 2D material. They also cause interface contamination degrading device performance and operation [71].

2.2.2 Unzipping nanotubes

Unzipping of nanotubes to form nanoribbons of graphene was first shown in 2009. In the following years it was successfully applied for hBN and WSe_2. The Figure 2.3 shows a representation of processing parameters and the resulting NR formed [78]. It is evident that isolating NRs from the solution would require further processing and can result in an extremely low yield. This makes their usage limited to solution based processes and

applications. The process also depends on the availability of nanotubes of a particular 2D material to synthesize NRs form it. This is critical for hBN as significant difficulties are involved in the BN nanophase synthesis which is essential for NR formation. Unlike chemical synthesis, the control of edges and width of the nanoribbons in the unzipping method is also challenging.

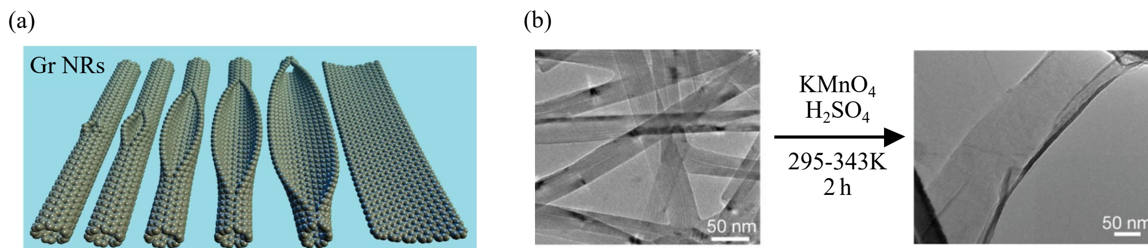

Figure 2.3: (a) A schematic representation of unzipping of multiwalled carbon nanotubes to form nanoribbons (b) Chemical processing steps and temperatures required. The figure is adopted from reference [77].

To address the challenges associated to nanoribbon fabrication, the work of my thesis presents a nanoribbon fabrication method which is based on the growth of small conjugated organic molecules in the form of crystalline needles on 2D materials. The needle-like crystals follow discrete crystallographic directions of the 2D material [79–81]. It is applicable to a wide range of 2D materials and also allows the fabrication of heterostructure nanoribbons e.g., MoS_2/WS_2. The resulting NRs are optically and electrically characterized. The work is represented in the ”Publications” section as the first publication titled *”Single-crystalline nanoribbon network field effect transistors from arbitrary two-dimensional materials”*.

The following chapter details the methodologies used to fabricate and characterize the nanoribbons produced by the pathway opted by the author.

CHAPTER 3
METHODOLOGIES

3.1 2D Material Exfoliation and Growth

2D materials on silicon (Si-SiO_2) substrates were obtained by both, chemical vapor deposition (CVD) as well as exfoliation. CVD was in particular used to demonstrate the control over the orientation of the predominant NR direction [71]. As this can be verified by using triangular CVD grown MoS_2 flakes that terminate with zig-zag edges due to the growth kinetics [82, 83].

3.1.1 Exfoliation

Mechanical exfoliation has been the most popular and easily accessible method since last 15 years. It allows to obtain monolayer 2D material flakes from bulk crystal as it is straightforward, and the products have high crystal quality [71]. Moreover, it allows the fabrication of heterostructures of 2D materials.

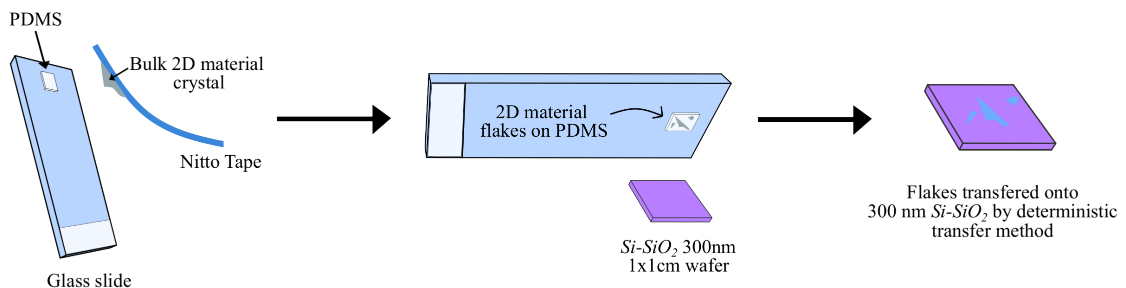

Figure 3.1: 2D material transfer process.

The method involves transfer of bulk crystals from the scotch tape to the Poly-dimethylsiloxane (PDMS). The 2D material flakes obtained on PDMS can then be controllably transferred to the substrate of choice. During the course of the thesis, various substrates were used such

as highly oriented pyrolitic graphite, thin films of gold and Silicon with a 300 nm oxide. The Figure 3.1 shows the schematic for the transfer of 2D material flakes from scotch tape to Si substrate. For most of the studies, 300nm Si-SiO_2 was the substrate of choice as it allows the identification of monolayers of 2D materials relatively easy under the optical microscope due to color contrast [84, 85].

3.1.2 Chemical Vapor Deposition

CVD is a method that produces high-quality MoS_2 flakes with uniform morphology and controllable size by the chemical reaction between molybdenum and sulfur sources at suitable temperature and gas flow.

The method involves the growth of triangular MoS_2 flakes from solution-based molybdenum precursor at atmospheric pressure similarly to the procedure in reference [86]. The liquid molybdenum source was drop casted and the substrate was then placed in a sulfur atmosphere. The liquid Mo precursors used were NaMo (sodium molybdate) and AHM (ammonium heptamolybdate) in 1:1 ratio and dissolved in ultra-pure water at concentration of 200 ppm.

3.2 Hot Wall Epitaxy

Hot wall epitaxy (HWE) is classified as a type of thermal evaporation technique where the source material transforms into a gaseous phase while increasing in vapor pressure. It allows the epitaxial growth to take place near thermodynamic equilibrium. In high-vacuum 10^{-7} mbar, the rate of the molecules leaving the source into the gas phase is controlled by the source oven (which is a separated heated quartz tube), while the energy of the molecules in the gas phase can be tuned by the temperature of the oven wall as shown in Figure 3.2. The substrates' temperature controls the surface diffusion of the adsorbed molecules [71]. HWE was selected as the technique of choice to grow organic semiconductor nanostructures namely, para-hexaphenyl (6P) and dihydrotetraazaheptacene

(DHTA7) [87].

By keeping the substrate temperature high (375 - 390 K) and the deposition rate low (0.5 Monolayer per hr) it is possible to achieve very large single-crystalline nanostructures, especially on van der Waals substrates. These organic nanostructures self assemble into networks of organic needles. Such a network then serves as a mask on top of 2D material flakes which can then be etched to form a single crystalline 2D material NR networks.

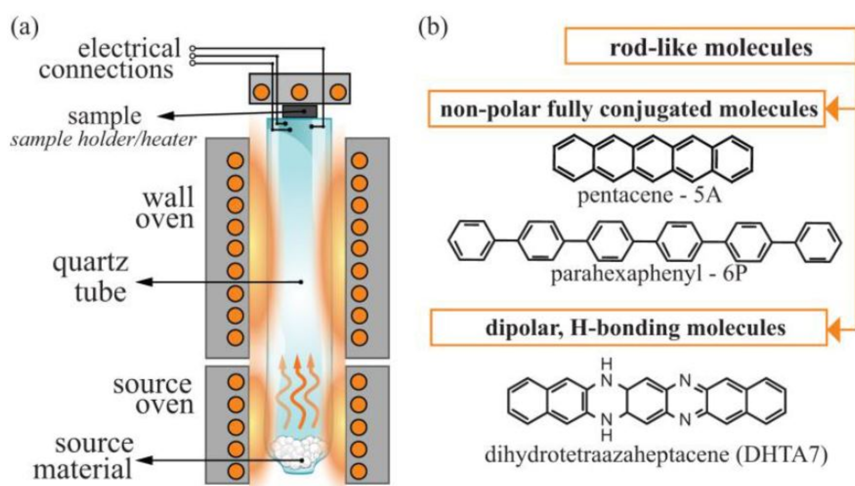

Figure 3.2: (a) Scheme of a HWE setup. (b) Different molecule types that can be used as source material for needle like growth.

The author targeted the growth of small rod-like molecules with either acene or phenylene based backbones as shown in Figure 3.2b. The organic molecules at the interface with the 2D material substrate adopt a flat-lying orientation and align their π-networks to optimize van-der-Waals interaction with the substrate [79, 88]. Consequently, the molecules at the interface are 'locked' into preferential adsorption sites on the substrate and the growing crystallites adopt rotational commensuration with their 2D material support [80]. This provides an inherent self-alignment with the substrates' high symmetry directions, i.e., armchair or zig-zag.

To show control of NRs predominant crystallographic orientation, two different organic molecules - (6P) and (DHTA7) - were grown on ML MoS_2 obtained by CVD. Their phenylene (6P) and acene (DHTA7) backbones correspond to armchair and zig-zag motifs,

respectively, and upon adsorption, molecular backbones will align with the corresponding high-symmetry directions of the 2D material substrate [81, 89, 90]. The control over the orientation of the predominant NR direction was verified by using triangular CVD MoS_2 flakes that terminate with zig-zag edges due to the growth kinetics [82, 83, 91]. The NR directions and the triangular MoS_2 flake-edge directions were compared by 2D Fast Fourier Transform (2D-FFT) analysis of the atomic force microscopy (AFM) topography images. In the case of 6P masks predominant NR directions were tilted by $(8.5 \pm 0.4)°$ from the edge directions, *i.e.,* edges of the resulting NRs are close to parallel with the zigzag crystallographic direction of the 2D material. By altering the backbone of the molecular mask (the case of DHTA7) the NR edges change predominantly following the armchair crystallographic direction [71]. The results are presented in the publication number 1 *"Single-crystalline nanoribbon network field effect transistors from arbitrary two-dimensional materials"*.

By further optimization of the growth time, etching time or selection of organic nanostructures based on shorter back bone (e.g., bi-phenylenes), the mean width of the resulting nanoribbon network can be controlled [71].

3.2.1 6P Nanoneedle formation

Graphene: 6P forms elongated needle like structures at elevated growth temperatures (360 K to 410 K) with the molecular long axes aligned parallel to graphene's zig-zag axes.

Whereas on amorphous or weakly interacting substrates such as SiO_2 it forms islands due to the molecules' long axes roughly oriented in an upright manner with respect to the substrate surface. This is shown in the AFM image in Figure 3.3. In the case of graphene the contact plane is 6P(2 0 -3) and for an island growth the low energy face 6P(001) is exposed [79].

hBN: Similar to graphene, 6P growth on hBN follows discrete growth directions due to the interfacial alignment between hBN and 6P molecules in the 6P(-6 2 9) plane. It was

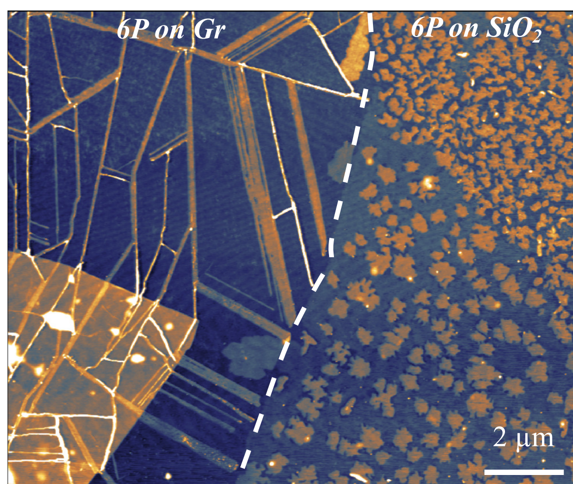

Figure 3.3: An AFM image of 6P on graphene and SiO_2 (*z-scale: 17 nm*).

found via DFT calculations that individual 6P molecules attach to the underlying substrate (hBN) with their long axes parallel to hBN's arm chair direction and their phenyl rings are centered on the nitrogen atoms. The growth then continues selectively in the direction perpendicular to the long molecular axes i.e. hBN's zigzag direction $\pm 6°$ [81]. The typical width of the needles realized method ranged from 10 nm to 100 nm.

3.3 Reactive Ion Etching

Reactive ion etching (RIE) is an anisotropic etching technique, meaning it etches in a directional manner, producing well-defined and controlled features. It is commonly used in the production of integrated circuits, microelectromechanical systems (MEMS), and other microfabricated devices. An Oxford plasma 80 plus system (available at PCCL, Leoben) was used during the works carried out in the scope of this thesis. It involves a stream of glow discharge (plasma) of an appropriate gas at the sample. Figure 3.4 shows a schematic representation of the process.

Particularly, for graphene and TMDCs oxygen precursor gas was used. As part of the procedure, the components of the material being etched react chemically with the reactive species produced by the plasma to produce volatile etch products at room temperature. hBN

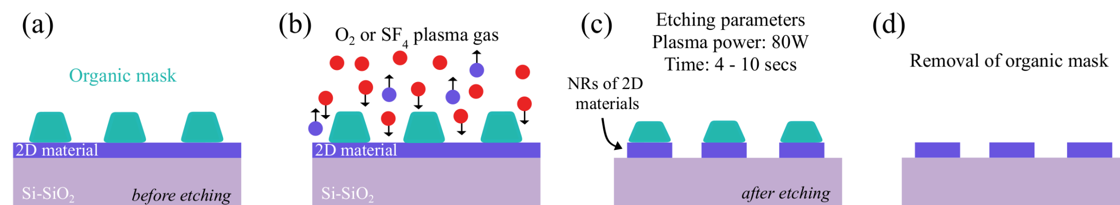

Figure 3.4: Schematics for the illustration of the etching process. (a) Configuration of the 2D material and organic mask stack. (b) Reactive ion etching process. (c) Nanoribbon formation due to the etching of exposed regions. (d) Removal of organic mask by annealing under high vacuum or rinsing in chloroform.

largely remains unaffected by the oxygen plasma. Therefore, sulfur tetraflouride (SF_4) precursor gas was used which reacts rapidly to etch it away. The plasma source, often referred to as the etch species, can either be neutral (atoms and radicals) or charged (ions). The etching experiments with (SF_4) were performed in the clean room facility of TU Wien (Institute for Solid State Physics) using Oxford plasma 80 plus system.

3.4 Atomic Force Microscopy

Atomic force microscopy (AFM) is a low-force experimental method that can characterize various surfaces at the nanoscale. It uses forces in the pN to μN range. A pointed tip at the end of a cantilever is used in the AFM method to scan a surface and measure its topography. The AFM's basic operating principle is shown in the Figure 3.5. In many commercial systems, the sample is scanned in the x and y directions while the cantilever is positioned at an angle of roughly 11 degrees in a holder that can operate only in the z direction. Piezo-actuators are used to make these x, y, and z-directional motions because they have sub-nm position precision.

The AFM typically operates in two modes namely contact and non-contact mode. As the probe approaches the surface, various intermolecular forces come into play. The most common forces include van der Waals forces, electrostatic forces, and chemical bonding forces. These forces cause the cantilever to deflect. The probe is typically made of silicon

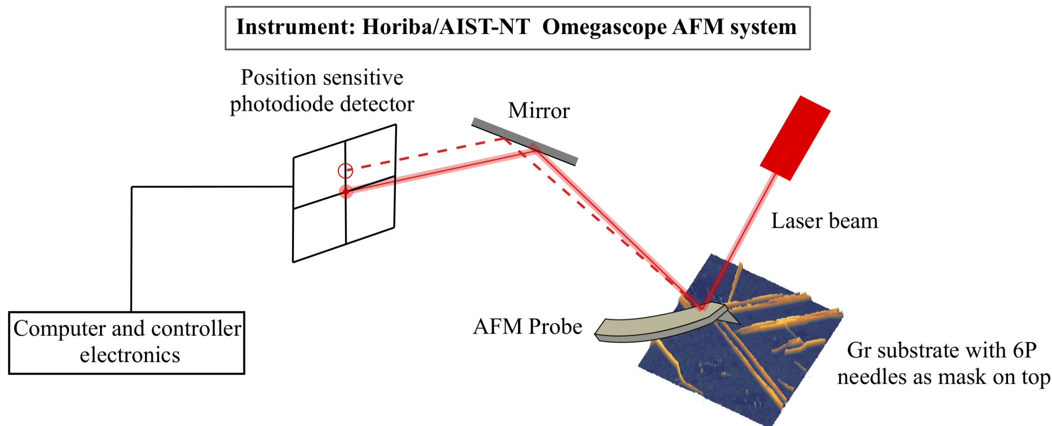

Figure 3.5: Schematic representation of the working principle of an atomic force microscope.

or silicon nitride and may have a sharp tip with a radius of just a few nanometers. For some AFM modes like Kelvin Probe Force Microscopy (KPFM) a conductive coating of a metal e.g. platinum is done on the tip.

The deflection of the cantilever is highly sensitive to the interaction forces between the probe and the sample. When the probe is close to the sample, the deflection of the cantilever changes in response to these forces. To maintain a constant force or set point between the probe and the sample, an electronic feedback loop is employed. The feedback loop adjusts the position of the probe vertically by moving the piezoelectric scanner, which holds the sample or the probe itself. The goal is to keep the cantilever deflection constant by adjusting the distance between the probe and the sample's surface. The deflection of the cantilever as it interacts with the sample's surface is monitored by a position sensitive photodiode detector. The setup involves directing a laser beam onto the back of the cantilever and positioning a photodiode to capture the reflected laser light. When the cantilever deflects due to interactions with the sample, it causes the laser beam to move on the four quadrants photodiode detector. This movement results in a change in the amount of light hitting the two upper and lower photodiode quadrants, which is then converted into an electrical signal. This signal is used to track the cantilever's position in real-time during scanning, allowing for precise topographical measurements.

The AFM scans the sample's surface by moving the probe laterally in a raster pattern. As the probe moves across the surface, it continually adjusts the distance between itself and the sample to maintain the set-point force. The vertical motion of the piezoelectric scanner records changes in the height of the probe, creating a topographical map of the sample's surface.

AFM measurements were performed by commercially available Nunano Scout probes with nominal spring constant 42 N/m, resonant frequency 350 kHz and tip radius of 5 nm. To verify nanoribbon widths special 'Nanosensors' probes were also used (spring constant of 10 - 130 N/m, resonant frequency 300 kHz, and tip radius of 2 nm.

3.4.1 Kelvin Probe Force Microscopy

KPFM allows to measure the contact potential difference (CPD which is the difference between the work function of the sample at the location of the measurement and that of the tip. If the work function of the tip is known during the measurement, the local work function of the sample surface can be estimated. KPFM was done using the same instrument as mentioned above while using frequency modulation (FM-KPFM) double pass mode [92]. Commercially bought conductive tips (NuNano Scout 350) were used for this purpose with 40 nm platinum coating with a 5 nm titanium adhesion layer on both sides of the probe. The setup and CPD are represented in Figure 3.6.

With a double-pass configuration, every line in the scan is traversed by the cantilever twice. The first pass involves mapping the topography in amplitude modulation mode while the tip is in contact with the sample. The user-specified lift height parameter is then tuned for each scan and is generally a few or tens of nanometers. The tip is then raised above the sample for the second pass, with the piezoelectric scanner feedback off, an AC voltage is applied to the probe at its resonance frequency. In contrast to piezo-actuation, which is utilized to drive the cantilever for topographical imaging in the first pass, electrical actuation is employed. The electrostatic forces that ensue when the probe's potential is

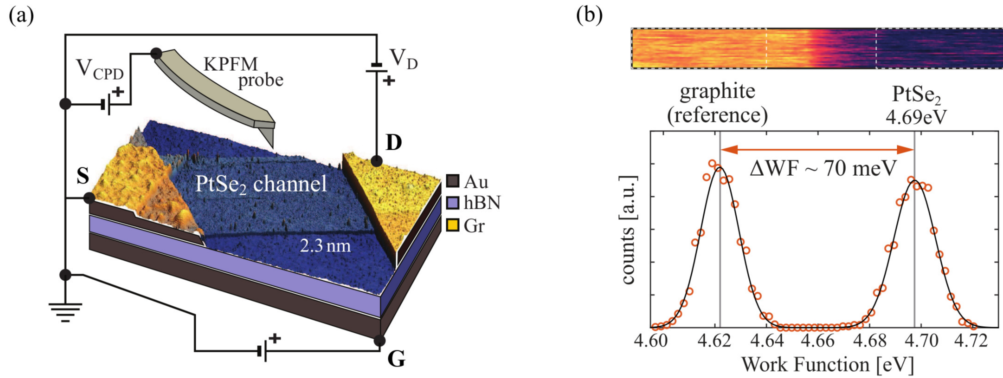

Figure 3.6: (a) Schematic representation of KPFM setup (out of scale) with relevant electrical connections used for the studies carried out (publication number 1 and 3). (b) Work function difference between graphite and $PtSe_2$ using several single line scans along the contact and channel area (as shown in publication number 3).

different from the sample surface potential cause the cantilever to mechanically oscillate. The surface potential, which is a measurement of the potential difference between the tip and the sample, is then brought to zero using a DC voltage selected by a potential feedback loop [92].

The nanoribbon and flake devices as shown in both publication number 1 and 3 were measured while under operation, i.e. while the devices were applied with a source drain and a source gate voltage. This allowed to track the conduction path in the case of nanoribbon devices and contact resistance for the study of $PtSe_2$.

3.5 Raman spectroscopy

Raman scattering is a single-step scattering [93] where a photon of energy (hv) is scattered into another photon of energy (hv'). Most of the scattered light is at the same wavelength (or color) as the laser source and does not provide useful information – this is called Rayleigh Scattering. The difference h (v − v') corresponds to the energy gap Δ = E_f - E_i. If the scattered energy hv' $<$ hv, the scattering is known as Stokes Raman scattering. Whereby the excess energy is transferred to produce an excited state (f). A schematic illustration of this is represented in the Figure 3.7.

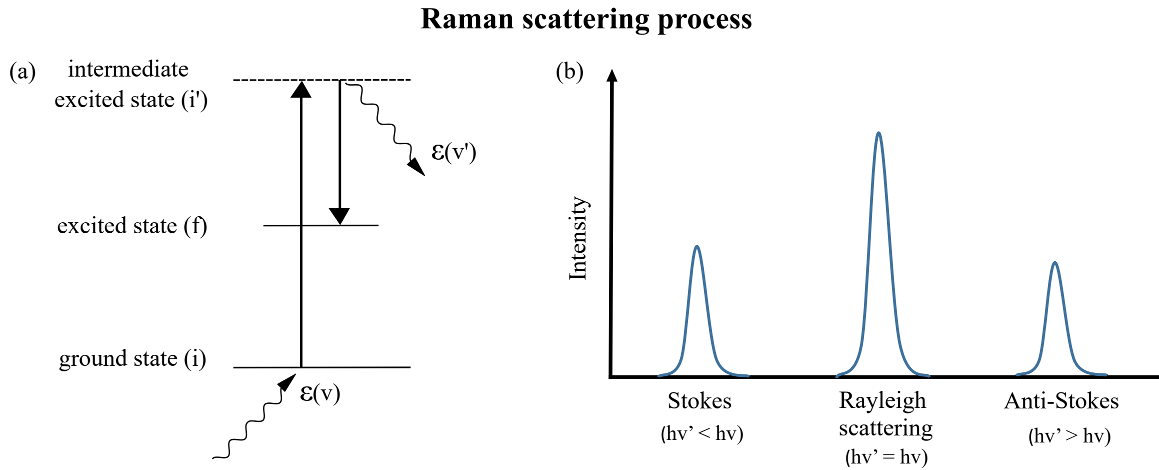

Figure 3.7: (a) Schematic for the representation of the basic principle of Raman scattering. (b) Raman spectrum lines.

A shift from a higher vibrational level to a lower level occurs when the frequency of the scattered photon is greater than that of the incident photon (hv' $<$ hv), producing an anti-stokes line.

In theoretical terms, the interaction of light with the molecules causes the distortion of the electron cloud around the nuclei resulting in the polarization of the molecule. This can be represented as, $\mu = \alpha$ E, where μ is the dipole moment that is induced due to the electron cloud displacement. It is linearly proportional to the strength of the electric field (E) and the polarizability of the material α [93, 94]. As a consequence a virtual state is formed which has a short life time. This causes the re-radiation of the photon which forms the foundation of raman spectroscopy. A variety of physical and chemical properties can be measured using Raman spectroscopy. It has been used in the 2D material community to accurately measure the number of graphene layers and TMDCs [95, 96].

For 2D materials, Raman spectra can be used for various purposes including crystallinity and doping as well as the characterisation of intrinsic stress and strain [97, 98]. During the course of thesis, Raman measurements were used to verify the crystallinity of fabricated nanoribbons by Raman mapping as presented in the publication number 1. The instrument used for the measurements was Labram Evolution by Horiba at the Raman

TERS-AFM lab situated in department of Applied Geosciences and Geophysics, Montanuniversität Leoben. The setup of Raman spectrometer is schematically represented in figure 3.8.

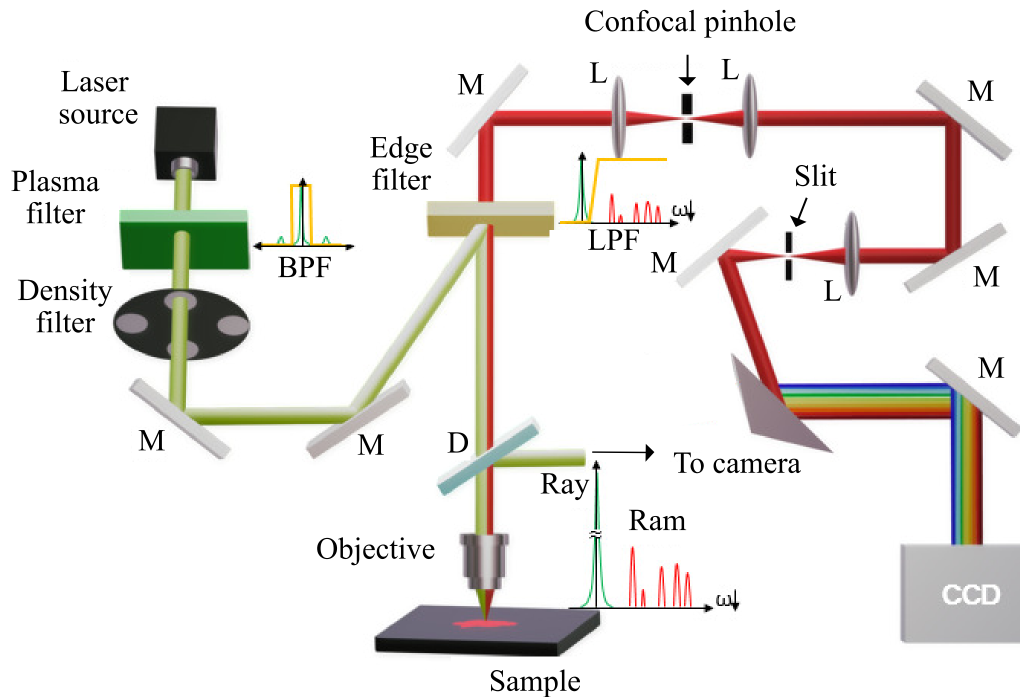

Figure 3.8: (a) Schematic for path opted by the laser in a raman spectroscope. BPF = Band Pass Filter, LPF = Long Pass Filter, D = Dichroic Mirror, L = Lens, M = Mirror, CCD = Charge Coupled Detector, Ray = Rayleigh scattering, Ram = Raman scattering. For details see text.

Laser source in the raman spectrometer: The laser source produces a monochromatic, stable and intense laser beam. Different types of lasers such as Argon ion laser (488 and 514.5 nm), Krypton ion laser (530.9 and 647.1 nm), Helium–Neon (He–Ne) (632.8 nm), Near Infrared (IR) diode lasers (785 and 830 nm) can be used as light sources.

Band pass filter: These filters isolate a single beam of laser while using high quality gratings and notch filters. Low pass filter: Used to separate weak Raman lines from the intense Rayleigh scattered radiations. Charge Coupled Device (CCD): It is a multichannel array detector composed of thousands of “pixels”. These elements (pixels) accumulate charge which is then read out by the electronics. CCDs are cooled down using air cooling

due to constant charge accumulation resulting in the heating.

3.6 Electrical characterization

Electrical characterizations for 2D material flakes and nanoribbons were performed using the INSTEC probe station and Keithley dual source meter 2636B. The fabricated devices of field effect transistors (FETs) were subjected to current voltage (I-V) measurements with variable source gate voltage(V_{SG}) and drain-source voltage (V_{DS}). The resulting curves (I_{DS}) vs (V_{SG}) provide information about the device's conductivity, carrier mobility, ON/OFF ratio. Moreover, the type of contact (Ohmic or Schottky) to channel can be verified by measuring the output curves. Figure 3.9 shows the basics of the measuring instruments used.

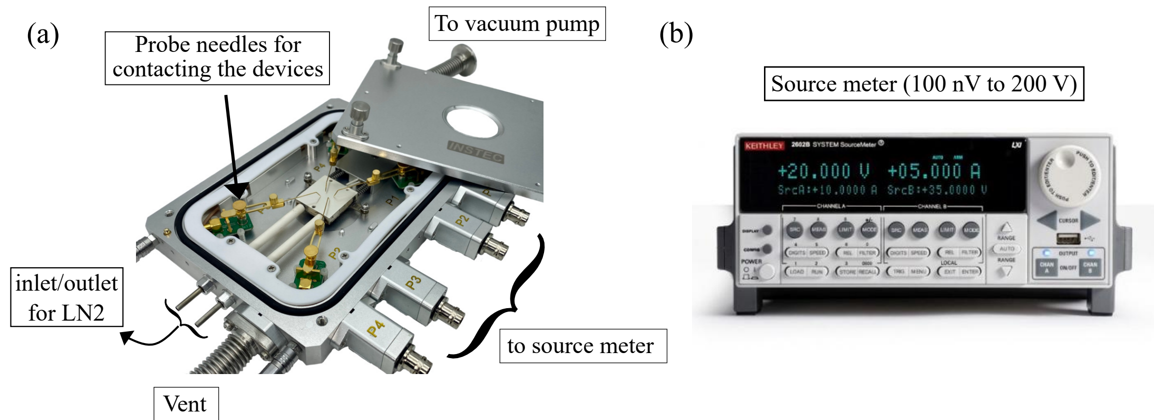

Figure 3.9: (a) Probe station with relevant features and (b) the Keithley dual source meter (2636B) used during the thesis.

A typical device configuration is represented in figure 3.10(a) which highlights the main features of a device. S and D represent the source and drain electrode of the device. Figure 3.10(b) shows a representative *I-V* plot with critical parameters labeled. I_G represents the gate leakage current whereas V_{DD} represents the supply voltage for the transistor (that is, the target maximum voltage of operation for both V_{DS} and V_{SG}. The maximum drain current that flows through the device is dependent on the device dimensions therefore, ideally it is shown as μA / μm (micro ampere per micro meter) with respect to the device

width.

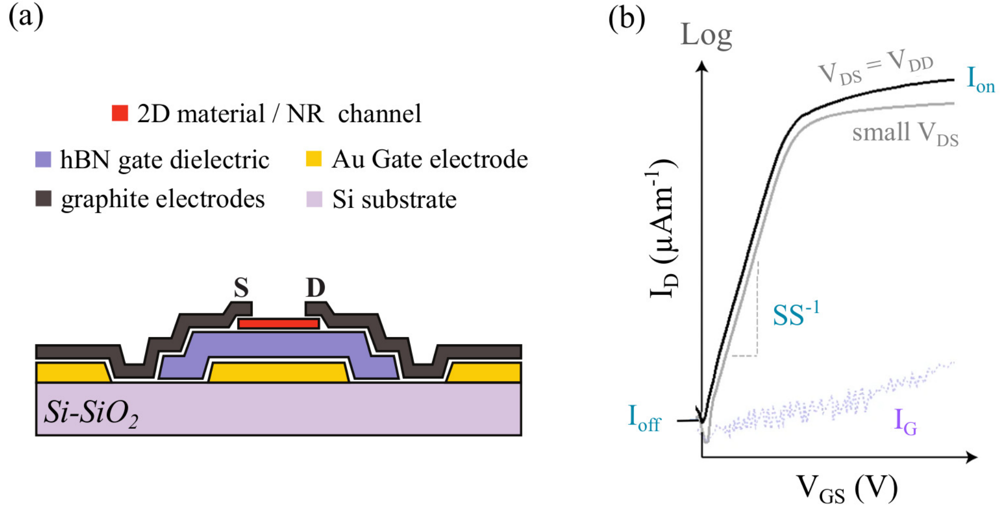

Figure 3.10: (a) A schematic representation of a typical 2D material device with. (b) Important features of the electrical curves obtained which highlight the device performance.

The device performance can be analysed by various parameters such as:

(i) Linear mobility of charge carriers (μ): For a n-type device as shown in Figure 3.10, only electron mobilities are available. However, for an ambipolar device both electron and hole mobilities can be achieved. The mobility can be calculated using the equation below:

$$\mu = \frac{L}{WC_{oxV}} \frac{dI_d}{dV_{bg}} \tag{3.1}$$

where C_{hBN} represents the effective capacitance per area. L and W represent the channel length and width respectively. It is calculated considering vacuum permittivity (ϵ_0) and relative permittivity (ϵ_r for hBN to be 3.5 and 3.9 for SiO_2) [99]. However, the commonly used parallel capacitance model (equation 3.1) overestimates the mobilities when applied to NRs as their widths are much smaller compared to the oxide thickness [52, 71]. Therefore, taking into account the capacitance per unit area for the fringing capacitance model [100], a more realistic area-specific gate capacitance can be expressed as:

$$C_{ox} \approx \varepsilon_{ox}\varepsilon_0 \left\{ \frac{\pi}{\ln\left[6\left(\frac{t_{ox}}{W}+1\right)\right]W} + \frac{1}{t_{ox}} \right\} \tag{3.2}$$

where t_{ox} is the oxide thickness and W is channel width [71].

(ii) I_{ON}/I_{OFF} ratio: This is a key parameter that represents the switching capability of a FET. This ratio is a crucial indicator for assessing the effectiveness and performance of FETs since it measures the variation in current flow between the transistor's on and off states. The on-state of an FET occurs when the device is in the conducting or active mode. In this configuration, the FET functions as a closed switch by permitting a sizable current to travel between its source and drain terminals. The off-state of an FET occurs when the device is in the non-conducting or inactive mode. In this state, the FET effectively blocks the current flow between the source and drain terminals, behaving like an open switch. I_G represents the gate leakage current. To be used in logic circuits, a FET should have minimum I_{ON}/I_{OFF} ratio of 10^4. A low on-off ratio indicates that the transistor may not completely turn off, leading to higher power consumption and potentially signal degradation.

(iii) Subthreshold Swing (SS): The slope of the (I_{SD}) vs (V_{SG}) curve in the subthreshold region provides the SS of a FET as shown in Figure 3.10(b). It is typically measured on a logarithmic scale, which means it's the change in gate voltage needed to change the drain current by a factor of 10. A linear or steep slope SS indicates that the transistor can turn on more sharply and efficiently as the gate voltage is increased slightly above the threshold. Achieving a low SS is essential for designing low-power electronic devices

CHAPTER 4
SUMMARY AND CONCLUSION

A universal method for the fabrication and integration of 2D materials into field effect transistors

A novel method to fabricate nanoribbon networks starting from arbitrary 2D materials is proposed which is not limited to graphene and is applicable to TMDCS and their heterostructures [71]. The process flow for the method is represented in the Figure 4.1.

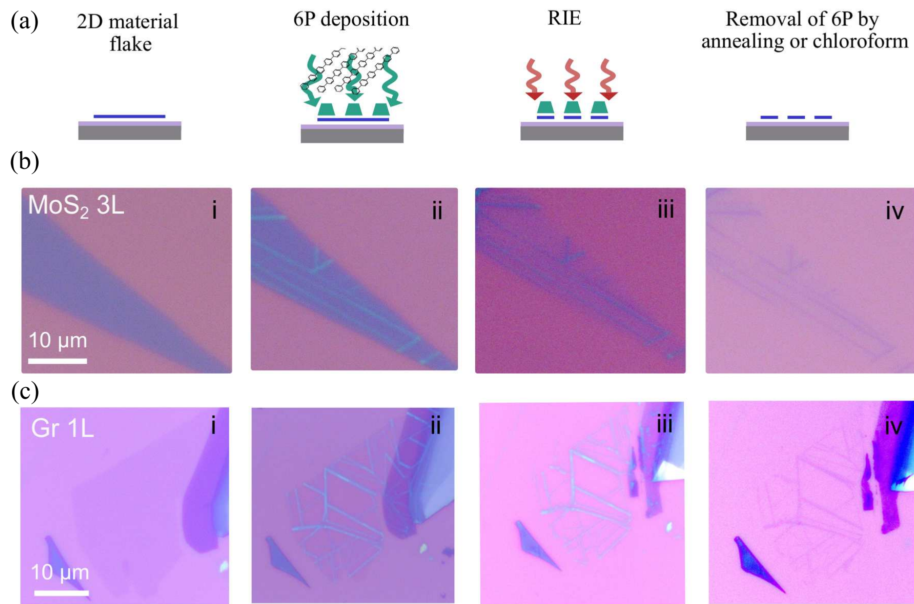

Figure 4.1: (a) Schematics for the steps involved in the nanoribbon fabrication process. (b) and (c (i-iv)) shows the optical microscope images of the steps applied to a 3 layered (3L) MoS_2 and graphene monolayer. i) an exfoliated flake is transferred onto Si/SiO_2. ii) organic molecules are deposited via hot wall epitaxy process. iii) the flake is subjected to reactive ion etching with oxygen plasma. iv) nanoribbon network is annealed under high vacuum or rinsed in chloroform to remove the organic molecules. Adopted from [publication 1], see chapter 5.1.

The method allows achieving NR widths below 20 nm. The technique is widely ap-

plicable and is demonstrated by fabricating molybednum disulphide, tungsten disulphide, tungsten diselenide, and graphene nanoribbon field effect transistors that inherently do not suffer from interconnection resistance [71]. Figure 4.2 shows the raman spectra for MoS_2 flake and nanoribbons. An absence of the defect activated peaks represents the single crystalline nature of the MoS_2 nanoribbons.

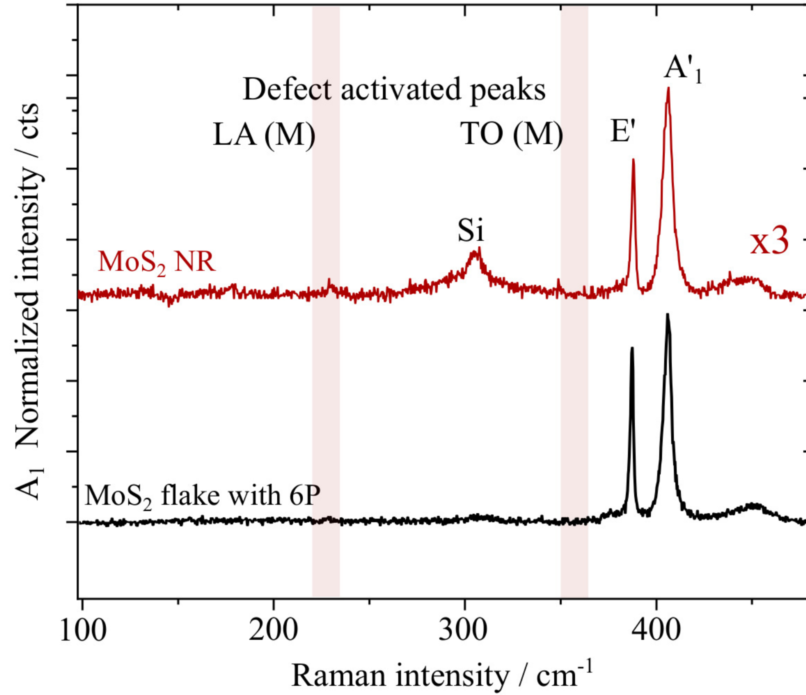

Figure 4.2: (a) Shows the absence of defect related peaks in both, monolayer MoS_2 flake and the fabricated MoS_2 nanoribbon. Adopted from [publication 1], see chapter 5.1.

Examined TMDC nanoribbon network FETs exhibit band transport, maintain high carrier mobility values, clear OFF-states, high ON-state currents, and importantly stable operation over a large number of sweeping cycles [71]. The electrical properties of a MoS_2 nanoribbon device are represented in Figure 4.3 which represents 100 subsequent forward and backward sweeping electrical transfer curves (semi log scale) of a MoS_2 NR network FET measured under vacuum and with 2 V/s sweeping rates. The ON current values reach up to 0.1μA at 300 K while maintaining an OFF state of 10^{-10}. Figure 4.1(b,c) show negligible variations for μ_{lin} and V_{th}, which highlights the highly stable nature of NR FETs.

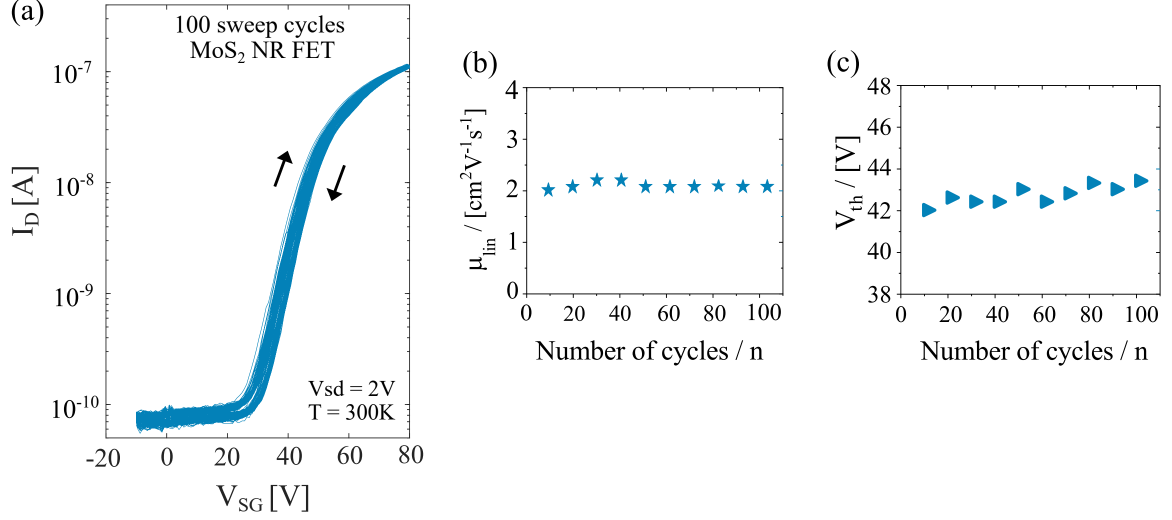

Figure 4.3: (a) The I_D vs V_{GS} characteristics for MoS_2 nanoribbon FET (b) Statistics for the extracted apparent linear electron mobility (μ_{lin}) as a function of the number of sweeps, considering the fringing capacitance model. (c) statistics of the extracted threshold voltage (V_{th}) as a function of the number of sweeps. Compiled from [publication 1], see chapter 5.1.

Observation of ferroelectric behaviour in graphene nanoribbons

The thesis also reports the observation of robust ferroelectricity in graphene nanoribbons due to oxygen terminated edges which support adsorption of water molecules. The termination of these nanoribbons can be controlled by using different sources for the plasma, for example oxygen (O_2) and sulfur hexafluoride SF_6 which in turn allows the edges to be either polar or non-polar in nature, respectively. An exposure to the oxygen plasma during the RIE causes the polar water molecules to be attached to the edges [101, 102]. These polar molecules have equal probability of arranging themselves symmetrically with respect to the graphene basal plane (either up or down configurations) in a form of cluster under $V_g = 0$ [102]. Once the nanoribbon devices are subjected to the external gate bias (V_g), this disrupts the equal probability of arrangement and only one orientation is preferred for a particular $V_g \neq 0$. The orientation is then changed in accordance with the localized field (E_{loc} or V_g) which induces a torque on the water molecules adsorbed at the edges.

Such torque is a result of electric forces acting on the positively charged hydrogen atoms and negatively charged oxygen atoms, thus facilitating their flip/rotation according to the applied V_g or E_{loc} [103]. The simultaneous orientation of water molecules induces a net dipole moment perpendicular to the plane of graphene nanoribbons resulting in the large ambipolar stability [71].

It was observed that the hysteresis window is independent of the temperature in a large and technology relevant range, only if the ribbons are having bi-layer or thicker graphene stack. This was attributed to a collective behaviour of water dipoles, enabled by the "bridge" molecules that adsorb between the two layers (see Figure 4.4).

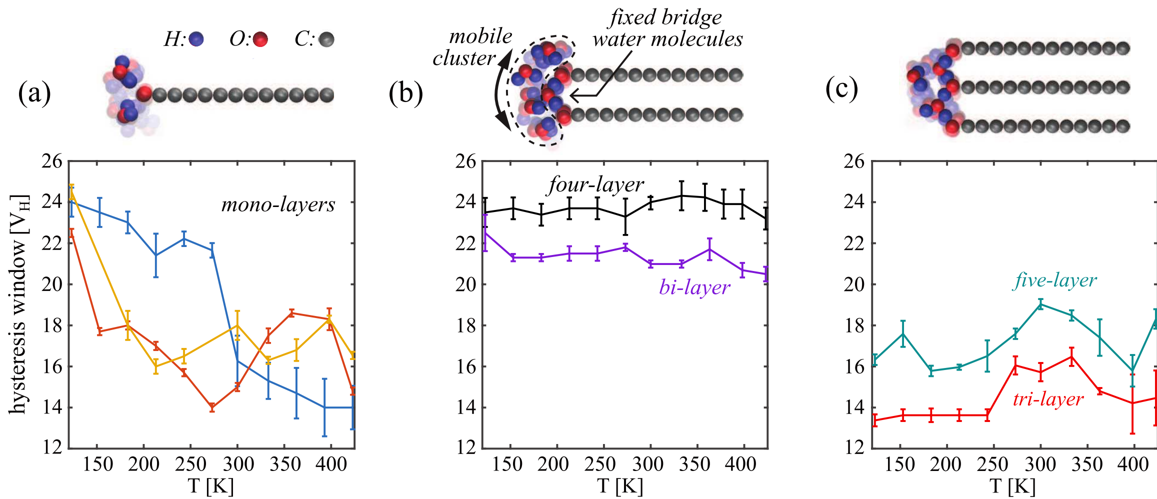

Figure 4.4: (a-c) Temperature dependence of the hysteresis window (V_H) considering varying thicknesses of graphene NRs. The plot for monolayers includes three different devices colored blue, yellow and orange. Top of (a-c) MD simulation models exhibiting typical local configuration of water clusters at the Gr edges for varying thicknesses of graphene in absence of the external electric field. Compiled from publication [2], see chapter 5.2.

With large scale molecular dynamics simulations (performed by Dr. Igor Stankovic), the key features observed in the experiments were replicated. It was proposed that the molecules can collectively stay bound in one state by intermolecular Coulomb interactions, yielding a ferroelectric effect that is not thermally activated [104]. The study captures the importance of the collective behaviour of water, especially in the interaction with nanostructured materials and its potential for application as a molecular switch in nanoelectron-

ics.

High performance and stable $PtSe_2$ field effect transistors achieved via an all van-der-Waals assembly

$PtSe_2$ FETs contacted by graphite electrodes were proposed to address the contact resistance challenge faced by the 2D materials, simultaneously employing a 2D semiconductor which can be grown at BEoL friendly temperatures. Figure 4.5(a,b) shows the transconductance properties of a $PtSe_2$ FET for various temperatures and V_D values.

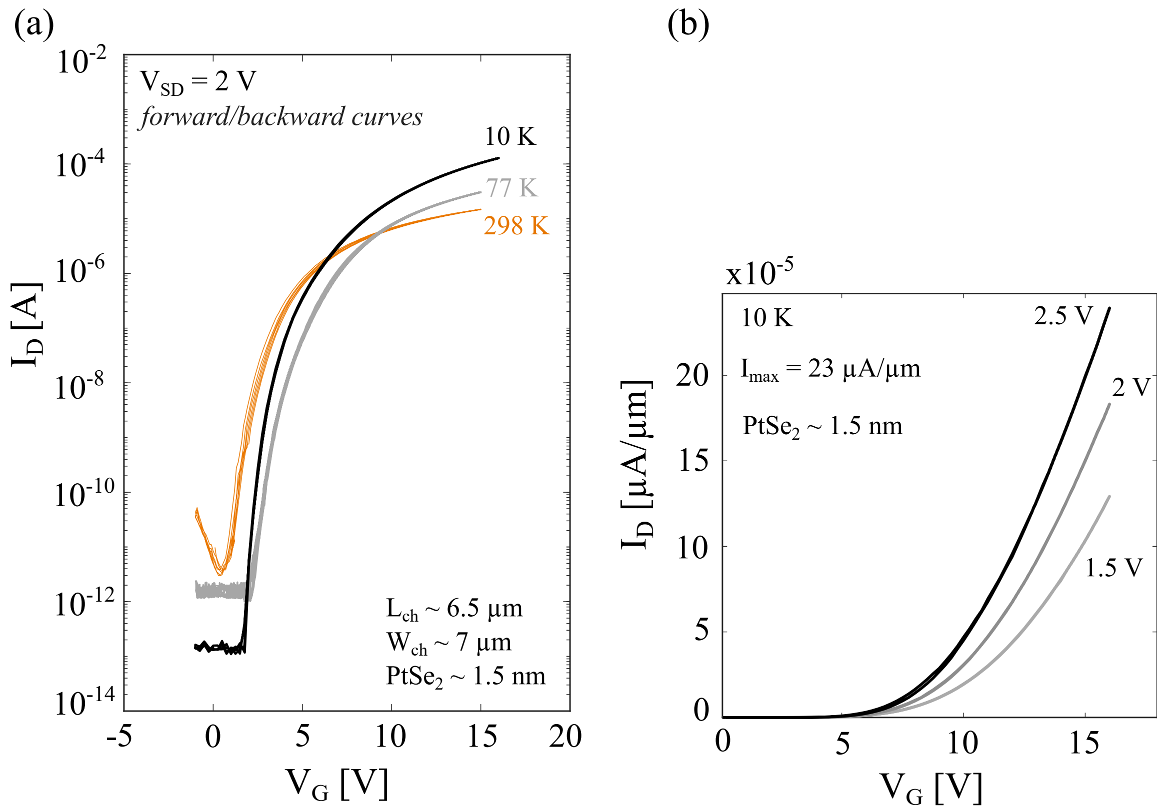

Figure 4.5: (a) Electrical transport properties of a 1.5 nm thick $PtSe_2$ device at 298 K, 77 K and 10 K. (b) Linear plots of transconductance show high ON currents. Compiled from publication [3], see chapter 5.3.

KPFM measurements reveal low contact resistance of 36 kΩ.cm between $PtSe_2$ and graphite electrodes, resulting in high current densities and I_{ON}/I_{OFF} ratios of up to 10^9. Integration of hBN provides an atomically smooth and essentially trap free gate dielectric

interface. Consequently, our devices display minimal hysteresis and high reliability despite large number of cyclic sweeps. The potential for exceptionally stable and field switchable electron and hole transport within a single $PtSe_2$ device presents an avenue for runtime reconfigurability which could allow new electronics architectures inaccessible in the conventional Si based technologies. Engineering all van der Waals interfaces also allows us to fully employ $PtSe_2$ as a potential platform for 2D material-based devices.

Multi–layer paladium diselenide as a contact material for two–dimensional tungsten diselenide field–effect transistors

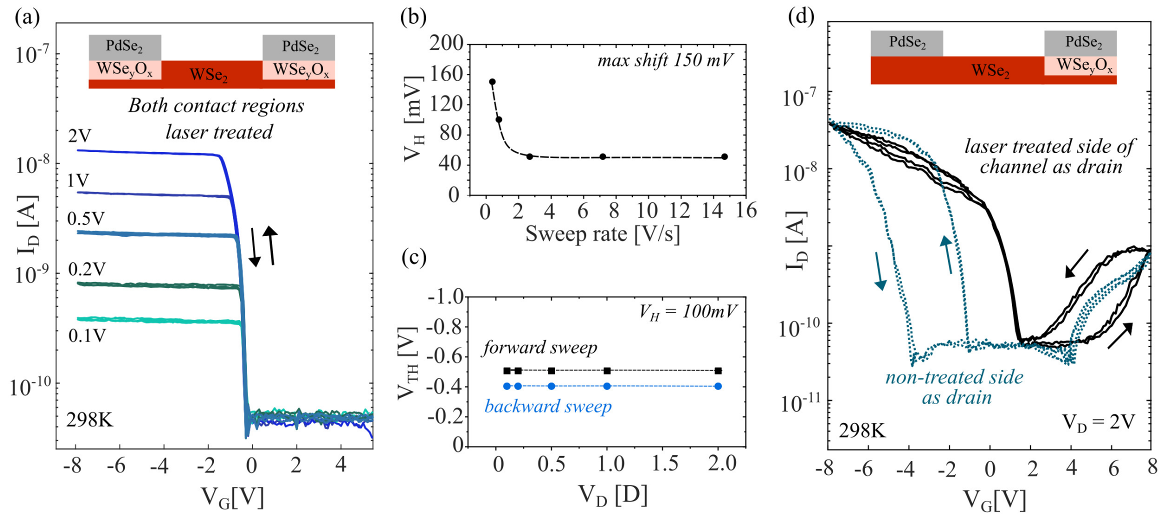

Figure 4.6: (a) Electrical response of WSe_2/WSe_yO_x/$PdSe_2$ electrode interface: (a) Semi–log scale electrical transfer curves of a WSe_2 device with both source and drain electrode interfaces treated by a laser prior to stamping $PdSe_2$ contacts measured at 298 K, $2{\times}10^{-2}$ mbar). (b) V_H plot as a function of a scan speed (measured at 298 K, $2{\times}10^{-2}$ mbar). (c) Position of the threshold voltage V_{th} for both forward and backward V_G sweeping with varied V_D. The difference indicates the hysteresis (V_H) is independent of V_D. (d) Semi–log scale electrical transfer curves for an asymmetric WSe_2 FET with only one contact pad treated by the laser. The dotted lines represent the drain electrode connected to the non–treated $PdSe_2$ contact side, while source and drain were swapped for solid black line. The arrows indicate the V_G sweeping direction. Compiled from publication [4], see chapter 5.4.

Lastly, we investigated the behavior of two–dimensional WSe_2 FETs with multi–layer palladium diselenide ($PdSe_2$) as a contact material. We employed both laser treated and

non-treated devices to investigate the effects of the laser mediated oxidation. The contact regions were ablated to transform first few layers into conductive tungsten selenium oxide (WSe_2/WSe_yO_x) which acts as an efficient hole injection layer. It was demonstrated that $PdSe_2$ contacts favor hole injection while preserving the ambipolar nature of the channel material yielding dominant p-type WSe_2 devices.

It was observed that the subthreshold swing had improved two-fold and the V_th for the hole-branch had stabilized. On the other hand, asymmetric WSe_2 FETs with pronounced and stable hysteretic behavior of a single (electron or hole) branch were obtained for the case where one electrode interface was altered by the laser treatment. The direction in which the drain voltage was applied determined the hysteresis as shown in Figure 4.6(d). Designing in-memory computing and reconfigurable electrical concepts based solely on 2D interfaces is possible with the help of such device response.

REFERENCES

[1] K. S. Novoselov, A. K. Geim, S. V. Morozov, D.-e. Jiang, Y. Zhang, S. V. Dubonos, I. V. Grigorieva, and A. A. Firsov, "Electric field effect in atomically thin carbon films," *Science*, vol. 306, no. 5696, pp. 666–669, 2004.

[2] L. Cheng, X. Wang, F. Gong, T. Liu, and Z. Liu, "2D nanomaterials for cancer theranostic applications," *Advanced Materials*, vol. 32, no. 13, p. 1 902 333, 2020.

[3] X. Liu and M. C. Hersam, "2D materials for quantum information science," *Nature Reviews Materials*, vol. 4, no. 10, pp. 669–684, 2019.

[4] Y. Yi, Z. Chen, X.-F. Yu, Z.-K. Zhou, and J. Li, "Recent advances in quantum effects of 2D materials," *Advanced Quantum Technologies*, vol. 2, no. 5-6, p. 1 800 111, 2019.

[5] M. Atatüre, D. Englund, N. Vamivakas, S.-Y. Lee, and J. Wrachtrup, "Material platforms for spin-based photonic quantum technologies," *Nature Reviews Materials*, vol. 3, no. 5, pp. 38–51, 2018.

[6] A. Elbanna, H. Jiang, Q. Fu, J.-F. Zhu, Y. Liu, M. Zhao, D. Liu, S. Lai, X. W. Chua, and J. Pan, "2D material infrared photonics and plasmonics," *ACS Nano*, vol. 17, no. 5, pp. 4134–4179, 2023.

[7] L. Tang, X. Meng, D. Deng, and X. Bao, "Confinement catalysis with 2D materials for energy conversion," *Advanced Materials*, vol. 31, no. 50, p. 1 901 996, 2019.

[8] X. Zhang, L. Hou, A. Ciesielski, and P. Samori, "2D materials beyond graphene for high-performance energy storage applications," *Advanced Energy Materials*, vol. 6, no. 23, p. 1 600 671, 2016.

[9] E. C. Ahn, "2D materials for spintronic devices," *npj 2D Materials and Applications*, vol. 4, no. 1, p. 17, 2020.

[10] W. Han, "Perspectives for spintronics in 2D materials," *Apl Materials*, vol. 4, no. 3, p. 032 401, 2016.

[11] D. Akinwande, C. Huyghebaert, C.-H. Wang, M. I. Serna, S. Goossens, L.-J. Li, H.-S. P. Wong, and F. H. Koppens, "Graphene and two-dimensional materials for silicon technology," *Nature*, vol. 573, no. 7775, pp. 507–518, 2019.

[12] M. C. Lemme, D. Akinwande, C. Huyghebaert, and C. Stampfer, "2D materials for future heterogeneous electronics," *Nature Communications*, vol. 13, no. 1, p. 1392, 2022.

[13] C. D. English, G. Shine, V. E. Dorgan, K. C. Saraswat, and E. Pop, "Improved contacts to MoS_2 transistors by ultra-high vacuum metal deposition," *Nano Letters*, vol. 16, no. 6, pp. 3824–3830, 2016.

[14] IEEE, "IRDS More Moore," 2021.

[15] H. Wang, L. Yu, Y.-H. Lee, Y. Shi, A. Hsu, M. L. Chin, L.-J. Li, M. Dubey, J. Kong, and T. Palacios, "Integrated circuits based on bilayer MoS_2 transistors," *Nano Letters*, vol. 12, no. 9, pp. 4674–4680, 2012.

[16] T. Roy, M. Tosun, J. S. Kang, A. B. Sachid, S. B. Desai, M. Hettick, C. C. Hu, and A. Javey, "Field-effect transistors built from all two-dimensional material components," *ACS Nano*, vol. 8, no. 6, pp. 6259–6264, 2014.

[17] K. Kang, S. Xie, L. Huang, Y. Han, P. Y. Huang, K. F. Mak, C.-J. Kim, D. Muller, and J. Park, "High-mobility three-atom-thick semiconducting films with wafer-scale homogeneity," *Nature*, vol. 520, no. 7549, pp. 656–660, 2015.

[18] C. D. English, K. K. Smithe, R. L. Xu, and E. Pop, "Approaching ballistic transport in monolayer MoS_2 transistors with self-aligned 10 nm top gates," in *2016 IEEE International Electron Devices Meeting (IEDM)*, IEEE, 2016, pp. 5–6.

[19] T. Schram, Q. Smets, B. Groven, M. Heyne, E. Kunnen, A. Thiam, K. Devriendt, A. Delabie, D. Lin, M. Lux, D. Chiappe, I. Asselberghs, S. Brus, C. Huyghebaert, S. Sayan, A. Juncker, M. Caymax, and I. Radu, "WS_2 transistors on 300 mm wafers with beol compatibility," in *2017 47th European Solid-State Device Research Conference (ESSDERC)*, IEEE, 2017, pp. 212–215.

[20] Y. Y. Illarionov, A. G. Banshchikov, D. K. Polyushkin, S. Wachter, T. Knobloch, M. Thesberg, L. Mennel, M. Paur, M. Stöger-Pollach, A. Steiger-Thirsfeld, M. Vexler I., M. Waltl, N. S. Sokolov, T. Mueller, and T. Grasser, "Ultrathin calcium fluoride insulators for two-dimensional field-effect transistors," *Nature Electronics*, vol. 2, no. 6, pp. 230–235, 2019.

[21] H. Wang, H. S. Wang, C. Ma, L. Chen, C. Jiang, C. Chen, X. Xie, A.-P. Li, and X. Wang, "Graphene nanoribbons for quantum electronics," *Nature Reviews Physics*, vol. 3, no. 12, pp. 791–802, 2021.

[22] W. Li, X. Gong, Z. Yu, L. Ma, W. Sun, S. Gao, Ç. Köroğlu, W. Wang, L. Liu, T. Li, H. Ning, D. Fan, Y. Xu, X. Tu, T. Xu, L. Sun, W. Wang, J. Lu, Z. Ni, J. Li, X. Duan, P. Wang, Y. Nie, H. Qiu, Y. Shi, E. Pop, and J. Wang, "Approaching the quantum limit in two-dimensional semiconductor contacts," *Nature*, vol. 613, no. 7943, pp. 274–279, 2023.

[23] C. Tan, M. Yu, J. Tang, X. Gao, Y. Yin, Y. Zhang, J. Wang, X. Gao, C. Zhang, X. Zhou, L. Zheng, H. Liu, K. Jiang, F. Ding, and H. Peng, "2D fin field-effect transistors integrated with epitaxial high-k gate oxide," *Nature*, vol. 616, no. 7955, pp. 66–72, 2023.

[24] J. Zhu, J.-H. Park, S. A. Vitale, W. Ge, G. S. Jung, J. Wang, M. Mohamed, T. Zhang, M. Ashok, M. Xue, X. Zheng, Z. Wang, J. Hansryd, A. P. Chandrakasan, J. Kong, and T. Palacios, "Low-thermal-budget synthesis of monolayer molybdenum disulfide for silicon back-end-of-line integration on a 200 mm platform," *Nature Nanotechnology*, pp. 1–8, 2023.

[25] A. Allain, J. Kang, K. Banerjee, and A. Kis, "Electrical contacts to two-dimensional semiconductors," *Nature Materials*, vol. 14, no. 12, pp. 1195–1205, 2015.

[26] M. Chhowalla, D. Jena, and H. Zhang, "Two-dimensional semiconductors for transistors," *Nature Reviews Materials*, vol. 1, no. 11, pp. 1–15, 2016.

[27] S. Das, A. Sebastian, E. Pop, C. J. McClellan, A. D. Franklin, T. Grasser, T. Knobloch, Y. Illarionov, A. V. Penumatcha, J. Appenzeller, Z. Chen, W. Zhu, I. Asselberghs, L.-J. Li, U. E. Avci, N. Bhat, T. D. Anthopoulos, and R. Singh, "Transistors based on two-dimensional materials for future integrated circuits," *Nature Electronics*, vol. 4, no. 11, pp. 786–799, 2021.

[28] T. Knobloch, S. Selberherr, and T. Grasser, "Challenges for nanoscale CMOS logic based on two-dimensional materials," *Nanomaterials*, vol. 12, no. 20, p. 3548, 2022.

[29] P.-C. Shen, C. Su, Y. Lin, A.-S. Chou, C.-C. Cheng, J.-H. Park, M.-H. Chiu, A.-Y. Lu, H.-L. Tang, M. M. Tavakoli, G. others Pitner, X. Ji, Z. Cai, N. Mao, J. Wang, V. Tung, J. Li, J. Bokor, A. Zettl, C.-I. Wu, T. L. L.-J. Palacios, and K. Jing, "Ultralow contact resistance between semimetal and monolayer semiconductors," *Nature*, vol. 593, no. 7858, pp. 211–217, 2021.

[30] Y. Liu, J. Guo, E. Zhu, L. Liao, S.-J. Lee, M. Ding, I. Shakir, V. Gambin, Y. Huang, and X. Duan, "Approaching the schottky-mott limit in van der waals metal–semiconductor junctions," *Nature*, vol. 557, no. 7707, pp. 696–700, 2018.

[31] X. Zhang, H. Yu, W. Tang, X. Wei, L. Gao, M. Hong, Q. Liao, Z. Kang, Z. Zhang, and Y. Zhang, "All-van-der-Waals barrier-free contacts for high-mobility transistors," *Advanced Materials*, vol. 34, no. 34, p. 2 109 521, 2022.

[32] H. M. Khalil, M. F. Khan, J. Eom, and H. Noh, "Highly stable and tunable chemical doping of multilayer WS_2 field effect transistor: Reduction in contact resistance," *ACS Applied Materials & Interfaces*, vol. 7, no. 42, pp. 23 589–23 596, 2015.

[33] H. Gao, J. Suh, M. C. Cao, A. Y. Joe, F. Mujid, K.-H. Lee, S. Xie, P. Poddar, J.-U. Lee, K. Kang, P. Kim, D. A. Muller, and P. Jiwoong, "Tuning electrical conductance of MoS_2 monolayers through substitutional doping," *Nano Letters*, vol. 20, no. 6, pp. 4095–4101, 2020.

[34] K. Zhu, C. Wen, A. A. Aljarb, F. Xue, X. Xu, V. Tung, X. Zhang, H. N. Alshareef, and M. Lanza, "The development of integrated circuits based on two-dimensional materials," *Nature Electronics*, vol. 4, no. 11, pp. 775–785, 2021.

[35] Y.-W. Son, M. L. Cohen, and S. G. Louie, "Energy gaps in graphene nanoribbons," *Physical Review Letters*, vol. 97, no. 21, p. 216 803, 2006.

[36] M. Y. Han, B. Özyilmaz, Y. Zhang, and P. Kim, "Energy band-gap engineering of graphene nanoribbons," *Physical Review Letters*, vol. 98, no. 20, p. 206 805, 2007.

[37] H. Pan and Y.-W. Zhang, "Edge-dependent structural, electronic and magnetic properties of MoS_2 nanoribbons," *Journal of Materials Chemistry*, vol. 22, no. 15, pp. 7280–7290, 2012.

[38] M. Slota, A. Keerthi, W. K. Myers, E. Tretyakov, M. Baumgarten, A. Ardavan, H. Sadeghi, C. J. Lambert, A. Narita, K. Müllen, and L. Bogani, "Magnetic edge states and coherent manipulation of graphene nanoribbons," *Nature*, vol. 557, no. 7707, pp. 691–695, 2018.

[39] J. Lin, Z. Peng, G. Wang, D. Zakhidov, E. Larios, M. J. Yacaman, and J. M. Tour, "Enhanced electrocatalysis for hydrogen evolution reactions from WS_2 nanoribbons," *Advanced Energy Materials*, vol. 4, no. 10, p. 1 301 875, 2014.

[40] H. I. Karunadasa, E. Montalvo, Y. Sun, M. Majda, J. R. Long, and C. J. Chang, "A molecular MoS_2 edge site mimic for catalytic hydrogen generation," *Science*, vol. 335, no. 6069, pp. 698–702, 2012.

[41] C. Chen, Y. Hang, H. Shan Wang, Y. Wang, X. Wang, C. Jiang, Y. Feng, C. Liu, E. Janzen, J. H. Edgar, Z. Wei, W. Guo, W. Hu, Z. Zhang, H. Wang, and X. Xie, "Water induced bandgap engineering in nanoribbons of hexagonal boron nitride," *Advanced Materials*, p. 2 303 198, 2023.

[42] Q. Li, X. Liu, E. B. Aklile, S. Li, and M. C. Hersam, "Self-assembled borophene/graphene nanoribbon mixed-dimensional heterostructures," *Nano Letters*, vol. 21, no. 9, pp. 4029–4035, 2021.

[43] J. Oh, Y. Kim, S. Chung, H. Kim, and J. G. Son, "Fabrication of a MoS_2/Graphene nanoribbon heterojunction network for improved thermoelectric properties," *Advanced Materials Interfaces*, vol. 6, no. 23, p. 1 901 333, 2019.

[44] Y. Cai, G. Zhang, and Y.-W. Zhang, "Polarity-reversed robust carrier mobility in monolayer MoS_2 nanoribbons," *Journal of the American Chemical Society*, vol. 136, no. 17, pp. 6269–6275, 2014.

[45] Z. Guan, H. Hu, X. Shen, P. Xiang, N. Zhong, J. Chu, and C. Duan, "Recent progress in two-dimensional ferroelectric materials," *Advanced Electronic Materials*, vol. 6, no. 1, p. 1 900 818, 2020.

[46] M. Mehdi Pour, A. Lashkov, A. Radocea, X. Liu, T. Sun, A. Lipatov, R. A. Korlacki, M. Shekhirev, N. R. Aluru, J. W. Lyding, V. Sysoev, and A. Sinitskii, "Laterally extended atomically precise graphene nanoribbons with improved electrical conductivity for efficient gas sensing," *Nature Communications*, vol. 8, no. 1, p. 820, 2017.

[47] C. Zhao, Q. Liu, K. M. Cheung, W. Liu, Q. Yang, X. Xu, T. Man, P. S. Weiss, C. Zhou, and A. M. Andrews, "Narrower nanoribbon biosensors fabricated by chemical lift-off lithography show higher sensitivity," *ACS Nano*, vol. 15, no. 1, pp. 904–915, 2020.

[48] B. Cho, M. G. Hahm, M. Choi, J. Yoon, A. R. Kim, Y.-J. Lee, S.-G. Park, J.-D. Kwon, C. S. Kim, M. Song, Y. Jeong, K.-S. Nam, S. Lee, T. J. Yoo, C. G. Kang, B. H. Lee, H. Cho Ko, P. M. Ajayan, and D.-H. Kim, "Charge-transfer-based gas sensing using atomic-layer MoS_2," *Scientific Reports*, vol. 5, no. 1, p. 8052, 2015.

[49] M. Shekhirev, A. Lipatov, A. Torres, N. S. Vorobeva, A. Harkleroad, A. Lashkov, V. Sysoev, and A. Sinitskii, "Highly selective gas sensors based on graphene nanoribbons grown by chemical vapor deposition," *ACS Applied Materials & Interfaces*, vol. 12, no. 6, pp. 7392–7402, 2020.

[50] A. Smolyanitsky, B. I. Yakobson, T. A. Wassenaar, E. Paulechka, and K. Kroenlein, "A MoS_2-based capacitive displacement sensor for dna sequencing," *ACS Nano*, vol. 10, no. 9, pp. 9009–9016, 2016.

[51] J. Zhang, L. Qian, G. B. Barin, A. H. Daaoub, P. Chen, K. Müllen, S. Sangtarash, P. Ruffieux, R. Fasel, H. Sadeghi, J. Zhang, M. Calame, and M. L. Perrin, "Contacting individual graphene nanoribbons using carbon nanotube electrodes," *Nature Electronics*, pp. 1–10, 2023.

[52] X. Li, B. Li, J. Lei, K. V. Bets, X. Sang, E. Okogbue, Y. Liu, R. R. Unocic, B. I. Yakobson, J. Hone, and A. R. Harutyunyan, "Nickel particle-enabled width-controlled growth of bilayer molybdenum disulfide nanoribbons," *Science Advances*, vol. 7, no. 50, eabk1892, 2021.

[53] D. Kotekar-Patil, J. Deng, S. L. Wong, and K. E. J. Goh, “Coulomb blockade in etched single-and few-layer MoS_2 nanoribbons,” *ACS Applied Electronic Materials*, vol. 1, no. 11, pp. 2202–2207, 2019.

[54] Y. Li, J. Fu, X. Mao, C. Chen, H. Liu, M. Gong, and H. Zeng, “Enhanced bulk photovoltaic effect in two-dimensional ferroelectric $CuInP_2S_6$,” *Nature Communications*, vol. 12, no. 1, p. 5896, 2021.

[55] M. Krems, Y. V. Pershin, and M. Di Ventra, “Ionic memcapacitive effects in nanopores,” *Nano Letters*, vol. 10, no. 7, pp. 2674–2678, 2010.

[56] S. Yuan, X. Luo, H. L. Chan, C. Xiao, Y. Dai, M. Xie, and J. Hao, “Room-temperature ferroelectricity in $MoTe_2$ down to the atomic monolayer limit,” *Nature Communications*, vol. 10, no. 1, p. 1775, 2019.

[57] C. H. Naylor, W. M. Parkin, J. Ping, Z. Gao, Y. R. Zhou, Y. Kim, F. Streller, R. W. Carpick, A. M. Rappe, M. Drndic, J. M. Kikkawa, and A. T. C. Johnson, “Monolayer single-crystal 1T-$MoTe_2$ grown by chemical vapor deposition exhibits weak antilocalization effect,” *Nano Letters*, vol. 16, no. 7, pp. 4297–4304, 2016.

[58] M. Hassanpour Amiri, J. Heidler, K. Müllen, and K. Asadi, “Design rules for memories based on graphene ferroelectric field-effect transistors,” *ACS Applied Electronic Materials*, vol. 2, no. 1, pp. 2–8, 2019.

[59] H. Ryu, K. Xu, D. Li, X. Hong, and W. Zhu, “Empowering 2D nanoelectronics via ferroelectricity,” *Applied Physics Letters*, vol. 117, no. 8, 2020.

[60] J. Xiao, H. Zhu, Y. Wang, W. Feng, Y. Hu, A. Dasgupta, Y. Han, Y. Wang, D. A. Muller, L. W. Martin, P. Hu, and X. Zhang, “Intrinsic two-dimensional ferroelectricity with dipole locking,” *Physical Review Letters*, vol. 120, no. 22, p. 227 601, 2018.

[61] Q. Yang, M. Wu, and J. Li, “Origin of two-dimensional vertical ferroelectricity in WTe_2 bilayer and multilayer,” *The Journal of Physical Chemistry Letters*, vol. 9, no. 24, pp. 7160–7164, 2018.

[62] C. Huang, Y. Du, H. Wu, H. Xiang, K. Deng, and E. Kan, “Prediction of intrinsic ferromagnetic ferroelectricity in a transition-metal halide monolayer,” *Physical Review Letters*, vol. 120, no. 14, p. 147 601, 2018.

[63] K. Chang, J. Liu, H. Lin, N. Wang, K. Zhao, A. Zhang, F. Jin, Y. Zhong, X. Hu, W. Duan, Q. Zhang, L. Fu, Q.-K. Xue, X. Chen, and J. Shuai-Hua, “Discovery of robust in-plane ferroelectricity in atomic-thick SnTe,” *Science*, vol. 353, no. 6296, pp. 274–278, 2016.

[64] N. Balke, S. M. Neumayer, J. A. Brehm, M. A. Susner, B. J. Rodriguez, S. Jesse, S. V. Kalinin, S. T. Pantelides, M. A. McGuire, and P. Maksymovych, "Locally controlled Cu-ion transport in layered ferroelectric $CuInP_2S_6$," *ACS Applied Materials & Interfaces*, vol. 10, no. 32, pp. 27 188–27 194, 2018.

[65] K. Yasuda, X. Wang, K. Watanabe, T. Taniguchi, and P. Jarillo-Herrero, "Stacking-engineered ferroelectricity in bilayer boron nitride," *Science*, vol. 372, no. 6549, pp. 1458–1462, 2021.

[66] A. Weston, E. G. Castanon, V. Enaldiev, F. Ferreira, S. Bhattacharjee, S. Xu, H. Corte-León, Z. Wu, N. Clark, A. Summerfield, T. Hashimoto, Y. Gao, W. Wang, M. Hamer, H. Read, L. Fumagalli, A. V. Kretinin, S. J. Haigh, O. Kazakova, A. K. Geim, V. I. Fal'ko, and R. Gorbachev, "Interfacial ferroelectricity in marginally twisted 2D semiconductors," *Nature nanotechnology*, vol. 17, no. 4, pp. 390–395, 2022.

[67] Z. Zheng, Q. Ma, Z. Bi, S. de La Barrera, M.-H. Liu, N. Mao, Y. Zhang, N. Kiper, K. Watanabe, T. Taniguchi, J. Kong, W. A. Tisdale, R. Ashoori, N. Gedik, L. Fu, S.-Y. Xu, and P. Jarillo-Herrero, "Unconventional ferroelectricity in moiré heterostructures," *Nature*, vol. 588, no. 7836, pp. 71–76, 2020.

[68] J. M. Caridad, G. Calogero, P. Pedrinazzi, J. E. Santos, A. Impellizzeri, T. Gunst, T. J. Booth, R. Sordan, P. Bøggild, and M. Brandbyge, "A graphene-edge ferroelectric molecular switch," *Nano Letters*, vol. 18, no. 8, pp. 4675–4683, 2018.

[69] A. Narita, X. Feng, and K. Müllen, "Bottom-up synthesis of chemically precise graphene nanoribbons," *The Chemical Record*, vol. 15, no. 1, pp. 295–309, 2015.

[70] A. Aljarb, J.-H. Fu, C.-C. Hsu, C.-P. Chuu, Y. Wan, M. Hakami, D. R. Naphade, E. Yengel, C.-J. Lee, S. Brems, T.-A. Chen, M.-Y. Li, S.-H. Bae, W.-T. Hsu, Z. Cao, and V. Tung, "Ledge-directed epitaxy of continuously self-aligned single-crystalline nanoribbons of transition metal dichalcogenides," *Nature Materials*, vol. 19, no. 12, pp. 1300–1306, 2020.

[71] M. A. Aslam, T. H. Tran, A. Supina, O. Siri, V. Meunier, K. Watanabe, T. Taniguchi, M. Kralj, C. Teichert, E. Sheremet, *et al.*, "Single-crystalline nanoribbon network field effect transistors from arbitrary two-dimensional materials," *npj 2D Materials and Applications*, vol. 6, no. 1, p. 76, 2022.

[72] Z. Shi, X. Wang, Q. Li, P. Yang, G. Lu, R. Jiang, H. Wang, C. Zhang, C. Cong, Z. Liu, T. Wu, H. Wang, Q. Yu, and X. Xie, "Vapor-liquid-solid growth of large-area multilayer hexagonal boron nitride on dielectric substrates," *Nature Communications*, vol. 11, no. 1, p. 849, 2020.

[73] A. Yella, E. Mugnaioli, M. Panthofer, H. A. Therese, U. Kolb, and W. Tremel, "Bismuth-catalyzed growth of SnS_2 nanotubes and their stability," *Angewandte Chemie International Edition*, vol. 48, no. 35, pp. 6426–6430, 2009.

[74] Y. Zou, Z.-G. Chen, Y. Huang, L. Yang, J. Drennan, and J. Zou, "Anisotropic electrical properties from vapor-solid-solid grown Bi_2Se_3 nanoribbons and nanowires," *The Journal of Physical Chemistry C*, vol. 118, no. 35, pp. 20 620–20 626, 2014.

[75] S. Li, Y.-C. Lin, W. Zhao, J. Wu, Z. Wang, Z. Hu, Y. Shen, D.-M. Tang, J. Wang, Q. Zhang, H. Zhu, L. Chu, W. Zhao, C. Liu, Z. Sun, T. Taniguchi, M. Osada, W. Chen, Q.-H. Xu, A. T. S. Wee, K. Suenaga, F. Ding, and G. Eda, "Vapour–liquid–solid growth of monolayer MoS_2 nanoribbons," *Nature Materials*, vol. 17, no. 6, pp. 535–542, 2018.

[76] S. Chen, S. Kim, W. Chen, J. Yuan, R. Bashir, J. Lou, A. M. Van Der Zande, and W. P. King, "Monolayer MoS_2 nanoribbon transistors fabricated by scanning probe lithography," *Nano Letters*, vol. 19, no. 3, pp. 2092–2098, 2019.

[77] H. Liu, J. Gu, and D. Y. Peide, "MoS_2 nanoribbon transistors: Transition from depletion mode to enhancement mode by channel-width trimming," *IEEE Electron Device Letters*, vol. 33, no. 9, pp. 1273–1275, 2012.

[78] K. J. Erickson, A. L. Gibb, A. Sinitskii, M. Rousseas, N. Alem, J. M. Tour, and A. K. Zettl, "Longitudinal splitting of boron nitride nanotubes for the facile synthesis of high quality boron nitride nanoribbons," *Nano Letters*, vol. 11, no. 8, pp. 3221–3226, 2011.

[79] M. Kratzer and C. Teichert, "Thin film growth of aromatic rod-like molecules on graphene," *Nanotechnology*, vol. 27, no. 29, p. 292 001, 2016.

[80] A. Matković, J. Genser, D. Lüftner, M. Kratzer, R. Gajić, P. Puschnig, and C. Teichert, "Epitaxy of highly ordered organic semiconductor crystallite networks supported by hexagonal boron nitride," *Scientific Reports*, vol. 6, no. 1, p. 38 519, 2016.

[81] M. Kratzer, A. Matkovic, and C. Teichert, "Adsorption and epitaxial growth of small organic semiconductors on hexagonal boron nitride," *Journal of Physics D: Applied Physics*, vol. 52, no. 38, p. 383 001, 2019.

[82] A. M. Van Der Zande, P. Y. Huang, D. A. Chenet, T. C. Berkelbach, Y. You, G.-H. Lee, T. F. Heinz, D. R. Reichman, D. A. Muller, and J. C. Hone, "Grains and grain boundaries in highly crystalline monolayer molybdenum disulphide," *Nature Materials*, vol. 12, no. 6, pp. 554–561, 2013.

[83] D. Zhu, H. Shu, F. Jiang, D. Lv, V. Asokan, O. Omar, J. Yuan, Z. Zhang, and C. Jin, "Capture the growth kinetics of cvd growth of two-dimensional MoS_2," *npj 2D Materials and Applications*, vol. 1, no. 1, p. 8, 2017.

[84] H. Li, J. Wu, X. Huang, G. Lu, J. Yang, X. Lu, Q. Xiong, and H. Zhang, "Rapid and reliable thickness identification of two-dimensional nanosheets using optical microscopy," *ACS Nano*, vol. 7, no. 11, pp. 10 344–10 353, 2013.

[85] S. Puebla, H. Li, H. Zhang, and A. Castellanos-Gomez, "Apparent colors of 2D materials," *Advanced Photonics Research*, vol. 3, no. 4, p. 2 100 221, 2022.

[86] I. D. Marion, D. Čapeta, B. Pielić, F. Faraguna, A. Gallardo, P. Pou, B. Biel, N. Vujičić, and M. Kralj, "Atomic-scale defects and electronic properties of a transferred synthesized MoS_2 monolayer," *Nanotechnology*, vol. 29, no. 30, p. 305 703, 2018.

[87] A. Andreev, G. Matt, C. J. Brabec, H. Sitter, D. Badt, H. Seyringer, and N. Sariciftci, "Highly anisotropically self-assembled structures of para-sexiphenyl grown by hot-wall epitaxy," *Advanced Materials*, vol. 12, no. 9, pp. 629–633, 2000.

[88] G. Hlawacek, F. S. Khokhar, R. van Gastel, B. Poelsema, and C. Teichert, "Smooth growth of organic semiconductor films on graphene for high-efficiency electronics," *Nano Letters*, vol. 11, no. 2, pp. 333–337, 2011.

[89] A. Matkovic, J. Genser, M. Kratzer, D. Lüftner, Z. Chen, O. Siri, P. Puschnig, C. Becker, and C. Teichert, "Light-assisted charge propagation in networks of organic semiconductor crystallites on hexagonal boron nitride," *Advanced Functional Materials*, vol. 29, no. 43, p. 1 903 816, 2019.

[90] B. Vasić, I. Stanković, A. Matković, M. Kratzer, C. Ganser, R. Gajić, and C. Teichert, "Molecules on rails: Friction anisotropy and preferential sliding directions of organic nanocrystallites on two-dimensional materials," *Nanoscale*, vol. 10, no. 39, pp. 18 835–18 845, 2018.

[91] W. Zhou, X. Zou, S. Najmaei, Z. Liu, Y. Shi, J. Kong, J. Lou, P. M. Ajayan, B. I. Yakobson, and J.-C. Idrobo, "Intrinsic structural defects in monolayer molybdenum disulfide," *Nano Letters*, vol. 13, no. 6, pp. 2615–2622, 2013.

[92] T. Machleidt, E. Sparrer, D. Kapusi, and K. Franke, "Deconvolution of kelvin probe force microscopy measurements—methodology and application," *Measurement Science and Technology*, vol. 20, no. 8, p. 084 017, 2009.

[93] J. Weiner and F. Nunes, *Light-matter interaction: physics and engineering at the nanoscale*. Oxford University Press, 2017.

[94] R. R. Jones, D. C. Hooper, L. Zhang, D. Wolverson, and V. K. Valev, "Raman techniques: Fundamentals and frontiers," *Nanoscale Research Letters*, vol. 14, pp. 1–34, 2019.

[95] L. M. Malard, M. A. Pimenta, G. Dresselhaus, and M. S. Dresselhaus, "Raman spectroscopy in graphene," *Physics Reports*, vol. 473, no. 5-6, pp. 51–87, 2009.

[96] H. Li, Q. Zhang, C. C. R. Yap, B. K. Tay, T. H. T. Edwin, A. Olivier, and D. Baillargeat, "From bulk to monolayer MoS_2: Evolution of raman scattering," *Advanced Functional Materials*, vol. 22, no. 7, pp. 1385–1390, 2012.

[97] C. Lee, H. Yan, L. E. Brus, T. F. Heinz, J. Hone, and S. Ryu, "Anomalous lattice vibrations of single-and few-layer MoS_2," *ACS Nano*, vol. 4, no. 5, pp. 2695–2700, 2010.

[98] M. O'Brien, N. McEvoy, C. Motta, J.-Y. Zheng, N. C. Berner, J. Kotakoski, K. Elibol, T. J. Pennycook, J. C. Meyer, C. Yim, M. Abid, T. Hallam, J. F. Donegan, S. Sanvito, and G. S. Duesberg, "Raman characterization of platinum diselenide thin films," *2D Materials*, vol. 3, no. 2, p. 021 004, 2016.

[99] A. Laturia, M. L. Van de Put, and W. G. Vandenberghe, "Dielectric properties of hexagonal boron nitride and transition metal dichalcogenides: From monolayer to bulk," *npj 2D Materials and Applications*, vol. 2, no. 1, p. 6, 2018.

[100] A. D. Liao, J. Z. Wu, X. Wang, K. Tahy, D. Jena, H. Dai, and E. Pop, "Thermally limited current carrying ability of graphene nanoribbons," *Physical Review Letters*, vol. 106, no. 25, p. 256 801, 2011.

[101] J. Berashevich and T. Chakraborty, "Doping graphene by adsorption of polar molecules at the oxidized zigzag edges," *Physical Review B*, vol. 81, no. 20, p. 205 431, 2010.

[102] X. Lin, J. Ni, and C. Fang, "Adsorption capacity of H_2O, NH_3, CO, and NO_2 on the pristine graphene," *Journal of Applied Physics*, vol. 113, no. 3, 2013.

[103] Winarto, E. Yamamoto, and K. Yasuoka, "Water molecules in a carbon nanotube under an applied electric field at various temperatures and pressures," *Water*, vol. 9, no. 7, p. 473, 2017.

[104] M. Awais Aslam, I. Stankovic, G. Murastov, A. Carl, Z. Song, K. Watanabe, T. Taniguchi, A. Lugstein, C. Teichert, R. Gorbachev, *et al.*, "Water induced ferroelectric switching: The crucial role of collective dynamics," *arXiv e-prints*, arXiv–2304, 2023.

[105] G. Murastov, M. A. Aslam, S. Leitner, V. Tkachuk, I. Plutnarová, E. Pavlica, R. D. Rodriguez, Z. Sofer, and A. Matković, "Multi-layer palladium diselenide as a con-

tact material for two-dimensional tungsten diselenide field-effect transistors," *Nanomaterials*, vol. 14, no. 5, p. 481, 2024.

CHAPTER 5
PUBLICATIONS

5.1 Single-crystalline nanoribbon network field effect transistors from arbitrary two-dimensional materials

M. Awais Aslam, Tuan Hoang Tran, Antonio Supina, Olivier Siri, Vincent Meunier, Kenji Watanabe, Takashi Taniguchi, Marko Kralj, Christian Teichert, Evgeniya Sheremet, Raul D. Rodriguez and Aleksandar Matkovic 2022. Single-crystalline nanoribbon network field effect transistors from arbitrary two-dimensional materials. npj 2D Materials and Applications, 6(1), p.76.

This work demonstrate an approach to fabricate 2D materials including Graphene, MoS_2, WS_2, WSe_2, hBN, and their heterostructures into nanoribbon networks. Small organic molecules deposited on 2D materials form nano-needles aligning in high-symmetry directions of the 2D material substrate which are used as masks. These hybrid heterostructures are plasma etched resulting in single-crystal nanoribbon networks composed of the remaining 2D material. Various characterization techniques are employed to verify the ribbons' network structural and transconductance properties. Ribbon-based Gr devices were found to exhibit pronounced gate dependent polarity switching, mimicking ferroelectric behaviour. The method opens a new avenue for straightforward production of 2D material nanoribbon network devices [71].

Status: Published in the peer-reviewed journal : npj 2D Materials and Applications.

Contribution of the author of the thesis: Prepared all the samples used in the study

for electrical, optical characterization and as well as for the decoration of nano-particles. Characterized the samples via optical spectroscopy, performed AFM/KPFM and electrical measurements. Carried out data analysis and evaluation. Prepared the figures and wrote the manuscript with the support of the co-authors.

npj | 2D materials and applications

www.nature.com/npj2dmaterials

ARTICLE OPEN

Single-crystalline nanoribbon network field effect transistors from arbitrary two-dimensional materials

Muhammad Awais Aslam [1] ✉, Tuan Hoang Tran [2], Antonio Supina [3], Olivier Siri [4], Vincent Meunier [5], Kenji Watanabe [6], Takashi Taniguchi [7], Marko Kralj [3], Christian Teichert [1], Evgeniya Sheremet [2], Raul D. Rodriguez [2] and Aleksandar Matković [1] ✉

The last decade has seen a flurry of studies related to graphene nanoribbons owing to their potential applications in the quantum realm. However, little experimental work has been reported towards nanoribbons of other 2D materials. Here, we propose a universal approach to synthesize high-quality networks of nanoribbons from arbitrary 2D materials while maintaining high crystallinity, narrow size distribution, and straightforward device integrability. The wide applicability of this technique is demonstrated by fabricating molybednum disulphide, tungsten disulphide, tungsten diselenide, and graphene nanoribbon field effect transistors that inherently do not suffer from interconnection resistance. By relying on self-aligning organic nanostructures as masks, we demonstrate the possibility of controlling the predominant crystallographic direction of the nanoribbon's edges. Electrical characterization shows record mobilities and very high ON currents despite extreme width scaling. Lastly, we explore decoration of nanoribbon edges with plasmonic particles paving the way for nanoribbon-based opto-electronic devices.

npj 2D Materials and Applications (2022)6:76 ; https://doi.org/10.1038/s41699-022-00356-y

INTRODUCTION

The successful synthesis of graphene nanoribbons (NRs)[1,2] and their implementation in devices[3,4] has brought them at the forefront as building blocks for information processing in quantum and classical electronics[5]. Graphene NRs enable various functionalities including tunable band gap, high current carrying capability, long mean free path, localized spin and topological edge states[5]. Similarly, other two-dimensional (2D) material NRs can display edge specific properties such as ferromagnetism[6,7], efficient catalysis[8,9], and enhanced sensing abilities[3,10]. Moreover, a recent study about MoS_2 NRs demonstrated their potential for spintronics and quantum transport[11]. The development of 2D material NRs is largely driven by the needs in nanoelectronics, where three-dimensional (3D) gate-all-around architectures that employ nanotubes, nanorods, or NRs are considered as the likely solution to the arising scaling challenges[12–14].

Despite all the possibilities that 2D material-based NRs hold, their sufficient quality, narrow widths, density, controlled edges, and high yield remain as technological challenges for realistic applications. The most widely used preparation methods are bottom-up chemical synthesis[15–18] and top-down lithography[19–21]. Chemical synthesis of NRs offers precise edge control and even allows synthesis of nanoporous graphene (NPG) ribbons with widths down to 1 nm. Such NPG systems are very appealing due to their ability to sieve as well as induce semiconducting behaviour in graphene[22,23]. However, bottom-up synthesis routes focus almost exclusively on graphene NRs, facing significant obstacles to develop more complex 2D materials or NR heterostructures. Moreover, the device channels suffer from electrical percolation issues and high junction (node) resistance[3]. Whereas, top-down lithography-based approaches do not offer a straight forward control over NR's alignment with respect to high symmetry directions of the 2D material. They also cause interface contamination thereby degrading device performance and operation[24].

Recently, Aljarb et al.[25] demonstrated a technique based on vicinal growth to fabricate NRs of arbitrary 2D materials e.g., (TMDCs). Although, the NRs produced by this approach are single crystals, the ribbon widths are rather large and non-uniform. The growth of these ribbons is also dependent on specific substrate, requiring an additional transfer step for their integration[25]. Vapour Liquid Solid (VLS) growth is another interesting method utilised for the NR synthesis[11,26]. Despite the fact that VLS uses silicon dioxide (SiO_2) as a substrate, it employs salt and metal precursors that can be detrimental for device integration.

In this work we tackle the outlined challenges and demonstrate a universal method to fabricate NRs of arbitrary 2D materials, including graphene, hexagonal boron nitride (hBN), transition metal dichalcogenides TMDCs, and nanoribbon heterostructures with a width ranging from 6 to 100 nm. Our approach is based on epitaxially-grown organic needle-like nanostructures which self assemble along high-symmetry directions of 2D materials. We exploited these organic nano-needles as a mask through which 2D materials could be etched by oxygen plasma. This results in crystalline nanoribbon-networks (NRNs) with high edge-to-surface ratio and controlled predominant crystallographic edge-directions. To investigate the electrical performance of our NRNs and to show a challenging technological application, field effect transistors (FETs) were directly fabricated on Si/SiO_2 and $Si/SiO_2/hBN$ substrates. Besides their inherent single-crystalline nature, NRN-FETs were obtained without any additional transfer steps. TMDC NRN-based devices show outstanding electrical properties, including WS_2 and WSe_2 nanoribbons. We also observed ferroelectric switching for graphene NR devices due to water

[1]Institute of Physics, Montanuniversität Leoben, Franz Josef Strasse 18, 8700 Leoben, Austria. [2]Tomsk Polytechnic University, Lenina ave. 30, 634034 Tomsk, Russia. [3]Center for Advanced Laser Techniques, Institute of Physics, Bijenička cesta 46, 10000 Zagreb, Croatia. [4]Aix Marseille University CNRS CINaM UMR 7325, Campus de Luminy 13288, Marseille cedex 09, France. [5]Department of Physics, Applied Physics, and Astronomy, Rensselaer Polytechnic Institute, Troy, NY 12180, USA. [6]Research Center for Functional Materials, National Institute for Materials Science, 1-1 Namiki, Tsukuba 305-0044, Japan. [7]International Center for Materials Nanoarchitectonics, National Institute for Materials Science, 1-1 Namiki, Tsukuba 305-0044, Japan. ✉email: muhammad.aslam@unileoben.ac.at; aleksandar.matkovic@unileoben.ac.at

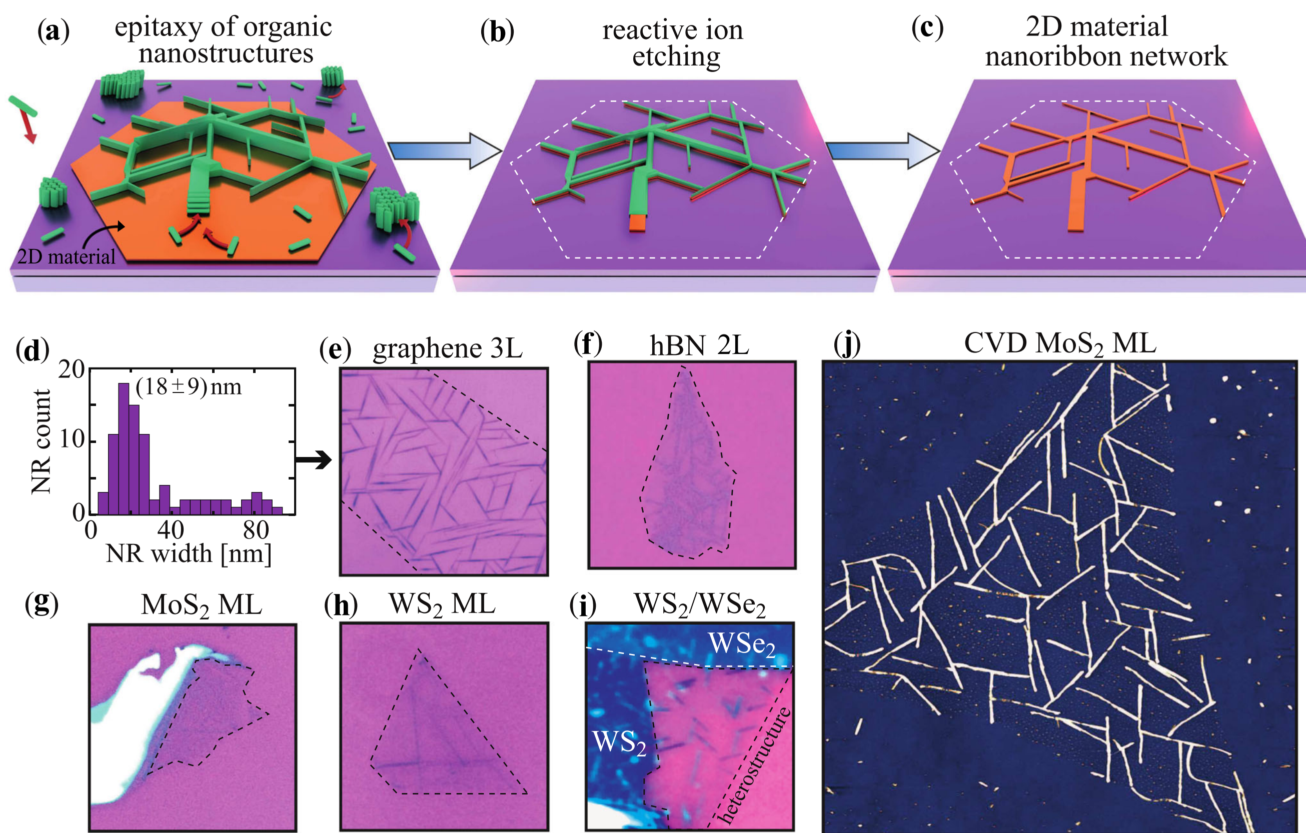

Fig. 1 Fabrication of 2D material NRNs. a–c Schematic representation of the key fabrication steps. **a** Organic nanostructures self-assembly and self-alignment. **b** After reactive ion etching. **c** NRN after removal of the sacrificial organic layer. **d** Histogram of NR widths for a graphene NRN shown in **e**. **e–i** Optical micrographs of various 2D material NRNs, presenting respectively NRNs of graphene, hBN, MoS_2, WS_2, and WS2/WSe2 heterostructure. **j** AFM topography image of a NRN from chemical vaopour deposition (CVD) Monolayer(ML) MoS_2 ($22 \times 22\ \mu m^2$, z-scale 15 nm).

adsorption at the ribbon edges[27]. Our proposed method allows ribbons which do not suffer from high node resistance between interconnecting NRs, as the networks are 'carved out' from single crystals. To confirm this, we employ *in operando* Kelvin probe force microscopy (KPFM). To demonstrate our methods scalability and ultimate control over the NR edge-direction, we have fabricated predominant armchair and zigzag NRNs from a large-area MoS_2 ML obtained by chemical vapor deposited (CVD). Such high edge-density in nanoribbon network field effect transistors (NRN-FETs) has potential benefits in sensing applications and in tunable catalytic devices, especially when considering catalytic edge reactivity of MoS_2[28,29]. To go one step further, we illustrate edge-specific decoration of NRNs with silver nanoparticles, creating mixed-dimensional plasmonic heterostructures.

RESULTS

Fabrication of NRNs

Figure 1a–c depict the proposed NRN fabrication pathway. Detailed steps for MoS_2 and graphene are given in Supplementary Fig. 1. Typically, NRs of about 10–30 nm width distribution were realized as shown in Fig. 1d. By further optimization of the growth time, etching time, or selection of organic nano-structures based on shorter back bone (e.g., bi-phenylenes), the mean NRN width can be changed. The tunability of the mean width has been demonstrated by changing the growth time and is presented in Supplementary Fig. 2.

Organic molecules grow on 2D materials via van der Waals (vdW) epitaxy[30]. The molecules at the interface with the 2D material substrate adopt a flat-lying orientation and align their π-networks to optimize vdW interaction with the substrate[31]. Consequently, the molecules at the interface are 'locked' into preferential adsorption sites on the substrate and the growing crystallites adopt rotational commensuration with their 2D material support. This provides an inherent self-alignment with the substrates' high symmetry directions, i.e., armchair or zig-zag[32–34].

After organic nanostructure growth, the hybrid organic/2D material stacks were precisely etched to form NRNs via exposure to oxygen plasma, i.e. reactive ion etching (RIE). An etch rate of ~1 layer in 3 s was established for graphene and TMDCs. Upon etching, the remaining organic molecules can either be left as an encapsulation layer[35] or removed by rinsing in chloroform or also by vacuum annealing. Our method allows for fabrication of monolithic NRNs of different exfoliated and CVD 2D materials, as demonstrated for graphene, hBN, MoS_2, WS_2 and WSe_2Fig. 1(e–j). Apart from individual 2D materials, in Fig. 1i we show NRN-heterostructures consisting of vertically stacked monolayer WS_2 (n-type) and bilayer WSe_2 (p-type), thus enabling atomically thin p-n junctions.

The structural integrity of NRs was probed by Raman and photoluminescence (PL) spectroscopies. Results for graphene NRs show extremely low values of (Intensity of the D peak/Intensity of the G peak) I_D/I_G peak ratios in the Raman spectra after etching of the flake into NRN (Supplementary Fig. 3 and Supplementary Table 1). Similarly, for ML MoS_2 (Supplementary Fig. 4) there are no defect activated peaks, which indicates high crystallinity of the fabricated nanoribbons. Figure 2a, b show results for the NR pairs (considering 3 layer MoS_2) with ~70° relative inclination. They exhibited a prominent difference in the intensities of E^1_{2g} and A_{1g}

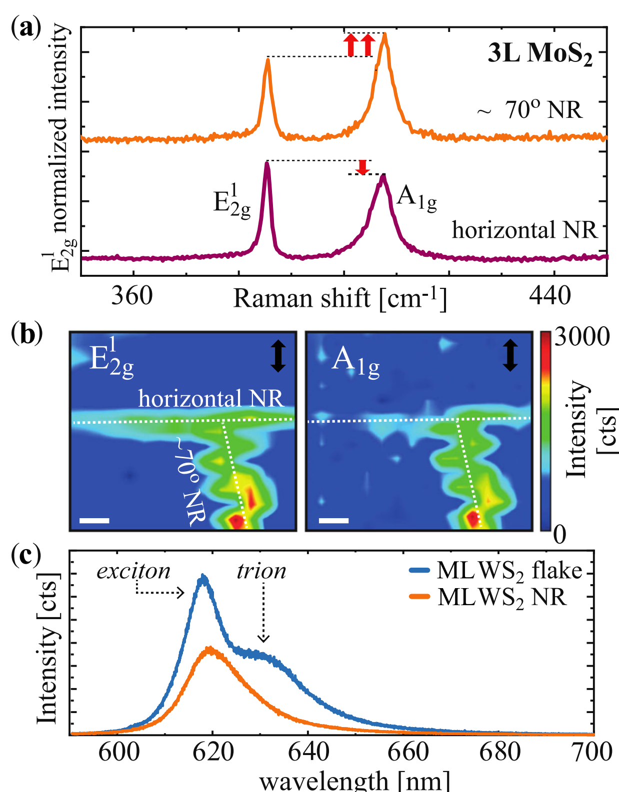

Fig. 2 Evidence of structural integrity of the NRs. **a** Raman spectra of the characteristic vibrational modes of MoS_2 showing the tri-layer flake before patterning, and two ribbons with ≈ 70° of relative inclination. The spectra are normalized with respect to the E^1_{2g}-mode intensity, and relative changes of the A_{1g} mode are indicated by horizontal dashed lines and red arrows. **b** Raman intensity maps of E^1_{2g} and A_{1g} modes of two intersecting NRs (scale-bar: 0.5 µm), highlighting a distinct variation of A_{1g} mode as the ribbon direction is changed. The direction of linearly polarized light is indicated by black arrows. This is in agreement with the published result that the relative intensity of the A_{1g} to E^1_{2g} peaks is strongly dependent on the orientation angle of the material's crystallographic axes, for a fixed in-plane polarization[60]. **c** PL spectra of a ML WS_2 flake and corresponding NR, highlighting exciton and trion components.

Raman active modes. Such anisotropy for Raman modes of MoS_2 NRs[36] and MoS_2 flakes[37] was previously observed by changing the polarization configuration. The intensity of a Raman mode is proportional to the dot product of the Raman tensor with the light polarization. Since the NRs of both directions are etched out of the same flake, their crystallographic orientation, and consequently the dot products are the same. Thus, this anisotropy cannot be explained by the selection rules per se. Raman spectra for rotated nanoribbons and flake are shown in (Supplementary Fig. 5). Anisotropy has an apparent effect on the relative A_{1g} mode intensity that warrants further investigation into its variations in narrow NRs. Furthermore, WS_2 NRs exhibited a dominant exciton peak and a suppressed trion peak in the PL measurements. This is due to a reduction in the free electron density over small widths (<30 nm) caused by the predominant oxygen terminated edges[38,39]. An example of the PL spectrum of WS_2 is presented in Fig. 2(c), comparing the initial ML flake and the resulting NR. The Raman spectra for the nanoribbon WS_2/WSe_2 heterostructure is provided in the (Supplementary Fig. 6).

Predominant crystallographic orientations of nanoribbons

To demonstrate that our proposed method offers control of NRs predominant crystallographic orientation, two different organic molecules—parahexaphenyl (6P) and dihydrotetraazaheptacene (DHTA7)—were grown epitaxially on ML MoS_2 obtained by CVD. As their phenylene (6P) and acene (DHTA7) backbones could be seen as armchair and zig-zag motifs, respectively, and upon adsorption, molecular backbones will align with the corresponding high-symmetry directions of the 2D material substrate[34,40,41]. The control over the orientation of the predominant NR direction can be verified by using triangular CVD MoS_2 flakes that terminate with zig-zag edges due to the growth kinetics[42–44]. Figure 3a, b compares the NR directions and the triangular MoS_2 flake-edge directions, presenting 2D Fast Fourier Transform (2D-FFT) analysis of the atomic force microscopy (AFM) topography images (corresponding insets). In the case of 6P masks (Fig. 3a), predominant NR directions are tilted by (8.5 ± 0.4)° from the edge directions, i.e., NR edges are close to parallel with the zigzag crystallographic direction. By altering the backbone of the molecular mask (the case of DHTA7—Fig. 3b) the NR edges change predominantly following the armchair crystallographic direction. Moreover, employing other molecular species could allow controlling this angle for a particular 2D material of interest, and to exploit orientation specific properties for 2D materials[45,46] in the one-dimensional NR-regime.

TMDC-NRN field effect transistors

Field-modulation of the NRNs was tested by fabricating two-terminal field-effect transistors (FETs) and investigating their transfer characteristics source-drain current *vs* source gate voltage $I_D(V_{SG})$ at 77 K and 300 K. Van der Waals graphite electrodes were employed to probe electrical response of the devices between each step of the fabrication. Our proposed NRN fabrication method is compatible with conventional two-dimensional field effect transistor (2D-FET) fabrication schemes (as mask-lithography or e-beam lithography) since the 2D material films can be patterned into NRNs prior to the electrode fabrication. Figure 4a presents the scheme of the device geometry, and an optical micrograph for one of the WS_2-NRN-FETs in the inset.

Figure 4b–d provide typical semi-logarithmic transfer curves at 300 K for flakes with organic nanostructures for WS_2, MoS_2, and WSe_2, respectively and after patterning them into NRs. For WSe_2 10–15 nm hBN was used for bottom capping and NRN was patterned on top of it. MoS_2 and WS_2 devices exhibit an n-type behaviour whereas WSe_2 exhibited an ambipolar behaviour, both before and after patterning of the flakes into NRNs. A shift in the positive V_{SG} direction of the $I_D(V_{SG})$ curves was observed after NRN formation, indicating *p*-type doping by the RIE process. On average, $I_D(V_{SG})$ curves for MoS_2 devices showed a positive shift of 40 V after the NRN formation. This large positive shift can be attributed to electron depletion by the oxygen terminating NR-edges[47].

The devices exhibited exceptional transfer characteristics even when SiO_2 was used as the gate dielectric. The performance of NRN-FETs could be further enhanced by employing high-*K* dielectric materials such as HfO_2[48]. An increase in the hysteresis was observed in the NR devices (except WSe_2) which can be due to two possible mechanisms including high density of edges facilitating charge trapping/de-trapping mechanisms from adosrbates[20] or increased capacitive gating effect-traps due to SiO_2[49]. To investigate the origin of hysteresis the devices were annealed in vacuum at 400K which lead to reduction of hysteresis due to removal of adsorbates on the edges[50]. However, a full closure of the hysteresis was noted by performing low temperature measurements (77 K) as shown in (Supplementary Fig. 7) which points towards capacitive gating as the possible reason[49].

Compared to the unetched flakes, the NRN-devices experienced a decrease of the I_D, as a consequence of the severely reduced channel widths when compared to the original 2D material-FET[47]. An increase in I_D and mobilities was observed when NRN-FETs are

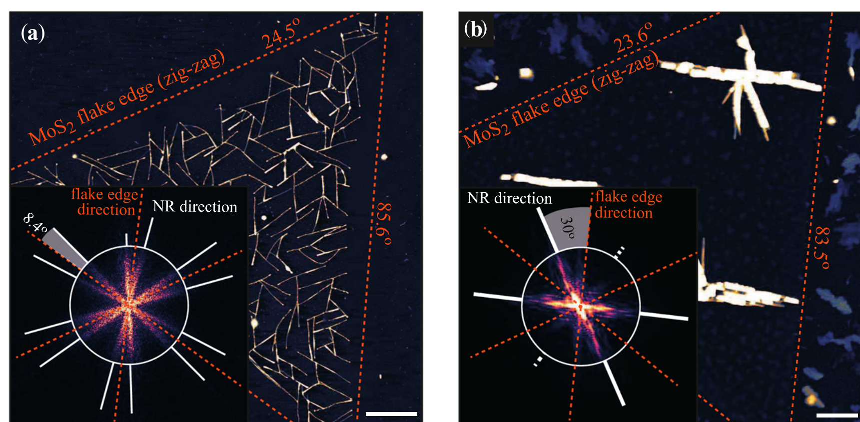

Fig. 3 Orientation control of nanoribbons. **a** (scale-bar: 5 μm) CVD MoS_2 NRN with ribbons nearly parallel to the flake edges (zigzag direction), using 6P molecules for the self-assembled mask. Inset shows 2D-FFT analysis of the NR directions with respect to the triangular flake edges. 2D Fast Fourier Transform (2D-FFT) image is rotated by 90° to represent real-space directions. **b** (scale-bar: 1 μm) Similar to **a** only using DHTA7 molecules for the self-assembled mask, and resulting in NRs in armchair direction (perpendicular to flake edges).

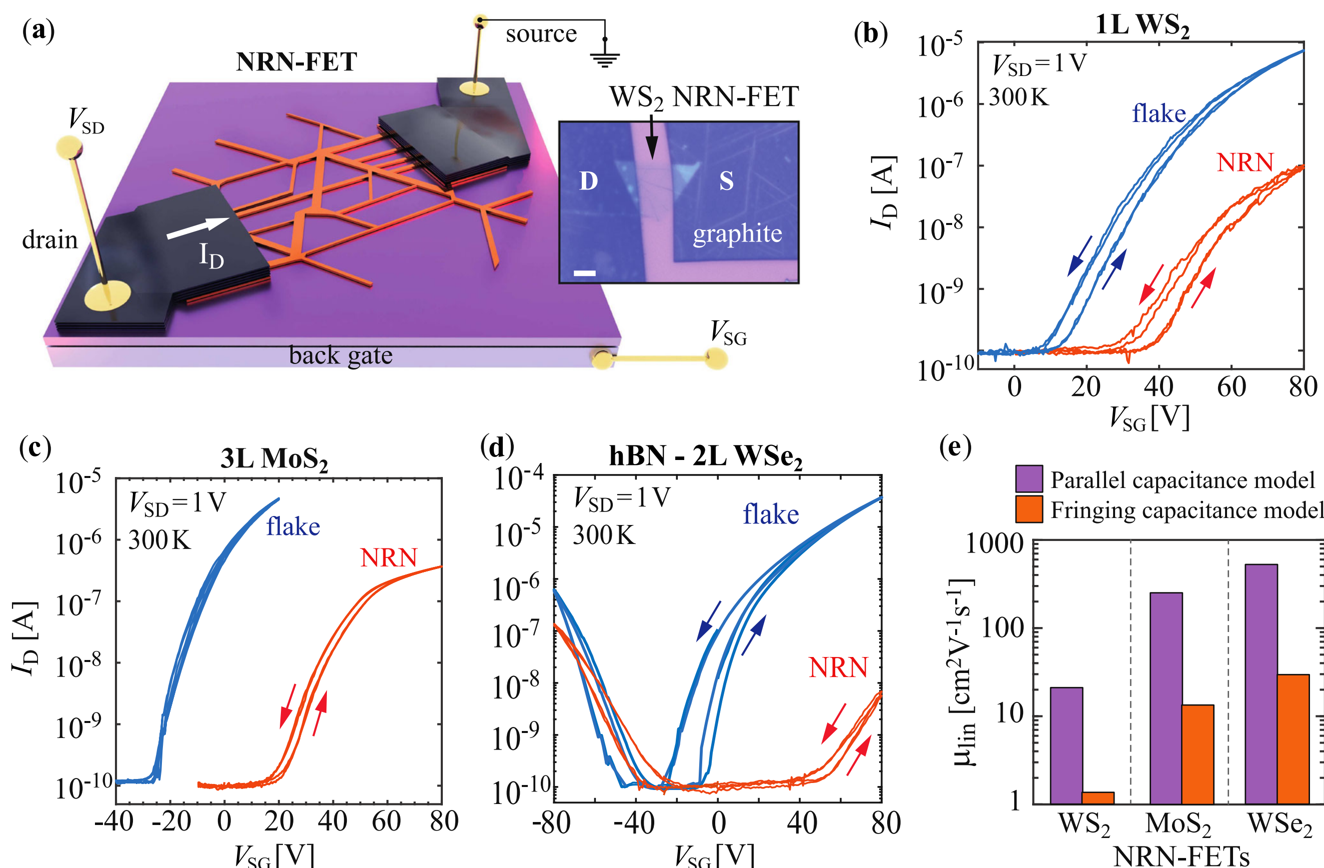

Fig. 4 TMDC-NRN-FETs. **a** Schematic diagram of a NRN-based FET utilizing vdW graphite electrodes. Inset of **a** shows an optical micrograph of a 3L WS_2 FET (scale-bar 5 μm). **b**–**d** Semi-logarithmic transfer curves of WS_2, MoS_2, and hBN-WSe_2 FETs before and after patterning the flakes into NRNs. **e** Parallel and fringing capacitance apparent linear electron mobilities at 77 K, for the devices presented in **b**–**d**.

measured at low temperature (77 K). These observations confirm the presence of band transport in NRNs, as at low temperatures the contribution from phonons are minimized (Supplementary Fig. 8).

Figure 4e summarizes the apparent linear electron mobilities (μ) obtained from the $I_D(V_{SG})$ curves measured at 77 K and calculated both by parallel and fringing capacitance models. Mobility plots are shown in Supplementary Fig. 8. The commonly used parallel capacitance model overestimates the mobilities when applied to NRs as their widths are much smaller compared to the oxide thickness[11]. Therefore, taking into account the capacitance per unit area for the fringing capacitance model[51], a more realistic area-specific gate capacitance can be expressed as:

$$C_{ox} \approx \varepsilon_{ox}\varepsilon_0 \left\{ \frac{\pi}{\ln\left[6\left(\frac{t_{ox}}{W}+1\right)\right]W} + \frac{1}{t_{ox}} \right\} \quad (1)$$

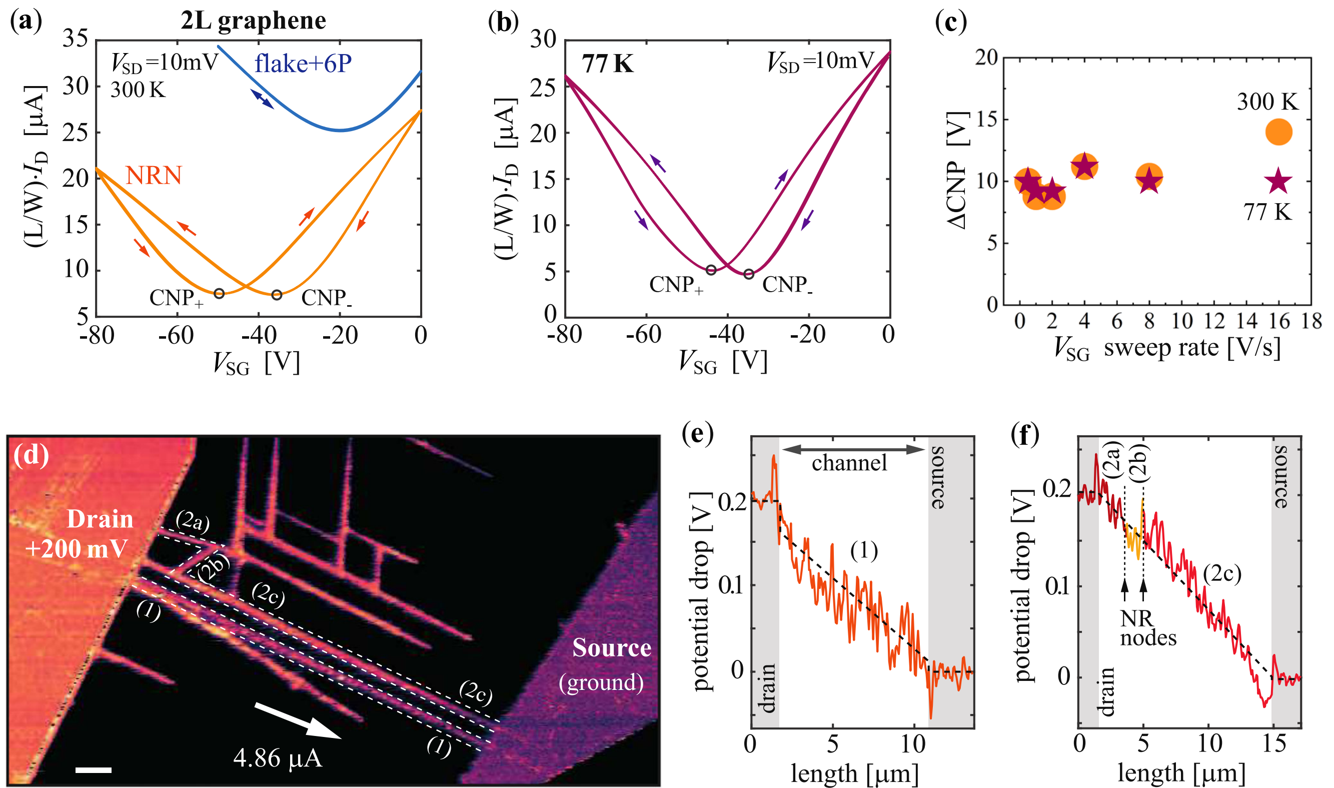

Fig. 5 Graphene NRN-FETs. a Length and width scaled transfer curves of the bi-layer graphene flake after organic nanostructure growth, and of the corresponding NRN-FET after annealing. Forward and reverse sweep direction is indicated by the arrows. **b** Length and width scaled transfer curves for graphene NRN-FET at 77 K, demonstrating that bi-modal switching persists at low temperature. **c** Difference in the forward and reverse bias charge neutrality point (CNP) positions as a function of the V_{SG} sweeping rate. **d** *in operando* FM-KPFM image of a graphene NRN-FET (scale-bar: 1 μm). Potential profile lines from the ribbons indicated by (1) and (2a–c) in sub-panel **d** are presented in **e** and **f**, respectively.

where t_{ox} is the oxide thickness and W is channel width. Effective channel length and width were estimated considering parallel and serial connections of NRs for each particular NRN-FET.

Graphene NRN-FETs and edge-induced ferroelectric effect

Besides very high mobilities ≈ 1000–1200 $cm^2V^{-1}s^{-1}$ (using the fringing capacitance model) graphene-based NRN devices exhibit pronounced hysteresis in the $I_D(V_{SG})$, see Fig. 5(a). The observed hysteresis ΔCNP (difference between two CNPs) was not present in the original flakes, nor is introduced by the deposited organic nano-structures. The effect appears after the RIE in oxygen plasma once the samples are exposed to the ambient environment. This exposure allows the attachment of water molecules from the air to the oxygenated edges of the nanoribbons. The hysteresis remains in high-vacuum, at low temperatures Fig. 5b, and is practically independent of the V_{SG} sweep-rates Fig. 5c. Similar effect was predicted for edge-adsorbed water molecules and was observed for graphene-FETs with oxygen-plasma etched edges[27]. The orientation of water molecules can be changed due to the torque induced by the external electric field. The total field experienced by the graphene NRN is a sum of the gate-bias induced field and the net field produced by the edge-adsorbed water dipoles, yielding a robust bi-modal—ferroelectric—behavior of graphene NRN-FETs.

To rule out any causes of hysteresis due to trap-states the devices were measured in high vacuum (10^{-7} mbar), after vacuum annealing (at 410K for over 90 min), and were subjected to low temperature (77 K) measurements. In all cases, the observed hysteresis was preserved. As the trapping is sensitive to temperature a significant quenching would occur at low temperature[52,53]. This was observed for TMDC-based NRN-FETs, where the bi-stable states of the adsorbed water molecules at the ribbon edges are not expected. For graphene NRN-FETs at 77 K the hysteresis of the transfer curves is only slightly reduced as shown in Fig. 5b. In addition, V_{SG} sweep-rate dependent measurements were carried out both at 300 K and at 77 K. Figure 5c presents the V_{SG} sweep-rate dependence of the ΔCNP, representing the negligible difference in the CNP position for the forward and the backward sweeps. This further helps us excluding any contributions from capacitive gating which acts on seconds time scale[52]. Lastly, to identify the temperature required for water dissociation from graphene NR edges the devices were annealed for various temperatures (373 K, 473 K and 573 K) under vacuum conditions. A large reduction of the hysteresis was observed after annealing the devices at 573 K (Supplementary Fig. 9) whereas no significant changes to the hysteresis were observed for lower temperature. A shift of the CNP towards negative V_{SG} was also noted. This is a direct indication of water removal which otherwise causes a p-type doping of graphene[54]. Our results point to the induced ferroelectric effect in oxygen-terminated graphene nanoribbon-FETs, which is very similar and more robust than observed previously for the oxygen-terminated flake-edges[27]. While ferroelectric-graphene nanoribbons and their integration into heterostructures are very interesting and promising pathways for future nanoelectronics, optoelectronics, neuromorphic electronics, and sensing applications, such research is beyond the scope of this study. To directly probe the resistivity of the nodes between the adjacent NRs and the potential drops across the NRN-FET channel *in operando* frequency modulated (FM) KPFM was performed on graphene NRN-FETs. Figure 5d presents a

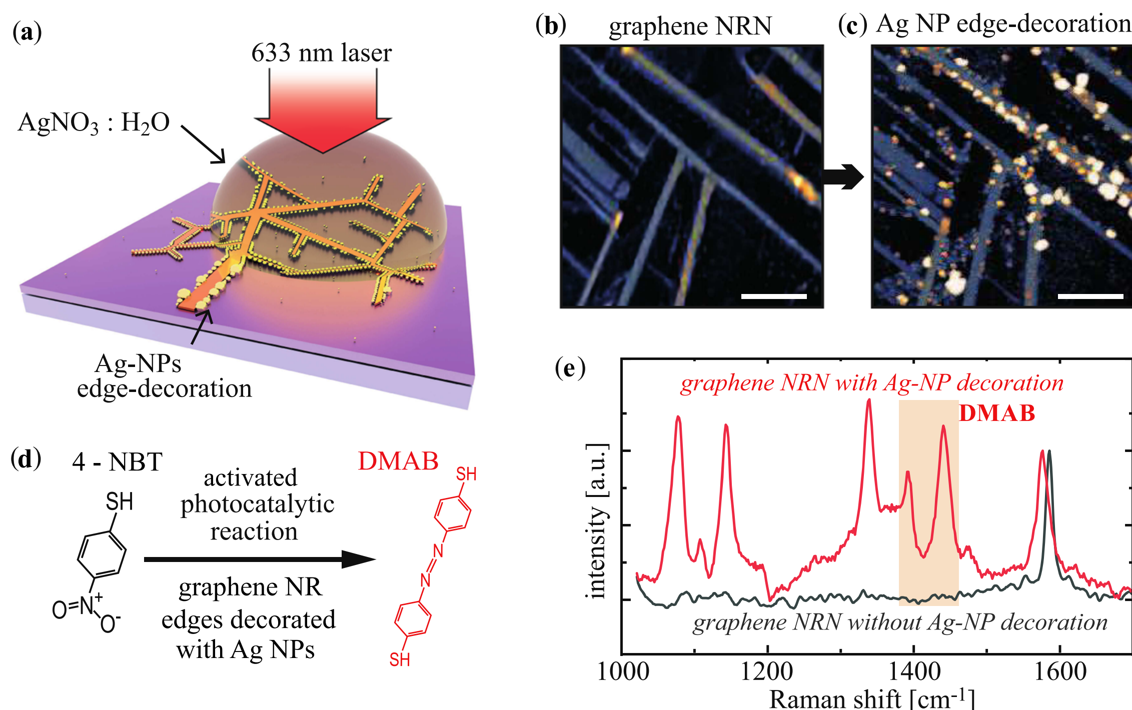

Fig. 6 Decoration of nanoribbon edges. a Illustration of the process for the decoration of the NRNs with metallic nanoparticles, and (**b**, **c**) graphene NRN before and after edge-decoration with Ag NPs (scale bars 500 nm, z-scales 25 nm). **d** Dimerization of 4-NBT to DMAB and (**e**) demonstration of the photocatalytic activity and (surface-enhanced raman spectroscopy) SERS capability of the hybrid graphene-NRN + Ag-NP system.

contact potential difference (CPD) map across a graphene NRN-FET during operation.

To highlight the relevant potential drops across the channel, cross-sections marked in Fig. 5d are provided in Fig. 5(e, f). The transitions from the electrodes to the channel do not introduce any significant potential drops, as seen earlier for gold electrodes on both graphene and MoS_2[55,56]. Graphene NR labeled (1) interconnects between the source and drain electrodes, it exhibits an almost perfectly linear potential drop across the 10 µm long channel Fig. 5e. NRs labeled (2a–c) form a parallel connection to NR (1). No potential drop was observed at the nodes between (2a)-(2b) and (2b)–(2c), as indicated in Fig. 5f. Further, many more ribbons that do not bridge the source and drain electrodes, maintain a constant potential as these are not part of the current flow across the device. Above all, the consistent potential observed at all nodes is due to the translation of single-crystallinity of the original 2D material into the nanoribbon network. By not suffering from high node resistance, most of the potential drop of the provided V_{SD} bias is utilized for the transport along the NRs in the channel (Fig. 5d–f). As a consequence, our NRN FETs exhibit high on state currents and allow for high current modulation by the gate.

Decoration of nanoribbons with plasmonic particles

To demonstrate high edge-to-surface ratio of our 2D material nanoribbon networks, we investigated edge-specific decoration of the NRs by metallic nanoparticles (NPs). Figure 6a schematically presents the decoration process. The details are provided in the methods section. The NR edges induce selective nucleation of Ag nanoparticles via the photo-activated reduction of Ag ions at the edges via electron transfer from graphene. Figure 6b, c present a graphene NRN before and after decoration with Ag NPs. Edge-specific decoration of 2D materials with metallic NPs was already demonstrated[57], and utilizing NRN enhances the benefits of these hybrid systems.

To investigate the photocatalytic activity of the edge-decorated NPs, we use 4-nitrobenzenethiol (4-NBT) as a model for photocatalysis experiment. This is shown in Fig. 6d. The photocatalytic conversion of 4-NBT to p,p'-dimercaptoazobenzene (DMAB) has been intensively investigated[58]. Both Ag NP-decorated and bare graphene NRs were exposed to the solution of 4-NBT, and the resulting Raman spectra are shown in Fig. 5e. Without the NPs only the G-mode of the graphene NRs can be observed. However, edge decorated NPs not only enable surface-enhanced raman spectroscopy (SERS) signal, but also induce the desired photocatalytic reaction of 4-NBT into DMAB, as evident from the appearance of the DMAB characteristic Raman mode at ~1440 cm^{-1} and ~1390 cm^{-1}.These Raman modes are related to ag_{16} and ag_{17} vibrations of N=N of DMAB[58]. Such a photocatalytic reaction on nanoribbons decorated with plasmonic nanoparticles shows its future potential towards photocatalytic applications. In further studies, we will focus on employing 2D material-based NRN-FETs combined with edge-specific decorated plasmonic NPs, gaining an additional 'knob' via gate biasing. Such coupled mixed-dimensional plasmonic systems can be utilised in gate-controlled photocatalytic reactions, tunable SERS sensors, and high-sensitivity optoelectronic devices, however such experiments would go beyond the scope of this study.

DISCUSSION

We propose a method to fabricate nanoribbon networks starting from arbitrary 2D materials, including WS_2 and WSe_2 NRs, and their heterostructures, which were not demonstrated until now. The method allows achieving NR widths below 20 nm while also enabling a straight-forward integration of the 2D material based NRNs into high-performance FETs with high yields of nanoribbon (Supplementary Table 2 and Supplementary Fig. 10). Further, with the appropriate choice of the self-aligned molecular masks control of the NR direction with respect to the crystallographic high-symmetry directions is achieved. Examined TMDC nanoribbon

network FETs exhibit band transport, maintain high carrier mobility values, clear off-states, high ON-state currents, and maintain stable operation over a large number of sweeping cycles (Supplementary Fig. 11).

By bridging between top-down and bottom-up approaches, our method provides high-quality NR connections (nodes) that do not act as scattering centers (high resistivity points), as proven by *in operando* KPFM of graphene-NRN FETs. Further, using graphene-NRN FETs we show bi-modal switching of the transfer curves which has been theoretically predicted, and thus far demonstrated only for graphene edges[27]. By Raman spectroscopy we have observed that MoS_2 ribbons with the different growth directions exhibit Raman anisotropy[36]. Our method facilitates both high crystallinity and large-area coverage without the high resistance issues of the adjacent nanoribbon nodes. In comparison, the bottom up approaches usually suffer from percolation and node resistance issues[3], while the top-down approaches tend to introduce defects[24] in the ribbons yielding lower crystallinity.

Lastly, the high edge-to-surface ratios of our NRNs allowed us to selectively decorate the edges with plasmonic nanoparticles. These hybrid mixed-dimensional systems can provide a platform for next generation optoelectronic and plamsonic sensing devices due to the flexibility provided by our method for size tuning of the nanoribbons and the applicability of the process to heterostructures and vertical 2D material p-n junctions.

METHODS

2D materials, organic masks, and device fabrication

Flakes of 2D materials were mechanically exfoliated from bulk crystal and transferred onto a 300 nm SiO_2/Si substrate using commercially available Nitto tape and polydimethylsiloxane (Gel-Pak-DLG-X4). Monolayer and few layer flake thicknesses were identified via optical contrast, PL, and Raman measurements. Graphite flakes 10–50 nm thick kish graphite) were then transferred on 2D materials as electrodes to make device channels. 6P and DHTA7 nanostructures were grown on devices/flakes by hot wall epitaxy. The growth procedures were adopted from refs. [34,41]. MoS_2 triangular flakes were grown from solution-based CVD at atmospheric pressure similarly to the procedure in ref. [59]. The liquid Mo precursors used were NaMo and AHM in 1:1 ratio and dissolved in ultra-pure water at concentration of 200 ppm.

Reactive ion etching

The reactive ion etching process was developed using an Oxford Plasma 80 plus RIE system. For all devices the forward power was kept at 80 W with an oxygen flow of 50 sccm under a pressure of 40 mTorr. Etching time was optimized according to the thickness of 2D materials.

Electrical characterization

Electrical characterization of the flake- and NRN-FETs were done using Keithley 2636A Source-Meter attached to the Instec probe station. The samples were contacted with Au coated Ti electrical cantilever microprobes. Low temperature electrical measurements were performed using liquid nitrogen on a silver plate for thermal uniformity. The temperatures were monitored via mK2000 temperature controller connected to the probe station with a temperature resolution of 0.01 K.

AFM and FM-KPFM Measurements

AFM and FM-KPFM measurements were performed using Horiba/AIST-NT Omegascope AFM system. Aseylec probes were employed (spring constant ~ 42 N/m, resonant frequency ~ 70 kHz, tip radius below 30 nm). For width measurements 'Nanosensors' probes were used (spring constant of 10–130 N/m, resonant frequency ~ 300 kHz and tip radius of 2 nm). For *in-operando* FM-KPFM experiments, the graphene-NRN-FETs were controlled by a Keithley 2636A sharing the same ground with the KPFM-setup. FM-KPFM measurements were carried out in a two-pass mode, with the probe lifted by 12 nm in the second pass. Topography and CPD images were processed in the open-source software Gwyddion v2.56. For topography images zero-order line filtering was applied and leveling of the base plane. For CPD images only zero order line filtering was applied.

Micro-PL Measurements

All micro-PL and Raman measurements were performed using a Horiba LabRam HR Evolution confocal Raman spectrometer using 600 lines/mm and 1800 lines/mm gratings. A 532 nm laser source was used to excite the samples with an excitation power of 0.1–3.2 mW. The laser spot was focused by a 100 ×, 0.9 NA objective.

NP edge-decoration and photocatalysis experiments

Ag deposition on graphene nanoribbons was carried out by photo-deposition method. 10 µl of 1 mM $AgNO_3$ was dropped on the sample. Thin glass was placed on top of the sample for ease of finding the region of interest. Red laser (633 nm) and objective 100x were used to irradiate the sample. Laser power, laser scanning speed and area were optimized to control the size of Ag NPs. For photocatalytic experiment, 0,1 mM 4-NBT with water to ethanol ratio 50:50 was prepared. Nanoribbon networks decorated with Ag NPs was immersed in this solutions overnight. After that, sample was washed and Raman spectra were recorded with NT-MDT Raman spectroscope.

DATA AVAILABILITY

Correspondence and the requests for the data and/or materials should be addressed to Aleksandar Matković.

Received: 11 June 2022; Accepted: 14 October 2022;
Published online: 31 October 2022

REFERENCES

1. Li, X., Wang, X., Zhang, L., Lee, S. & Dai, H. Chemically derived, ultrasmooth graphene nanoribbon semiconductors. *Science* **319**, 1229–1232 (2008).
2. Cai, J. et al. Graphene nanoribbon heterojunctions. *Nat. Nanotechnol.* **9**, 896–900 (2014).
3. Chen, Z., Narita, A. & Müllen, K. Graphene nanoribbons: on-surface synthesis and integration into electronic devices. *Adv. Mater.* **32**, 2001893 (2020).
4. Saraswat, V., Jacobberger, R. M. & Arnold, M. S. Material science challenges to graphene nanoribbons. *ACS Nano* **15**, 3674–3708 (2021).
5. Wang, H. et al. Graphene nanoribbons for quantum electronics. *Nat. Rev. Phys.* **3**, 791–802 (2021).
6. Pan, H. & Zhang, Y. W. Edge-dependent structural, electronic and magnetic properties of MoS_2 nanoribbons. *J. Mater. Chem.* **22**, 7280–7290 (2012).
7. Slota, M. et al. Magnetic edge states and coherent manipulation of graphene nanoribbons. *Nature* **557**, 691–695 (2018).
8. Lin, J. et al. Enhanced electrocatalysis for hydrogen evolution reactions from WS_2 nanoribbons. *Adv. Energy Mater.* **4**, 1301875 (2014).
9. Karunadasa, H. I. et al. A molecular MoS_2 edge site mimic for catalytic hydrogen generation. *Science* **335**, 698–702 (2012).
10. Lihter, M. et al. Electrochemical functionalization of selectively addressed MoS_2 nanoribbons for sensor device fabrication. *ACS Appl. Nano Mater.* **4**, 1076–1084 (2021).
11. Li, X. et al. Nickel particle enabled width-controlled growth of bilayer molybdenum disulfide nanoribbons. *Sci. Adv.* **7**, eabk1892 (2021).
12. Thomas, S. Gate-all-around transistors stack up. *Nat. Electron.* **3**, 728–728 (2020).
13. Chen, M. L. et al. A FinFET with one atomic layer channel. *Nat. Commun.* **11**, 1–7 (2020).

14. Xu, L. Can carbon nanotube transistors Be scaled down to the sub-5 nm gate length? *ACS Appl. Mater. Interfaces* **13**, 31957–31967 (2021).
15. Jia, X., Campos-Delgado, J., Terrones, M., Meunier, V. & Dresselhaus, M. S. Graphene edges: a review of their fabrication and characterization. *Nanoscale* **2**, 86–95 (2011).
16. Barone, V., Hod, O. & Scuseria, G. E. Electronic structure and stability of semiconducting graphene nanoribbons. *Nano Lett.* **6**, 2748–2754 (2006).
17. Jolly, A., Miao, D., Daigle, M. & Morin, J. F. Emerging bottom-up strategies for the synthesis of graphene nanoribbons and related structures. *Angew. Chem.* **132**, 4652–4661 (2020).
18. Bennett, P. B. et al. Bottom-up graphene nanoribbon field-effect transistors. *Appl. Phys. Lett.* **103**, 253114 (2013).
19. Han, M. Y., Özyilmaz, B., Zhang, Y. & Kim, P. Energy band-gap engineering of graphene nanoribbons. *Phy. Rev. Lett.* **98**, 206805 (2007).
20. Chen, S. et al. Monolayer MoS_2 nanoribbon transistors fabricated by scanning probe lithography. *Nano Lett.* **19**, 2092–2098 (2019).
21. Tapasztó, L., Dobrik, G., Lambin, P. & Biro, L. P. Tailoring the atomic structure of graphene nanoribbons by scanning tunnelling microscope lithography. *Nat. Nanotechnol.* **3**, 397–401 (2008).
22. Moreno, C. et al. On-surface synthesis of superlattice arrays of ultra-long graphene nanoribbons. *Chem. Commun.* **54**, 9402–9405 (2018).
23. Moreno, C. et al. Bottom-up synthesis of multifunctional nanoporous graphene. *Science* **360**, 199–203 (2018).
24. Zhou, Y. & Loh, K. P. Making patterns on graphene. *Adv. Mater.* **22**, 3615–3620 (2010).
25. Aljarb, A. Ledge-directed epitaxy of continuously self-aligned single-crystalline nanoribbons of transition metal dichalcogenides. *Nat. Mater.* **19**, 1300–1206 (2020).
26. SLi, S. Vapour-liquid-solid growth of monolayer MoS_2 nanoribbons. *Nat. Mater.* **17**, 535-542, (2018).
27. Caridad, J. M. et al. A graphene-edge ferroelectric molecular switch. *Nano Lett.***18**, 4675–4683 (2018).
28. Salazar, N., Rangarajan, S., Rodríguez-Fernández, J., Mavrikakis, M. & Lauritsen, J. V. Site-dependent reactivity of MoS_2 nanoparticles in hydrodesulfurization of thiophene. *Nat. Commun.* **11**, 1–9 (2020).
29. Wang, H. et al. Structural and electronic optimization of MoS_2 edges for hydrogen evolution. *J. Am. Chem. Soc.* **141**, 18578–18584 (2019).
30. Koma, A. Van der Waals epitaxy for highly lattice-mismatched systems. *J. Cryst. Growth* **201**, 236–241 (1999).
31. Hlawacek, G., Khokhar, F. S., van Gastel, R., Poelsema, B. & Teichert, C. Smooth growth of organic semiconductor films on graphene for high-efficiency electronics. *Nano Lett.* **11**, 333–337 (2011).
32. Matković, A. et al. Epitaxy of highly ordered organic semiconductor crystallite networks supported by hexagonal boron nitride. *Sci. Rep.* **6**, 1–10 (2016).
33. Wang, J. Probing the crystallographic orientation of two-dimensional atomic crystals with supramolecular self-assembly. *Nat. Commun.* **8**, 1–8 (2017).
34. Vasić, B. et al. Molecules on rails friction anisotropy and preferential sliding directions of organic nanocrystallites on two-dimensional materials. *Nanoscale* **10**, 18835–18845 (2018).
35. Ha, T. J., Akinwande, D. & Dodabalapur, A. Hybrid graphene/organic semiconductor field-effect transistors. *Appl. Phys. Lett.* **101**, 033309 (2012).
36. Wu, J. B. et al. Monolayer molybdenum disulfide nanoribbons with high optical anisotropy. *Adv. Opt. Mater.* **4**, 756–762 (2016).
37. Ji, J. et al. Giant magneto-optical Raman effect in a layered transition metal compound. *PNAS* **113**, 2349–2353 (2016).
38. Cong, C., Shang, J., Wang, Y. & Yu, T. Optical properties of 2D semiconductor WS_2. *Adv. Opt. Mater.* **6**, 1700767 (2018).
39. Kwon, Y., Kim, K., Kim, W., Ryu, S. & Cheong, H. Variation of photoluminescence spectral line shape of monolayer WS_2. *Curr. Appl. Phys.* **18**, 941–945 (2012).
40. Kratzer, M., Matkovic, A. & Teichert, C. Adsorption and epitaxial growth of small organic semiconductors on hexagonal boron nitride. *J. Phys. D: Appl. Phys.* **52**, 383001 (2019).
41. Matković, A. et al. Light assisted charge propagation in networks of organic semiconductor crystallites on hexagonal boron nitride. *Adv. Funct. Mater.* **29**, 1903816 (2019).
42. Van Der Zande, A. M. et al. Grains and grain boundaries in highly crystalline monolayer molybdenum disulphide. *Nat. Mater.* **12**, 554–561 (2013).
43. Zhu, D. et al. Capture the growth kinetics of CVD growth of two-dimensional MoS_2. *npj 2D Mater. Appl.* **1**, 1–8 (2017).
44. Zhou, W. et al. Intrinsic structural defects in monolayer molybdenum disulfide. *Nano Lett.* **13**, 2615–2622 (2013).
45. Li, F. et al. Strain improving the performance of a flexible monolayer MoS_2 photodetector. *Adv. Electron. Mater.* **12**, 1900803 (2019).
46. Arab, A. & Li, Q. Anisotropic thermoelectric behavior in armchair and zigzag mono- and fewlayer MoS_2 in thermoelectric generator application. *Sci. Rep.* **5**, 1–12 (2015).
47. Liu, H., Gu, J. & Peide, D. Y. MoS_2 nanoribbon transistors transition from depletion mode to enhancement mode by channel-width trimming. *IEEE Electron Device Lett.* **33**, 1273–1275 (2012).
48. Lee, G. H. et al. Flexible and transparent MoS_2 field-effect transistors on hexagonal boron nitride-graphene heterostructures. *ACS Nano* **7**, 7931–7936 (2013).
49. Park, Y., Baac, H. W., Heo, J. & Yoo, G. Thermally activated trap charges responsible for hysteresis in multilayer MoS_2 field-effect transistors. *App. Phys. Lett.* **108**, 083102 (2016).
50. Kaushik, N. et al. Reversible hysteresis inversion in MoS_2 field effect transistors. *npj 2D Mater. Appl.* **1**, 1–9 (2017).
51. Liao, A. D. et al. Thermally limited current carrying ability. *Phys. Rev. Lett.* **106**, 256801 (2011).
52. Wang, H., Wu, Y., Cong, C., Shang, J. & Yu, T. Hysteresis of electronic transport in graphene transistors. *ACS Nano* **4**, 7221–7228 (2010).
53. Singh, A. K. & Gupta, A. K. Reversible control of doping in graphene-on-SiO_2 by cooling under gate-voltage. *J. Appl. Phys.* **122**, 195305 (2017).
54. Melios, C., Giusca, C. E., Panchal, V. & Kazakova, O. Water on graphene review of recent progress. *2D Mater.* **5**, 022001 (2018).
55. Yu, Y. J. et al. Tuning the graphene work function by electric field effect. *Nano Lett.* **9**, 3430–3434 (2009).
56. Matković, A. et al. Interfacial band engineering of MoS_2/Gold interfaces using pyrimidine-containing self-assembled monolayers toward contact-resistance-free bottom-contacts. *Adv. Electron. Mater.* **6**, 2000110 (2020).
57. Tanaka, N., Nishikiori, H., Kubota, S., Endo, M. & Fujii, T. Photochemical deposition of Ag nanoparticles on multiwalled carbon nanotubes. *Carbon* **47**, 2752–2754 (2009).
58. Dong, B., Fang, Y., Xia, L., Xu, H. & Sun, M. Is 4-nitrobenzenethiol converted to p, p'-dimercaptoazobenzene or 4-aminothiophenol by surface photochemistry reaction? *J. Raman Spectrosc.* **42**, 1205–1206. (2011).
59. Marion, I. D. et al. Atomic-scale defects and electronic properties of a transferred synthesized MoS_2 monolayer. *Nanotechnology* **29**, 305703 (2018).
60. Liang, L. & Meunier, V. First-principles Raman spectra of MoS_2, WS_2 and their heterostructures. *Nanoscale* **6**, 5394–5401 (2014).

ACKNOWLEDGEMENTS

The authors would like to thank Prof. Roman Gorbachev from the University of Manchester and Prof. Jose′ Manuel Caridad from University of Salamanca for their useful input in improving the manuscript. This work is supported by the Austrian Science Fund (FWF) under grants no. I4323-N36 and Y1298-N, and by the Russian Foundation for Basic Research under the project no. 19-52-14006. K.W. and T.T. acknowledge support from the JSPS KAKENHI (Grant Numbers 19H05790, 20H00354 and 21H05233). A.S. and M.K. acknowledge support from the European Regional Development Fund for the "Center of Excellence for Advanced Materials and Sensing Devices" (No. KK.01.1.1.01.0001). Also, the bilateral Croatian-Austrian project funded by Croatian Ministry of Science and Education and the Centre for International Cooperation and Mobility (ICM) of the Austrian Agency for International Cooperation in Education and Research (OeAD-GmbH) under project HR 02/2020 is acknowledged. Further, the bilateral French-Austrian project funded by the Ministère de la Recherche et des Nouvelles Technologies (Amadeus PHC under project no. 42333PL, France) and the Centre for International Cooperation and Mobility (ICM) of the Austrian Agency for International Cooperation in Education and Research (OeAD-GmbH) under project FR 12/2019 is acknowledged.

AUTHOR CONTRIBUTIONS

M.A.A., supervised by A.M., prepared the samples, carried out experiments and data analysis, with exception of NP decoration and related experiments which were carried out by T.H.T. under supervision of E.S. M.A.A. and A.M. prepared the figures. M.A.A, A.M., and R.D.R. wrote the manuscript. T.H.T., E.S., and R.D.R. interpreted the results related to NP decoration. V.M. and E.S. provided interpretations and support for the Raman spectroscopy experiments. K.W. and T.T. provided hBN crystals. O.S. provided DHTA7 molecular source. A.S. and M.A.A. prepared CVD MoS_2 samples under supervision of M.K. C.T., with M.A.A. and A.M. interpreted AFM related data. C.T. assisted in the final MS preparation. A.M. proposed the concept of NRN fabrication and with R.D.R. acquired the main source of funding for the study. All the authors discussed the results and reviewed the manuscript.

COMPETING INTERESTS

The authors declare no competing interests.

ADDITIONAL INFORMATION

Supplementary information The online version contains supplementary material available at https://doi.org/10.1038/s41699-022-00356-y.

Correspondence and requests for materials should be addressed to Muhammad Awais Aslam or Aleksandar Matković.

Reprints and permission information is available at http://www.nature.com/reprints

Publisher's note Springer Nature remains neutral with regard to jurisdictional claims in published maps and institutional affiliations.

Open Access This article is licensed under a Creative Commons Attribution 4.0 International License, which permits use, sharing, adaptation, distribution and reproduction in any medium or format, as long as you give appropriate credit to the original author(s) and the source, provide a link to the Creative Commons license, and indicate if changes were made. The images or other third party material in this article are included in the article's Creative Commons license, unless indicated otherwise in a credit line to the material. If material is not included in the article's Creative Commons license and your intended use is not permitted by statutory regulation or exceeds the permitted use, you will need to obtain permission directly from the copyright holder. To view a copy of this license, visit http://creativecommons.org/licenses/by/4.0/.

© The Author(s) 2022

5.2 The Crucial Role of Collective Water Molecule Dynamics in a Graphene Nanoribbon Switch

M. Awais Aslam, Igor Stankovic, Gennadiy Murastov, Amy Carl, Zehao Song, Kenji Watanabe, Takashi Taniguchi, Alois Lugstein, Christian Teichert, Roman Gorbachev, Raul D. Rodriguez, and Aleksandar Matkovic 2023. The Crucial Role of Collective Water Molecule Dynamics in a Graphene Nanoribbon Switch.

The work presents high-quality graphene nanoribbon (NR) devices which exhibit ferroelectric behavior while utilizing Si/SiO_2 and hBN as substrates. Our results point to the induced ferroelectric effect in oxygen-terminated graphene NR field effect transistors (FET) due to water molecules adsorbed at the NR edges. To observe the orientation of attached water molecules under varying electric field, molecular dynamic (MD) simulations were performed. These simulations are in excellent agreement with the experimental results. Such robust systems can be the basis to fabricate next generation memory devices at the nanoscale.

Status: To be resubmitted to Physical Review Letters journal.

Contribution of the author of the thesis: Prepared all the samples used in the study for electrical and optical characterization and performed all etching procedures. Carried out data analysis and evaluation. Prepared the figures and wrote the manuscript with the support of all co-authors.

The Crucial Role of Collective Water Molecule Dynamics in a Graphene Nanoribbon Switch

Muhammad Awais Aslam[1], Igor Stanković[2,*] Gennadiy Murastov[1], Amy Carl[3], Zehao Song[4], Kenji Watanabe[5], Takashi Taniguchi[6], Alois Lugstein[4], Christian Teichert[1], Roman Gorbachev[3], Raul D. Rodriguez[7], and Aleksandar Matković[1†]

[1] *Chair of Physics, Department Physics, Mechanical Engineering, and Electrical Engineering, Montanuniversität Leoben, Franz Josef Strasse 18, 8700 Leoben, Austria*

[2] *Scientific Computing Laboratory, Center for the Study of Complex Systems, Institute of Physics Belgrade, University of Belgrade, 11080 Belgrade, Serbia*

[3] *Department of Physics and Astronomy and National Graphene Institute, University of Manchester, M13 9PL Manchester, United Kingdom*

[4] *Institute of Solid State Electronics, TU Wien, Gußhausstraße 25-25a, 1040 Vienna, Austria*

[5] *Research Center for Electronic and Optical Materials, National Institute for Materials Science, 1- 1 Namiki, Tsukuba 305-0044, Japan*

[6] *Research Center for Materials Nanoarchitectonics, National Institute for Materials Science, 1-1 Namiki, Tsukuba, 305-0044, Japan and*

[7] *Tomsk Polytechnic University, Lenina ave. 30, 634034, Tomsk, Russia*

(Dated: November 9, 2023)

Abstract: We investigate the role of water in the ferroelectric behavior of networks comprising graphene nanoribbons integrated into field effect transistors. We propose that the collective behavior of water molecules influences the system's dynamics, facilitated by fixed bridging water molecules between the layers and moving clusters formed by surrounding molecules. To gain a deeper understanding, we analyze the dependence of the observed phenomena on various factors, including the number of layers, temperature, and the application of external electric fields. Our experimental findings demonstrate that achieving temperature stability in the ferroelectric effect necessitates a minimum bilayer thickness. The experimental results provide compelling evidence for the presence of the remanent field, in line with the findings obtained from the simulations. This study sheds light on the underlying mechanisms governing the ferroelectric behavior in graphene nanoribbons and offers insights for the design of ferroelectric heterostructures and neuromorphic circuits.

Keywords: Water, Edges, Ferroelectricity, Nanoribbons, Graphene

Despite being at the centre of human life, water molecules and their interaction dynamics with various nanoscaled media remain elusive and fascinating [1, 2]. Understanding of water interaction with low dimensional materials has proven essential for nanofluidics [3], energy storage [4], water splitting [5], purification [6, 7] and water-assisted ferroelectricity [8–10]. In nano-structured materials, water can play a critical role for tuning the properties [11–15] and under ambient conditions its effects are often unavoidable.

In this regard, graphene nanoribbons with a high edge-to-surface ratio presents an excellent platform to study the influence of water behaviour at the edges. Ferroelectric behaviour due to water molecules adsorbed at graphene edges has been first reported in hexagonal boron nitride (hBN) encapsulated, micrometer-size, monolayer graphene devices [9] and subsequently in nanoribbon-based devices [10]. Water induced ferroelectricity in these systems relies on the collective orientation of interacting water molecules and switching between two states as a response to the application of an external electric field. Field-related kinesis of edge-adsorbed water, the influence of graphene thickness on water anchoring, and their interplay on ferroelectricity are not fully uncovered. An understanding of this phenomenon is essential as it warrants the use of water-induced ferroelectricity in radio frequency applications, neuromorphic computing and memcapacitors [16–20].

This study builds-up on the existing knowledge of the water induced ferroelectric effect at graphene edges [9, 10] and brings forward new experimental data with respect to the graphene layer and temperature dependence of this effect, as well as a molecular dynamic model describing the collective behaviour of water at graphene edges. We employ networks of graphene nanoribbons (Gr-NRs) integrated into FETs to demonstrate that at least bilayer thickness is required for a temperature-stable ferroelectric effect. The observed dependence on the number of layers, temperature, and the applied external electric fields is captured by our molecular dynamic (MD) model. We propose that the system exhibits collective behavior of water based on anchoring of the bridging water molecules between the layers. Therefore, the kinesis of the system is strikingly different in mono- and multi-layer nanoribbons.

Figure 1a depicts the schematic of a Gr-NR FET on hBN. See Supporting Information, Methods section

* igor@ipb.ac.rs

† aleksandar.matkovic@unileoben.ac.at

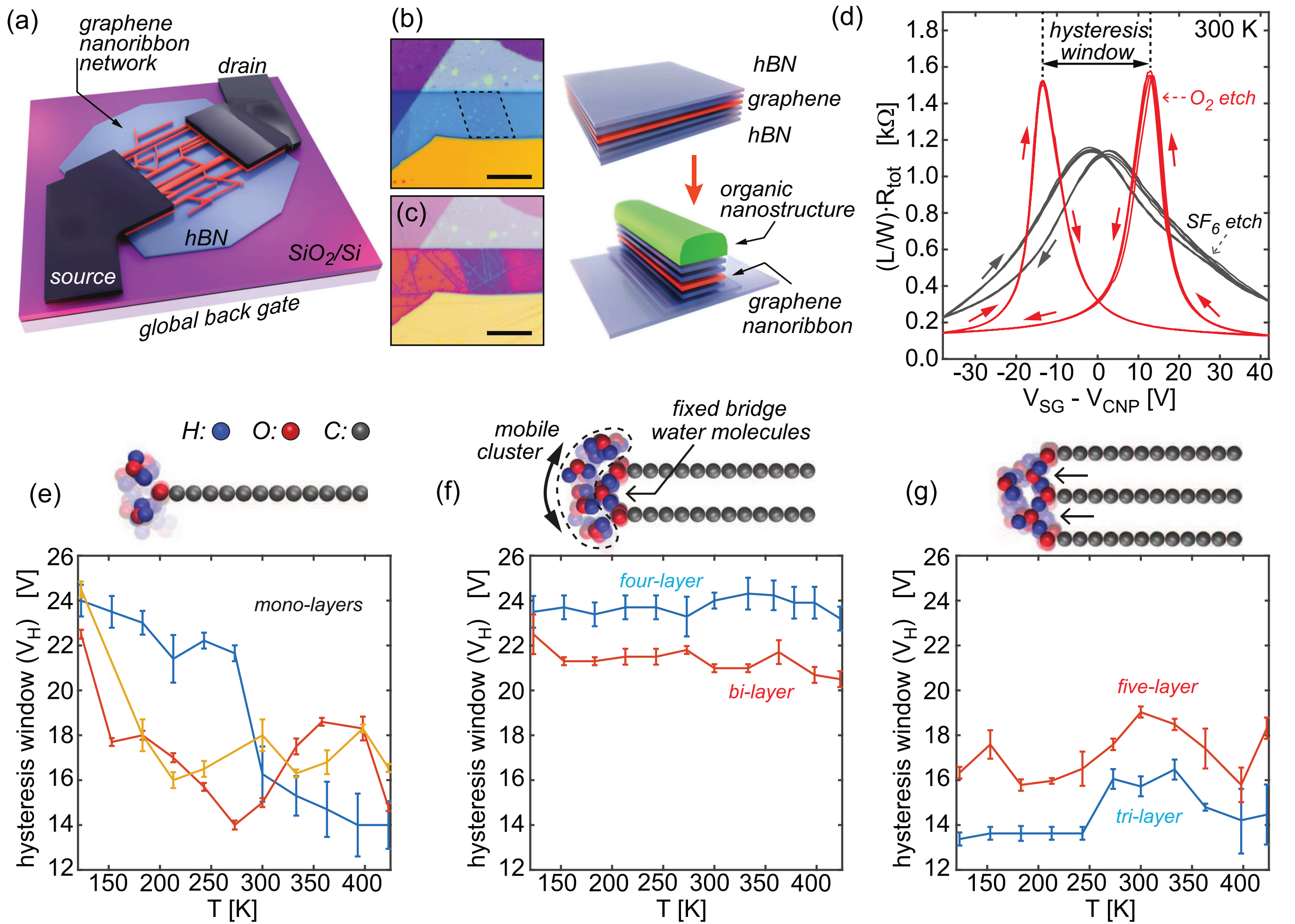

Figure. 1: (a) Schematic representation of nanoribbon filed effect transistor. (b,c) Optical images (scale-bar 10 μm) and corresponding sketches for fabrication of hBN-Gr-hBN nanoribbons. (d) Length and width (L/W) scaled total device resistance (two–terminal) transfer characteristics for 2L Gr-NR-FETs (measured under $2{\cdot}10^{-2}$ mbar). Arrows indicate the sweep direction. V_{SG} range is shifted with respect to the mean V_{CNP} values between both sweeping directions (considering the shifts of 3 V and 28 V for oxygenated and fluorinated ribbons, respectively). (e-g) Temperature dependence of the V_H considering varying thicknesses of graphene NRs. The plot for monolayers includes three different devices colored blue, yellow and orange. Top of (e-g) MD simulation models exhibiting typical local configuration of water clusters in absence of the external electric field.

for more information. Parahexaphenyl (6P) organic nanoneedles self-assembled on hBN-Gr-hBN heterostructures serve as self-aligned masks [10, 21, 22]. Reactive ion etching of the stacks produces a network of Gr nanoribbons (Figure 1b,c). A scheme of the fabrication process is provided in the Supporting Information, Figure S1. The resulting nanoribbons have on average 20 nm width, as estimated from high resolution atomic force microscopy (AFM) images (see also Supporting Information, Figure S2). It is important to mention that the top and bottom encapsulation with hBN is placed to ensure a complete isolation of the graphene nanoribbons from SiO_2 and organic nano-structure interfaces in order to avoid a potential contribution of the charge-traps. Employing hBN as the dielectric separator layers between graphene and potential charge-trap sources ensures that the dominant source of external interaction is originating at the nanoribbon's edges. More detail on the potential charge trap origins are given in the Supporting Information, Figure S3. The choice of precursor gas for plasma controls nanoribbon termination. Using oxygen (O_2) or sulfur hexafluoride (SF_6) allows for oxygen or fluorine terminated edges [9]. Devices with oxygen-terminated edges exhibit pronounced, stable, and switchable (between $p-$ and $n-$doping) characteristics depending on the global back gate (V_{SG}) sweeping direction (Figure 1d). The comparison between the nanoribbon and flake FETs is represented in Supporting Information Figure S4. The difference between two charge neutrality points (CNPs - $R_{tot}(V_{SG})$ maxima) is quantified as

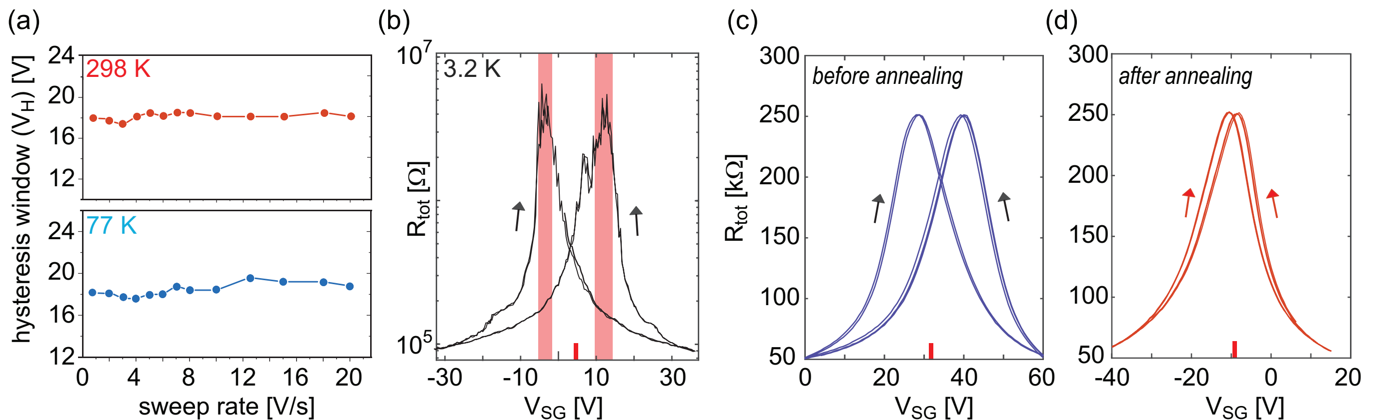

Figure. 2: (a) Change in the V_H with respect to varying V_{SG} sweeping rate (2L device, measured under $2{\cdot}10^{-2}$ mbar). (b) Total device resistance (two–terminal; semi–log curves) transfer curves demonstrating that the hysteresis prevails at 3.2 K with the emergence of transport gap which is highlighted in red color (1L device, measured under $4{\cdot}10^{-6}$ mbar). (c,d) Total device resistance (two–terminal) transfer curves of the same device before and after annealing under vacuum (1L device, measured under $2{\cdot}10^{-2}$ mbar). Red lines next to the x–axis in (b-d) indicate estimates of the unpolarized CNP values.

the hysteresis window (V_H). The relationship between the direction of the applied field and the resulting gate bias where the resistivity maxima occurs (V_{CNP}) have been explained in the Supporting Information Figure S5. The hysteretic behaviour is almost absent in hydrophobic SF_6 etched *i.e.* F-terminated ribbons, as previously observed for graphene flakes [9]. We will discuss oxygen-terminated graphene nanoribbons, which support the adsorption of water molecules and the induced ferroelectricity [9, 23, 24].

The contours of the mechanism behind the hysteretic characteristics shown in Figure 1(d) are known, as Caridad *et.al.* proposed that single molecules switch between the two states [9]. The external gate fields disrupt the equal probability of water arrangements while inducing a torque on the water adsorbed at the edges. The torque is a result of Coulomb forces acting on the water dipole allowing it to cross the energy barrier between the two states *ca.* 25 - 40 meV [9, 25].

The $R_{tot}(V_{\mathrm{SG}})$ hysteresis is thermally stable while at the same time it depends on the number of graphene layers. Figure 1e-g compares monolayer (ML) to thicker Gr-NRs over a temperature range of 120 K - 400 K. For each reported V_H value in Figure 1e-g, V_{SG} sweeping range was fixed between -40 V and +40 V, with a constant sweeping rate of 2 V/s. In monolayer Gr-NR FETs, the width of the hysteresis window decreases as temperature increases. Within the temperature range tested, the hysteresis window remains significant. For the devices with L$\geq$2 (L - number of graphene layers) the ferroelectric effect shows negligible dependence on temperature within the measured range (Figure 1f,g). The temperature characteristics of three- and five-layered graphene show less stable behavior but the hysteresis window does not exhibit a decreasing trend. A mechanism involving a single water molecule crossing the barrier and switching the side of the graphene plane would result in a stronger temperature dependence. When the thermal energy of the molecule is larger than the energy barrier, molecules can thermally switch from one state to the other. Such behaviour was observed in the case of monolayer Gr-NR FETs, with the hysteresis still preserved at elevated temperatures. Further dependence of the hysteresis window on the V_{SG} sweeping range are provided in the Supporting Information, Figure S5.

The direction of the observed hysteresis would indicate that the origin are charge traps in the gate dielectric layer. However, the same direction would result from the edge dipoles (see Supporting Information, Figure S6). To further verify the proposed nature of hysteresis we performed several experiments which can help rule out the influence of extrinsic effects such as impurities and charge traps. As trapping mechanisms can occur on a time scale of seconds [27] we used varying sweep rates (from 0.5 V/sec to 20 V/sec) to observe the effect on V_H. Figure 2a shows a largely unperturbed V_H at both 298 K and 77 K under forward and backward gate sweeps. Similarly, measurements at extremely low temperatures should result in the quenching of any contribution from thermally activated traps [28, 29]. Figure 2b represents the results for a device measured at 3.2 K where it is evident that the hysteresis persists. It is also interesting to note that the resistance exhibits aperiodic fluctuations near the charge neutrality point with high reproducibility indicating the opening of a transport gap. Apart from quantum interference phenomena [30, 31], such insulating states can be attributed to the adsorption of water molecules on the nanoribbon edges. Chen et al. [32] have shown that edge adsorbed water can induce high electric fields which influence the band gap of nanorib-

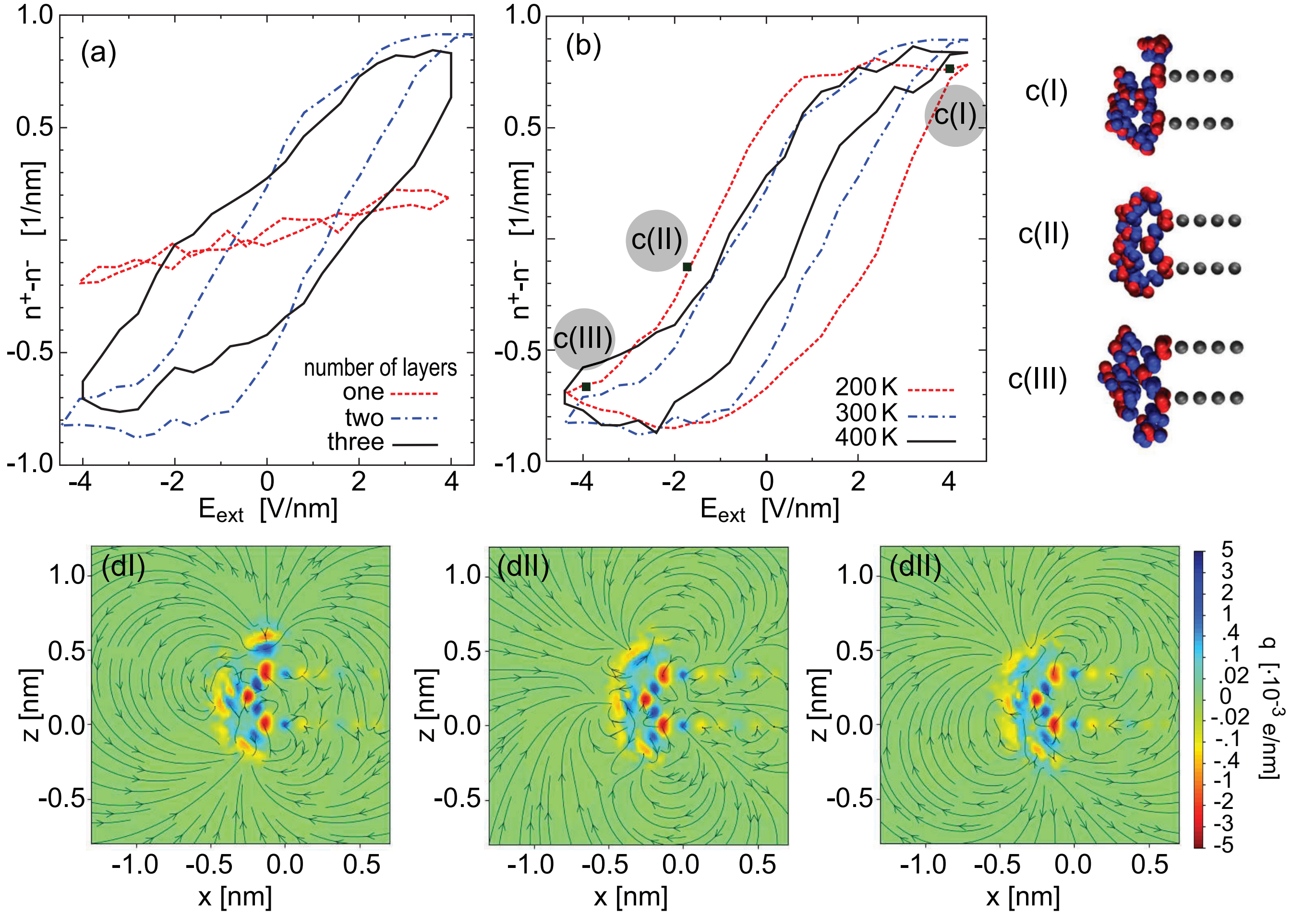

Figure. 3: . (a) Evolution of water molecules "above" n^+ and "below" n^- the graphene planes with varying thicknesses of graphene - for L=1, 2 and 3 layers. The homogeneous electric field is varied cyclically. (b) $n^+ - n^-$ for 2L nanoribbon with varying temperature. (c) The panels (I - III) illustrate induced electric fields E of a graphene ribbon and water molecules at (I) E_{ext} =4 V/nm, (II) E_{ext} =-2 V/nm, and (III) E_{ext} =-4 V/nm. Respective density of charges as well as electric field lines are shown in d(I-III).

bons. Figure 2c,d represent the measurements before and after the annealing without breaking the vacuum. The devices were exposed to high temperatures (573 K) for several hours under $8{\cdot}10^{-3}$ mbar. The diminished V_H can be attributed to the desorption of water molecules from the nanoribbon edges. The hysteresis is restored upon the subsequent air (humidity) exposure. Notable unintentional p–type doping of the device presented in Fig. 2c yields that only the positive V_{SG} values have to be applied, as the gate field has first to compensate for the built–in charge transfer doping induced field, before the total field direction can inverse and introduce the change in the orientation of the water dipoles (see also Supporting Information, Figure S7). In addition, a comparison between the electrical measurements under low vacuum and under ambient conditions (12 % relative humidity) is presented in the Supporting Information, Figure S8.

The tendency of the water molecules to bind at oxygenated edges and form clusters [26] suggests that collective behaviour stabilizes the molecules resulting in a temperature independent effect. To achieve such stable ferroelectric ordering of water molecules on Gr edges, two conditions must be met: (i) a low thermal barrier of a single polar molecule to switch from one state to the other, and (ii) a cluster large enough to stay bound in one state by intermolecular Coulomb interactions. While the first condition is well established, we have designed molecular dynamics simulations to investigate the second condition. The simulations take into account the hydrogen bonds which are implicitly present within the dynamically calculated local charges between water molecules and as well as oxidized graphene edge. Moreover, we also calculate the electric field which is a direct consequence of the molecule's polarization as shown later in the text. Our calculations are in agreement with the model presented in ref. [9], and provide additional information on the collective behaviour of water in this system, and the presence of strongly adsorbed bridging molecules between

graphene layers.

The MD simulations of single-layer graphene confirm the previous prediction of a 25 meV-40 meV energy barrier for the switching of a single water molecule [9, 25]. For the bi-layer system (top of Fig. 1f), the simulations reveal a fundamentally different behaviour of the water molecules. The particular layer separation in graphite allows water molecules to form a "bridge" between the two oxygen-terminated edges. These bridging molecules remain stable and do not react to applied external electric fields. However, they enable the formation of a water cluster around them. Molecular dynamics simulations show that anchored water molecules in the cluster can sustain both high electric fields (5 V/nm) and elevated temperatures up to 500 K. The water cluster that surrounds the bridge molecules is mobile in the electric field, and its collective behaviour stabilizes the structure. As a result, the hysteresis window is essentially temperature-independent. Such collective self-stabilizing behaviour of polar objects was previously observed in colloidal systems and molecular motors [33, 34].

We also performed MD simulations to understand the effect of varying electric fields that act on water molecules. An external homogeneous electric field generated by infinite planes was applied to ML, 2L and 3L graphene NRs. Refer to Supporting Information, Methods section for details about MD simulations. The fraction of polarised molecules above (n^+) and below (n^-) graphene layer quantifies the ferroelectric effect arising from molecular switching. We observed charge bistability and switching between two states under cyclical change of the external field (Figure 3a). It is important to note, that in the experiment the electric field source was generated between the ribbon and the flat surface (gate electrode), while in simulations the electro–neutral system with the ribbon and water molecules was placed between two uniformly charged planar electrodes generating a homogeneous field. Further, in the simulations, the electric field applied was over an order of magnitude higher than in the experiment when considering a parallel capacitance model. This was done to reduce simulation time, since electric field strength exponentially prolongs the switching time of the model system. In the experiments, field enhancement is expected due to the fringing capacitance effects [9]. An estimate of the enhancement and the field profiles based on a finite elements model of the device structure is provided in the Supporting Information, Figure S9. We anticipate about one order of magnitude enhancement of the out–of–plane field component due to the fringing capacitance effects, reaching up to 2 V/nm within the experimentally achievable biasing range.

For a monolayer ribbon, the fraction of molecules ($n^+ - n^-$) is proportional to the external electric field, suggesting a low energy barrier between the states. This can be attributed to the absence of a bridging water molecule compared to systems with L $\geq$ 2. Our experiments on monolayer graphene nanoribbons showed a temperature-dependent hysteresis. This observed discrepancy between the model and the experimentally probed monolayer systems may be attributed to a more complex interfaces available experimentally, involving hBN and potentially residuals of the organic masks. Additionally, the model system has much shorter temporal evolution (4 ns) to the external electrostatic perturbation than the timescale of the experiments (over 100 ms).

For L $\geq$ 2, a prominent evolution of the hysteresis was noted in the MD simulations (Figure 3a). Such an evolution of the system with electric field depends on the initial state. The field lines and field strength acting on a 2L nanoribbon generated via MD simulations are represented in Supporting information Figure S10. As the electric field decreases, some of the molecules remain stationary until the field polarization switches, causing these molecules to migrate to the other side with respect to the nanoribbon's basal plane. It should be noted that the hysteresis is weakly dependent on the temperature as shown in Figure 3b for L = 2. Such stability indicates that the switching of polarization in the model is in a qualitative agreement with the experiments, as increased thermal energy (400 K) does not result in disorder that could change the ferroelectric nature of the system. At low temperatures (200 K) the coercivity is overestimated in our simulations since switching time is extended due to the lower mobility of water molecules.

Figure 3d (I-III) represents snapshots of the edge segments for a 2L Gr-NR system with the corresponding charge distribution and induced electric filed lines. The system consists of both externally applied fields (not shown) and induced fields with opposite polarities in **z** direction. Figure 3c and 3d(I) presents the case of saturation with an external field of 4.1 V/nm applied in **z** direction. An induced charge redistribution is observed due to the molecular polarisation at the edges, which in turn creates an effective electric dipole moment. This changes the local field over the whole graphene double-layer profile. The effective electric field is, therefore, a sum of the two fields and as the external field decreases, they could cancel each other in parts of the graphene plane. Figure 3c - 3d(II) displays the configuration where the induced electric dipole points roughly along graphene, *i.e.* representing one of the coercivity points of the out of plane dipole field hysteresis. Consequently, the induced electric field component perpendicular to the ribbon will be negligible. Finally, for -4.1 V/nm we observe a complete reversal of the induced electric field. As the field strength increases, the migration and molecular polarisation repeat in the opposite order, generating a hysteresis loop (Figure 3b). The bonding between the polar molecular ensemble and the graphene edge, together with the intermolecular Coulomb interactions should be strong enough to prevent the external electric field from tearing off molecules from the cluster. The details on the large-scale atomistic model are presented in Supporting Information Figure S11. Our MD simulations show that under external fields exceeding ~5 V/nm, individual

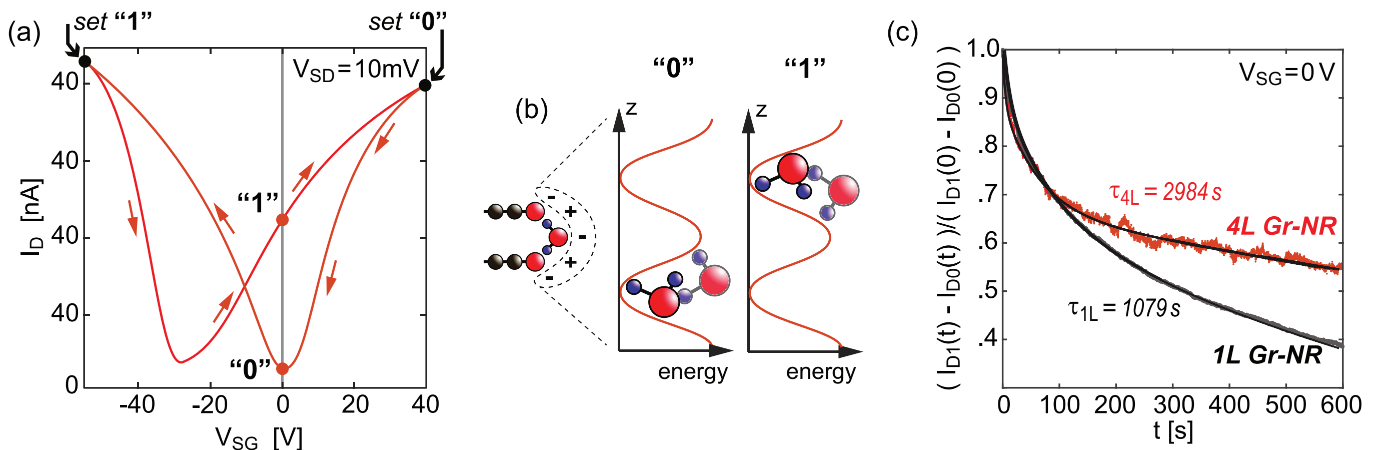

Figure. 4: (a) The hysteresis curve for 1L Gr-NR FET after the application of a bias stress (measured under $2{\cdot}10^{-2}$ mbar; unpolarized position of the CNP $\sim$2 V). (b) The schematic representation of retention states for the water clusters adsorbed at the edges. (c) The source-drain current deviation in time with respect to the ML (τ = (1041 $\pm$ 315) s) vs 4L (τ = (3020 $\pm$ 125) s) graphene nanoribbon devices (measured under $2{\cdot}10^{-2}$ mbar).

molecules dissociate from the edges at 300 K.

To confirm the pronounced hysteresis predicted by the MD simulation, we tracked the evolution of the drain current (I_D) of Gr NR FETs without an external gate field, after pre-biasing the devices into the n^+ or the n^- states. Figure 4a presents a hysteretic transfer curve of the water terminated Gr-NR-FET, where the range of the gate voltages was chosen so that one of the charge neutrality points is at V_{SG} = 0 V [35]. Supporting Information Figure S12 compares symmetrical and asymmetrical V_{SG} sweeps. This way the difference in I_D for the n^+ and the n^- states is maximized. The two $I_D(V_{SG}$ = 0 V) states can be defined as "0" and "1", corresponding to low or the CNP state and the high current state (see Figure 4b).

By sweeping from V_{SG} = 0 V to one end of the range, and returning back to V_{SG} = 0 V, the system is set either to the I_D "0" or "1" state. From this point on, the I_D is recorded as a function of time without an externally applied gate field. In both cases of mono- and multi-layer nanoribbons, the dipole induced remanent field was observed. The results comparing a ML and a 4L Gr NR FET are shown in Figure 4c, where the normalized difference between $I_{D1}(t)$ and $I_{D0}(t)$ was tracked for 600 s at 300 K and under low vacuum. To characterize the decay of the field, the curves were fitted to $C{\cdot}exp(-t/\tau)$; where C stands for a scaling constant and τ for time constant.

The remanence of the field for a ML is less pronounced and the current difference between the two states decays faster than in the multi-layer Gr NR FETs (Figure 4c). The time constants indicate that the ML NR-based devices lose 90 % of the initial I_D difference between the "0" and "1" states in about 30 min, and 4L NR-based devices in about 90 min. Further, a faster decaying component (τ = (64 $\pm$ 32) s) responsible for about 15-20 % of the I_D difference was noticed in all devices, and attributed to weakly bound molecules. Gr-NR-FETs with L $\geq$ 2, require several hours of storage to have the initial transfer curve sweep starting from the depolarized state of the water molecules, which is consistent with the extracted time constants.

We observed a different trend in the temperature dependency of the hysteresis window for monolayer than for L $\geq$ 2 nanoribbons. In multi–layered NRs the ferroelectric response is weakly temperature dependent, which indicates a collective and self-stabilizing effect. This behaviour requires a water cluster large enough so that collectively molecules can stay bound in one state by intermolecular Coulomb interactions. The simulations revealed a different behaviour of the system for mono- and multi-layer NRs. For L $\geq$ 2, the two adjacent layers enabled the adsorption of a "bridge" water molecule, that together with the oxygen-terminated edges promotes the formation of a water cluster. Our model predicts collective behavior of the cluster and bi-stability in the external electric fields, resulting in hysteresis of the induced dipole fields acting on the Gr-NRs. Robust, temperature independent, and high remanent fields in graphene nanoribbon networks could be utilized in the heterostacks with other 2D materials, creating new device concept based on molecular switching for applications such as computing in memory, and synaptic circuits.

References:

[1] Interfacial Liquid Water on Graphite, Graphene, and 2D Materials R. Garcia, *ACS Nano* **2023**, 17(1) , 51–69.

[2] The hydrogen bond and the water molecule: The physics and chemistry of water, aqueous and bio-media Yves Maréchal, *Elsevier* **2007**, I - X.

[3] Enhanced nanofluidic transport in activated carbon nanoconduits HT. Emmerich, K.S. Vasu, A. Niguès, A. Keerthi, B. Radha, A. Siria, and L. Bocquet *Nature Materials* **2022**, 21(6),696-702.

[4] Synthesis of two dimensional materials for capacitive energy storage B. Mendoza Sanchez, and Y. Gogotsi, *Advanced Materials* **2016**, 28(29), 6104-6135.

[5] Wien effect in interfacial water dissociation through proton-permeable graphene electrodes J. Cai, E.Griffin, V.H. Guarochico-Moreira, D. Barry, B. Xin, M. Yagmurcukardes, S. Zhang, A.K. Geim, F.M. Peeters and M. Lozada-Hidalgo *Nature Communications* **2022**, 13(1), 5776.

[6] 2D nanostructures for water purification: graphene and beyond S. Dervin, D.D. Dionysiou and S.C. Pillai, *Nanoscale* **2016**, 8(33), 15115-15131.

[7] Water desalination using nanoporous single-layer graphene S.P. Surwade, S.N. Smirnov, I.V. Vlassiouk, R.R. Unocic, G.M. Veith, S. Dai and S.M. Mahurin, *Nature Nanotechnology* **2015**, 10(5), 459-464.

[8] Ferroelectric 2D ice under graphene confinement H.T. Chin, J. Klimes, I.F. Hu, D.R. Chen, H.T. Nguyen, T.W. Chen, S.W. Ma, M. Hofmann, C.T. Liang, and Y.P. Hsieh *Nature Communications* **2021**, 12(1), 6291.

[9] A graphene-edge ferroelectric molecular switch J.M. Caridad, G. Calogero, P. Pedrinazzi, J.E. Santos, A. Impellizzeri, T. Gunst, T.J. Booth, R. Sordan, P. Bøggild, and M. Brandbyge, *Nano Letters* **2018**, 18(8), 4675-4683.

[10] Single-crystalline nanoribbon network field effect transistors from arbitrary two-dimensional materials M.A. Aslam, T.H. Tran, A. Supina, O. Siri, V. Meunier, K. Watanabe, T. Taniguchi, M. Kralj, C. Teichert, E. Sheremet, R.D. Rodriguez and A. Matkovic *npj 2D Materials and Applications* **2022**, 6(1), 76.

[11] Potential barrier of graphene edges W. Wang and Z. Li *Journal of Applied Physics* **2011**, 109(11), 114308.

[12] The impact of edges and dopants on the work function of graphene nanostructures: The way to high electronic emission from pure carbon medium D.G. Kvashnin, P.B. Sorokin, J.W. Brüning, and L.A. Chernozatonskii *Applied Physics Letters* **2013**, 102(18), 183112.

[13] Study of water adsorption on graphene edges L. Jiang, J. Wang, P. Liu, W. Song, and B. He *Royal Society of Chemistry Advances* **2018**, 8(20), 11216-11221.

[14] Atomically precise edge chlorination of nanographenes and its application in graphene nanoribbons Y.Z. Tan, B. Yang, K. Parvez, A. Narita, S. Osella, D. Beljonne, X. Feng, and K. Müllen, *Nature Communications* **2013**, 4(1), 2646.

[15] Band gap engineering via edge-functionalization of graphene nanoribbons P. Wagner, C.P. Ewels, J.J. Adjizian, L. Magaud, P. Pochet, S. Roche, A. Lopez-Bezanilla, V.V. Ivanovskaya, A. Yaya, M. Rayson, and P. Briddon, *Journal of Physical Chemistry C* **2013**, 117(50), 26790-26796.

[16] Ferroelectric memory based on nanostructures X. Liu, Y. Liu, W. Chen, J. Li, L. Liao, *Nanoscale Research Letters* **2012**, 7, 285.

[17] Two-dimensional materials for next-generation computing technologies C. Liu, H. Chen, S. Wang, Q. Liu, Y. G Jiang , D. W. Zhang, , M. Liu, P. Zhou, *Nature Nanotechnology* **2020**, 15(7), 545-557.

[18] Recent progress in two-dimensional ferroelectric materials Z. Guan, H. Hu, X. Shen,, P. Xiang, N. Zhong, J. Chu, C. Duan, *Advanced Electronic Materials* **2020**, 6(1), 1900818.

[19] Enhanced bulk photovoltaic effect in two-dimensional ferroelectric $CuInP_2S_6$ Y. Li, J. Fu, X. Mao, C. Chen, H. Liu, M. Gong, H. Zeng, *Nature Communications* **2021**, 12(1), 5896.

[20] Ionic memcapacitive effects in nanopores M. Krems, Y.V. Pershin, M. Di Ventra, *Nano Letters* **2010**, 10(7), 2674-2678.

[21] Light-Assisted Charge Propagation in Networks of Organic Semiconductor Crystallites on Hexagonal Boron Nitride A. Matković, J. Genser, M. Kratzer, D. Lüftner, Z. Chen, O. Siri, P. Puschnig, C. Becker, and C. Teichert, *Advanced Functional Materials* **2019**, 29(43), 1903816, 1-10.

[22] Effects of polymethylmethacrylate-transfer residues on the growth of organic semiconductor molecules on chemical vapor deposited graphene M. Kratzer, B.C. Bayer, P.R. Kidambi, A. Matković, R. Gajić, A. Cabrero-Vilatela, R.S. Weatherup, S. Hofmann, and C. Teichert, *Applied Physics Letters* **2015**, 106(10), 103101.

[23] Doping graphene by adsorption of polar molecules at the oxidized zigzag edges, J. Berashevich, T. Chakraborty, *Physical Review B* **2010**, 81(20), 205431.

[24] Adsorption capacity of H2O, NH3, CO, and NO2 on the pristine graphene, X. Lin, J. Ni, C. Fang, *Jounal of Applied Physics* **2013**, 113(3), 034306.

[25] Water molecules in a carbon nanotube under an applied electric field at various temperatures and pressures, E. Yamamoto, K. Yasuoka, *Water* **2017**, 9(7), 473.

[26] The collective burst mechanism of angular jumps in liquid water, A. Offei-Danso, U.N. Morzan, A. Rodriguez, A. Hassanali, and A. Jelic, *Nature Communications* **2023**, 14(1), 1345.

[27] Hysteresis of electronic transport in graphene transistors H. Wang, Y. Wu, C. Cong, J. Shang, and T. Yu, *ACS Nano* **2010**, 4(12), 7221-7228.

[28] Reversible control of doping in graphene-on-SiO_2 by cooling under gate-voltage. A.K. Singh, and A.K. Gupta, *Journal of Applied Physics* **2017**, 122(19), 195305.

[29] Thermally activated trap charges responsible for hysteresis in multilayer MoS_2 field-effect transistors Y. Park, H.W. Baac, J. Heo, and G. Yoo, *Applied Physics Letters* **2016**, 108(8), 083102.

[30] Gate-induced insulating state in bilayer graphene devices J.B. Oostinga, H.B. Heersche, X. Liu, A.F. Morpurgo, and L.M. Vandersypen, *Nature Materials* **2008**, 7(2), 151-157.

[31] Interaction-induced insulating state in thick multilayer graphene Y. Nam, D.K. Ki, M. Koshino, E. McCann, and A.F. Morpurgo, *2D Materials* **2016**, 3(4), 045014.

[32] Water Induced Bandgap Engineering in Nanoribbons of Hexagonal Boron Nitride C. Chen, et al. *Advanced Materials* **2023**, 35, 2303198.

[33] Collective dynamics of dipolar and multipolar colloids: From pas-

sive to active systems, S. HL Klapp, *Current Opinion in Colloid and Interface Science* **2016**, 21, 76-85.

[34] Cooperative cargo transport by several molecular motors, S. Klumpp, R. Lipowsky *Proceedings of National Academy of Sciences* **2005**, 102(48), 17284-17289.

[35] Control of Water Adsorption via Electrically Doped Graphene: Effect of Fermi Level on Uptake and H2O Orientation, M.H. Bagheri, R.T. Loibl, and S.N. Schiffres, *Advanced Materials Interfaces* **2021**, 8(18), 2100445.

Acknowledgements

This work is supported by the Austrian Science Fund (FWF) under grants no. I4323-N36 and Y1298-N, and by the Russian foundation for basic research under the project no. 19-52-14006. A.M. acknowledges the support from ERC Starting grant POL_2D_PHYSICS (101075821). I.S. acknowledges the support of the Ministry of Education, Science, and Technological Development of the Republic of Serbia through the Institute of Physics Belgrade and the European Commission through the ULTIMATE-I project partner Senzor Infiz doo, grant ID 101007825. Molecular dynamics calculations were run on the PARADOX super-computing facility at the Scientific Computing Laboratory, Center for the Study of Complex Systems of the Institute of Physics Belgrade. K.W. and T.T. acknowledge support from the JSPS KAKENHI (Grant Numbers 20H00354 and 23H02052) and World Premier International Research Center Initiative (WPI), MEXT, Japan. R.G. acknowledges support from Royal Society, ERC Consolidator grant QTWIST (101001515) and EPSRC grant numbers EP/V007033/1, EP/S030719/1 and EP/V026496/1. A.C. acknowledges support from EPSRC CDT Graphene NOWNANO, grant EP/L01548X/1. Views and opinions expressed are however those of the authors only and do not necessarily reflect those of the European Unionor the European Research Council Executive Agency; neither the European Union nor the granting authority can be held responsible for them.

Author Contributions

MAA prepared the samples, carried out experiments and data analysis under the supervision of AM. IS performed the simulations. GM performed the measurements for the field remanence. MAA wrote the manuscript with the help of IS and AM. MAA and ZS carried out etching experiments under the supervision of AL. KW and TT provided hexagonal boron nitride crystals. RG and AC provided monolayer graphene on hexagonal boron nitride. RDR and CT helped in the internal review of the manuscript. AM and RDR acquired the main funding for the study. All the authors discussed the results and reviewed the manuscript.

Additional information

Supporting Information: Additional experimental details, materials, and methods.

Competing financial interests: The authors declare no competing financial interests.

5.3 All van-der-Waals semiconducting $PtSe_2$ field effect transistors with low contact resistance

M. Awais Aslam, Shubham Tyagi, Alexandros Provia, Vadym Tkachuk, Egon Pavlica, Kenji Watanabe, Takashi Taniguchi, Dayu Yan, Youguo Shi, Theresia Knobloch, Michael Waltl, Udo Schwingenschloegl, Tibor Grasser, and Aleksandar Matkovic 2023. All van der Waals semiconducting $PtSe_2$ field effect transistors with low contact resistance.

The work presents semiconducting $PtSe_2$ field effect transistors with all-van-der-Waals electrode and dielectric interfaces. Graphite contacts are used which enable high I_{on}/I_{off} ratios up to 10^9, mobilities as high as 500 cm^2 V^{-1} s^{-1} and currents above 100 μA. Moreover, top and bottom hBN encapsulation is used to reduce the charge scattering induced by defects. The devices exhibit exceptional stable behaviour over multiple sweep cycles. The contact resistance at the graphite-$PtSe_2$ interface is determined by *in-operando* Kelvin probe force microscopy yielding very low values of 0.36 kΩ-cm. The results present $PtSe_2$ as a promising candidate for realization of high performance 2D circuits.

Status: Under review in ACS Nano Letters.

Contribution of the author of the thesis: Prepared all the samples used in the study for electrical, optical and as well as AFM/KPFM measurements. Characterized the samples via optical spectroscopy, AFM/KPFM and electrical measurements. Carried out data analysis and evaluation. Prepared the figures and wrote the manuscript with the support of all co-authors.

All van der Waals semiconducting $PtSe_2$ field effect transistors with low contact resistance graphite electrodes

M. Awais Aslam[1], Shubham Tyagi[2], Alexandros Provias[3], Vadym Tkachuk[4], Egon Pavlica[4], Kenji Watanabe[5], Takashi Taniguchi[6], Dayu Yan[7], Youguo Shi[7], Theresia Knobloch[3], Michael Waltl[8], Udo Schwingenschlögl[2], Tibor Grasser[3], and Aleksandar Matković[1]*

[1] *Department Physics, Mechanical Engineering, and Electrical Engineering, Montanuniversität Leoben, Franz Josef Strasse 18, 8700 Leoben, Austria*
[2] *Physical Science and Engineering Division (PSE), King Abdullah University of Science and Technology (KAUST), Thuwal, Saudi Arabia*
[3] *Institute for Microelectronics, TU Wien, Gußhausstraße 27-29/E360, 1040 Wien, Austria*
[4] *Laboratory of Organic Matter Physics, University of Nova Gorica, Vipavska 13, Nova Gorica SI-5000, Slovenia*
[5] *Research Center for Electronic and Optical Materials, National Institute for Materials Science, 1-1 Namiki, Tsukuba 305-0044, Japan*
[6] *Research Center for Materials Nanoarchitectonics, National Institute for Materials Science, 1-1 Namiki, Tsukuba 305-0044, Japan*
[7] *Beijing National Laboratory for Condensed Matter Physics and Institute of Physics, Chinese Academy of Sciences, 100190, Beijing, China and*
[8] *Christian Doppler Laboratory for Single-Defect Spectroscopy at the Institute for Microelectronics, TU Wien, Gußhausstraße 27-29/E360, 1040 Wien, Austria*

(Dated: February 13, 2024)

Contact resistance is a multifaceted challenge faced by the 2D materials community. Large Schottky barrier heights and gap-state pinning are active obstacles which require an integrated approach to achieve the development of high–performance electronic devices based on 2D materials. In this work, we present semiconducting $PtSe_2$ field effect transistors with all–van–der–Waals electrode and dielectric interfaces. We use graphite contacts which enable high I_{ON}/I_{OFF} ratios up to 10^9 with the currents above $100\,\mu A\,\mu m^{-1}$, mobilities of $50\,cm^2V^{-1}s^{-1}$ at room temperature, and over $400\,cm^2V^{-1}s^{-1}$ at 10 K. The devices exhibit high stability with an effective oxide thickness scaled maximum hysteresis width below $36\,mV\,nm^{-1}$. The contact resistance at the graphite–$PtSe_2$ interface is determined by *in–operando* Kelvin probe force microscopy yielding low values of $680\,\Omega\,\mu m$. Our results present $PtSe_2$ as a promising candidate for the realization of high performance 2D circuits built solely with 2D materials.

Since the end of the Dennard scaling era [1], the semiconductor industry has struggled to keep up with the ever growing demands of nanoelectronics. Although, new architectures [2, 3] and changes in gate dielectric materials [4, 5] have helped scaling down of very large scale microelectronics, there is an immediate need to replace the channel material. This is due to the performance limits of silicon technology below 4 nm channel thickness [6]. In this regard, the International Road map for Devices and Systems (IRDS) 2022 lists two-dimensional (2D) materials as probable candidates for standard complementary metal–oxide semiconductor (CMOS) technology in the coming years [7]. 2D materials not only offer sub–nanometer thicknesses but also provide a wide range of opportunities for neuromorphic computing [8, 9], photonic integrated circuits [10, 11] and quantum technologies [12, 13]. Therefore, intensive efforts have been made in the last decade to make 2D material–based very large–scale integration (VLSI) technology a reality [14, 15].

However, high contact resistances [16, 17] and growth temperatures [15, 18] are the foremost challenges preventing the co-integration of 2D materials into CMOS technologies. High contact resistances effectively reduces the bias applied along the channel, consequently also reducing the drain current and causing high power dissipation at the junctions [19]. Contact engineering methods [20–23] and doping techniques [24, 25] have helped approach the quantum limits of contact resistance for various monolayer transition metal dichalcogenides (TMDCs). Yet, their integration is limited by the high growth temperatures which are not compatible with the back end of line (BEoL) processes [14, 18].

Among various 2D materials which can be grown at BEoL–friendly temperatures ($T < 450°C$), platinum diselenide ($PtSe_2$) has garnered substantial research interest [26–29]. This is due to its predicted high performance owing to unique 6–fold degenerate valleys in the conduction band, while maintaining excellent air stability [26, 27]. $PtSe_2$ is also predicted to exhibit drift carrier mobilities up to $3000\,cm^2\,V^{-1}s^{-1}$), which are much higher than those of most other TMDCs [28]. Although $PtSe_2$ is inherently a semi–metal, it transitions to a semiconductor at reduced thicknesses (<6 nm; *i.e.* <10 layers), making it ideal for the integration into field effect transistors [27, 29].

Many studies have been done to show high currents in thicker layers (8–11 nm) of metallic $PtSe_2$. However, for effective field modulation, channel thicknesses below

* aleksandar.matkovic@unileoben.ac.at

4 nm are required. Notably, Das *et al.* demonstrated on state currents (I_{ON}) of up to 0.6 µA µm^{-1} for a channel thickness of 1.5 nm while utilising thick $PtSe_2$ itself as a contact material [27]. Intrinsically, $PtSe_2$ can provide a large density of states near the conduction band minima, while a small effective mass ensures high drift mobilities [28, 30]. However, high performance few layered (up to 4 nm) $PtSe_2$ field effect transistors (FET) have not been reported yet. This can be attributed to the high contact resistances in $PtSe_2$ devices. Deposition of metals for contacting the 2D materials results in the formation of mid gap states (metal induced gap states and defect induced gap states) near the conduction band as a result of metal inter–diffusion or defect formation at the interface [21, 31]. These result in the gap–state pinning and in high injection barriers for both electrons and holes. To realise the true potential of $PtSe_2$, it is important to have contacts that avoid mid gap–states and help approach the Schottky–Mott limit with minimal contact resistance. For this, studies based on first–principles methods have shown formation of an ohmic contact between $PtSe_2$ and graphite under the influence of external electric fields [32, 33].

In this study, we report few–layer (FL) graphite contacts (10–30 nm) to $PtSe_2$ as a channel material (thicknesses $\leq$4 nm). These FETs exhibit very low contact resistances of 680 Ω µm, and consequently result in high performance transport characteristics. We show hysteresis free transfer curves with I_{ON}/I_{OFF} ratios of 10^9 at 10 K and above 10^4 at room temperature. To benefit from an atomically flat gate dielectric interface, we have employed hexagonal boron nitride (hBN), effectively making our system pure van der Waals based. Record–low values for contact resistance are verified via *in–operando* Kelvin Probe Force Microscopy (KPFM), and supported by low–temperature electrical output and transfer characteristics.

Results and discussions

Electrical characteristics for FL graphite contacted $PtSe_2$

Figure 1a shows the schematic representation of the device and the optical micrograph with graphite contacts as source and drain. Hexagonal boron nitride (hBN) (15 nm) was used as a gate dielectric (see Methods for more information related to device fabrication). The thicknesses of the exfoliated $PtSe_2$ flakes were verified by the ratios of A_{1g} / E_g Raman active modes (see Supplementary Information Figure S1) [28, 34]. Figures 1b and c represent the electrical transfer characteristics (drain current versus gate voltage) for a 2 nm $PtSe_2$ flake at 298 K and 77 K. An ambipolar behaviour is evident with I_{ON}/I_{OFF} ratios for the electron branch of ∼10^3 at room temperature (298 K). Currents scaled by the device width (W) for the electron branch I_D go up to 2 µA µm^{-1} for a small V_D of 125 mV. This is an order of magnitude better than the best reported values for similar thicknesses [28]. At 298 K, the off state - the current minimum in the transfer characteristics - is affected by the thermal broadening of the valence/conduction band edges [28, 35]. This effect becomes more evident for thicker $PtSe_2$ devices, due to the diminishing band gap with increasing thicknesses, as $PtSe_2$ transforms from a semiconductor to a semi–metal. Furthermore, potential contaminants that can deposit on the device active area during fabrication also contribute to an increase in the off state current. These can be minimized by vacuum annealing of the devices, as shown in Supplementary Information Figure S2. The devices exhibit excellent stability for a large number of operation cycles (×50) (forward and backward sweeps), as detailed later in the text.

The contribution to the I_{OFF} from the thermally excited carriers is significantly reduced at 77 K (Figure 1c). At lower temperatures, the off state is stable and independent of V_D. Moreover, the devices showed a very small variation of the threshold voltage V_{th} with a sigma of 50 mV (considering 15 nm hBN as a gate dielectric). An increase of the on state I_D was observed for the electron branch at 77 K compared to 298 K, indicating a low contact barrier. Moreover, I_D reaches up to 30 µA µm^{-1} at a low V_D of 1 V with an I_{ON}/I_{OFF} ratio of 10^6. Such superior on state characteristics have been theoretically predicted for $PtSe_2$ due to the large density of states, especially in comparison to other TMDCs [26]. On the contrary, the hole current does not increase at 77 K. This indicates a blocking contact to the hole branch, and is explained later in more detail. Nevertheless, we recorded I_D of up to 1.5 µA µm^{-1} for the hole branch at 77 K with an I_{ON}/I_{OFF} ratio of over 10^4. The inset in Figure 1c represents the calculated sheet conductivity (σ_{2D}) for the electron branch as a function of temperature. An exponential increase in electron conductivity is noted with a decrease of the temperature, indicating a highly conductive on state of $PtSe_2$ [28].

To verify the nature of contact to the electron and hole branches we plotted the output curves (I_D vs V_D) as shown in Figure 1d. Electron transport reveals a linear behaviour, especially at very low V_D (shown in the inset), indicating a good ohmic contact. On the other hand, for hole transport we observe a non–linear change in I_D. These results point to a Fermi level alignment close to the conduction band edge of $PtSe_2$, which primarily results in efficient electron injection.

Gate bias dependent apparent linear electron mobility plots for varying temperatures are shown in Figure 1e. An increase in the apparent electron mobility was observed when the temperature is lowered from 298 K to 10 K, as phonon scattering mechanisms reduce with temperature [36]. The apparent hole mobilities were observed to experience a similar trend in the temperature dependence with about five times lower values, which also supports electron dominant transport in graphite contacted $PtSe_2$.

An increase of current density and mobility was also observed with increasing thickness of $PtSe_2$ (Figure 2a

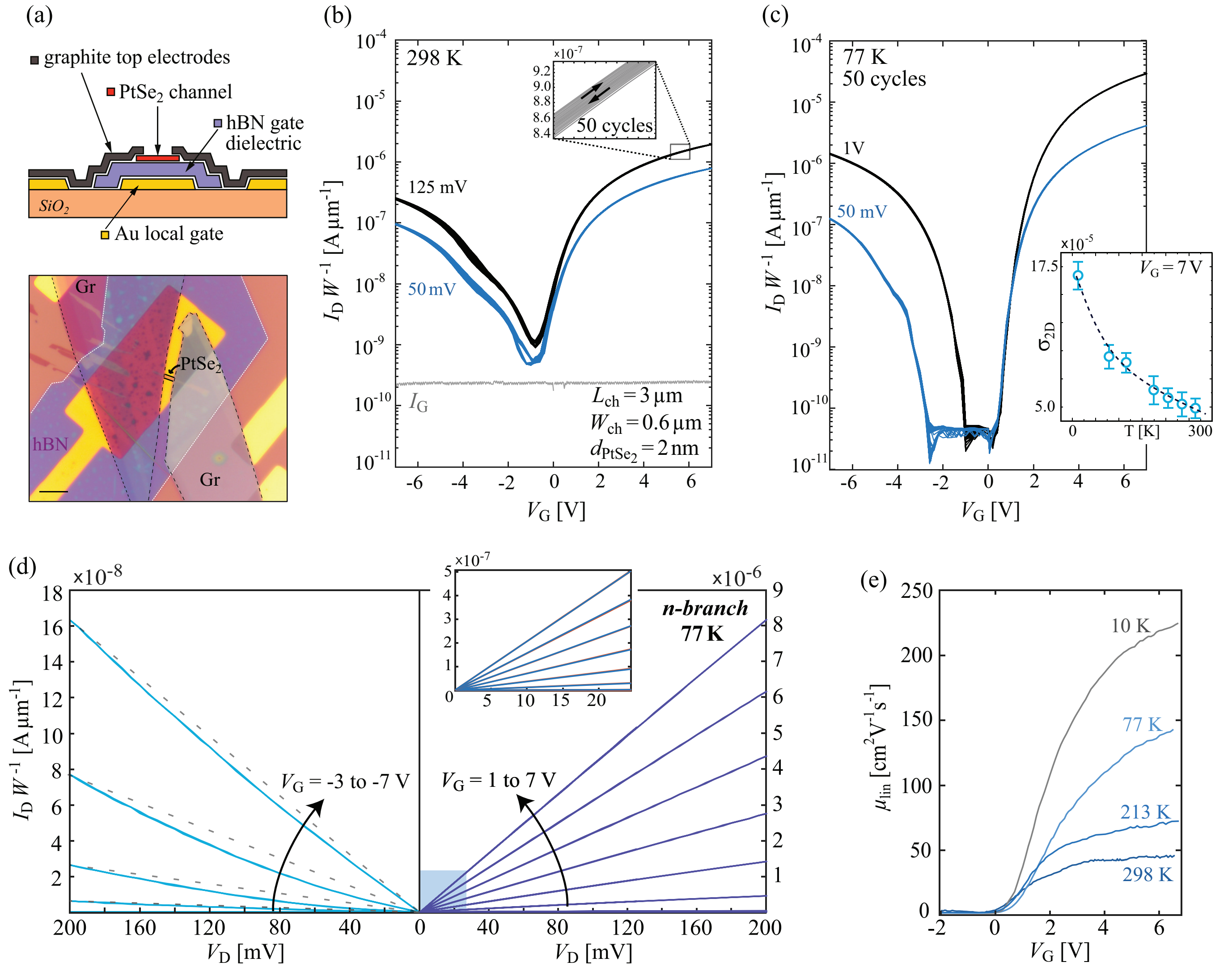

Figure. 1: **Electrical characteristics of graphite contacted $PtSe_2$ FETs:** (a) Schematic representation of device configuration with optical image of $PtSe_2$ FET (scale-bar: 10 µm) (b-c) Transfer curves of a 2 nm thick $PtSe_2$ flake at 298 K and 77 K (semi–log scale), overlaying 50 subsequent forward and backward sweeps (see inset of (b)). (b) also presents the level of the gate leakage current (I_G) with a solid gray line. Inset in (c) shows electron conductivity plot with decreasing temperature, dashed line presents an exponential fit. (d) Output curves for the hole and electron branches at 77 K. The inset shows the region of lower V_D bias to highlight the linearity of the electron–branch. (e) Apparent linear electron mobilities for 2 nm $PtSe_2$ as a function of V_G at the different temperatures.

and b). The transport curves at room and low temperature for various thicknesses are presented in Supplementary Information Figure S3, which show I_{ON}/I_{OFF} ratios of up to 10^9 at 10 K. Our results also validate the study by Zhao *et al.* as they associated the decrease of mobility at low temperatures to remote charge scattering and increased roughness induced by the SiO_2 substrate [28]. Whereas, in our case hBN provides cleaner and atomically flat interface to $PtSe_2$, reducing the charge scattering [37, 38]. To verify the stability of the devices we carried out systematic frequency sweeps at room temperature to observe the change in the hysteresis width (V_H) [39, 40]. Figure 2c shows the hysteresis width (V_H) normalized to the effective oxide thickness (EOT) plotted against the reciprocal sweep time $t_{sw}{}^{-1}$. A maximum hysteresis of 36 mV nm^{-1} was recorded for a 1.5 nm thick device with 18 nm thick hBN as back gate on top of Au electrode. It is pertinent to note that although the device was not capped from the top, very low V_H were observed. The hysteresis is expected to be further reduced with a top capping [40, 41]. On the other hand devices based on 290 nm SiO_2 gate dielectric with ∼10 nm hBN interface to $PtSe_2$ showed larger hysteresis with a maximum V_H of 280 mV nm^{-1}, see supplementary information Figure S4.

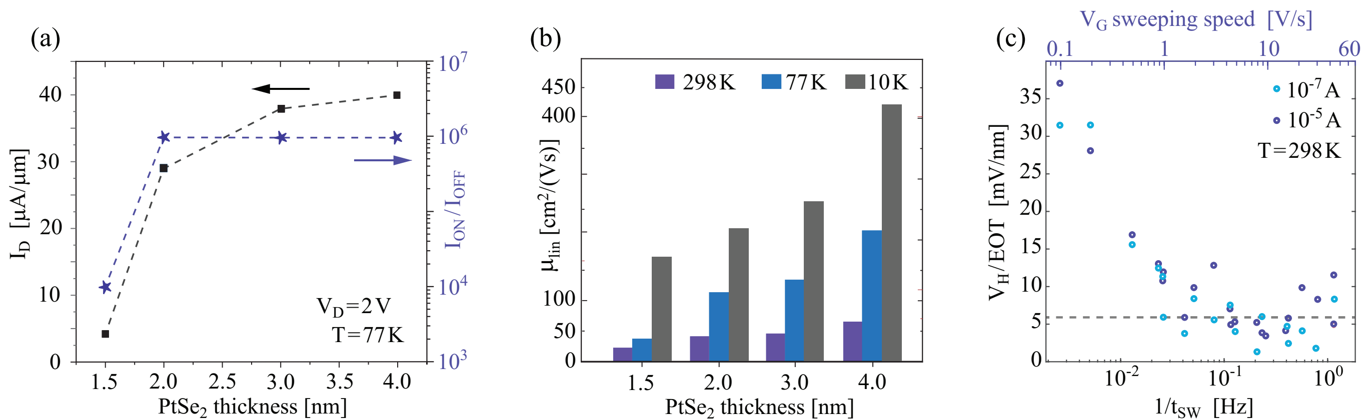

Figure. 2: **$PtSe_2$ thickness dependent transport characteristics and device stability** (a) Maximum width–scaled current ratios I_{ON}/I_{OFF} achieved for the devices ($V_D = 2\,V$). (b) Apparent linear electron mobility with respect to the thickness at various temperatures. (c) Stability of the forward and backward V_G sweeping induced hysteresis of the electron branch as a function of the sweeping frequency (${t_{sw}}^{-1}$), presented in a semi–log frequency scale. The purple and the blue data points in (c) indicate the current values at which V_H was extracted.

Contact Resistance via in-operando KPFM

Kelvin Probe Force Microscopy (KPFM) has emerged as a powerful approach to image the potential distribution along the FET channel during operation [42–45]. It provides a direct measure for the source and drain contact resistances independently of each other, by tracking the contact potential difference voltage (V_{CPD}) profiles across the device active area. For our devices, the *in–operando* measurements were done in a frequency modulation regime (FM-KPFM). Figure 3a represents the topography image of a 2.3 nm thick $PtSe_2$ channel fabricated on top of hBN. Black lines indicate the electrical connections in a KPFM configuration (see methods for more details) allowing the modulation of V_D and V_G during V_{CPD} measurements. To estimate the work function (WF) difference between graphite and $PtSe_2$ we performed repeated single line scans with all electrodes grounded, as shown in Figure 3b. The measurements of the graphite electrodes serve also as a reference [46] for estimating the absolute values of the $PtSe_2$ WF. As the area of $PtSe_2$ away from the contact and the top surface of the graphite electrode are imaged, the measurements essentially provide the WF difference values away from the interface. A higher WF of $PtSe_2$ (by 70 meV) implies an electron transfer from the graphite electrodes to $PtSe_2$ at the interface. The charge redistribution introduces a downward bending of the $PtSe_2$ bands at the interface to graphite, and therefore a preferred n–type ohmic contact at the junction. The band alignment is illustrated in Figure 3c and shows the diagram before and after interface formation (equal vacuum and Fermi levels respectively). As the valence band minimum is further away from the Fermi level of few layer graphite, holes experience a higher injection barrier, whereas it is easier for the electrons to move into the conduction band.

To further understand the energy level alignments of the graphite contacts to the $PtSe_2$ FETs we have calculated the energy band diagrams for a Gr-$PtSe_2$-hBN heterostructure using density functional theory (DFT) within the generalized gradient approximation of Perdew–Burke–Ernzerhof for the exchange–correlation functional. Six–layered graphite was used in combination with two–layers of $PtSe_2$ and two-layered hBN to mimic the experimental conditions. The results are provided in Supplementary Information Figures S5 and S6.

Figure 3d shows the potential drop across the channel (corrected for WF difference [45]) while the device is biased with $V_D = 250\,mV$. The top of Figure 3d represents the corresponding height cross–section. A linear decrease in the potential is seen from the drain to source contact with a small kink at the source electrode which points to the electron injection barrier. The majority of the applied V_D (86 %) is utilized for the transport across the channel which in turn results in highly efficient field modulation and high apparent linear mobility. When correlated with the recorded I_D during the KPFM measurements and scaled with the device width, we can express the junction–related potential drop as contact resistance, yielding the value of $(680 \pm 40)\,\Omega\,\mu m$. The potential drops across the channel were recorded for various values of V_D (varied from 50 mV to 250 mV with 50 mV steps). The data set allows to extract the non–linear I_D dependence of the contact resistance. The results are presented in Figure 3e. The width scaled contact resistance is fitted by a combination of ohmic and diode component (solid line in Figure 3e) [45]. In the probed I_D range, only minor increase of the contact resistance is observed with the reducing I_D. This indicates a predominant bias–independent ohmic contribution to the contact resistance.

A comparison of our results to the literature reported values of the contact resistance between $PtSe_2$ and various contact materials is provided in Figure 3f, consid-

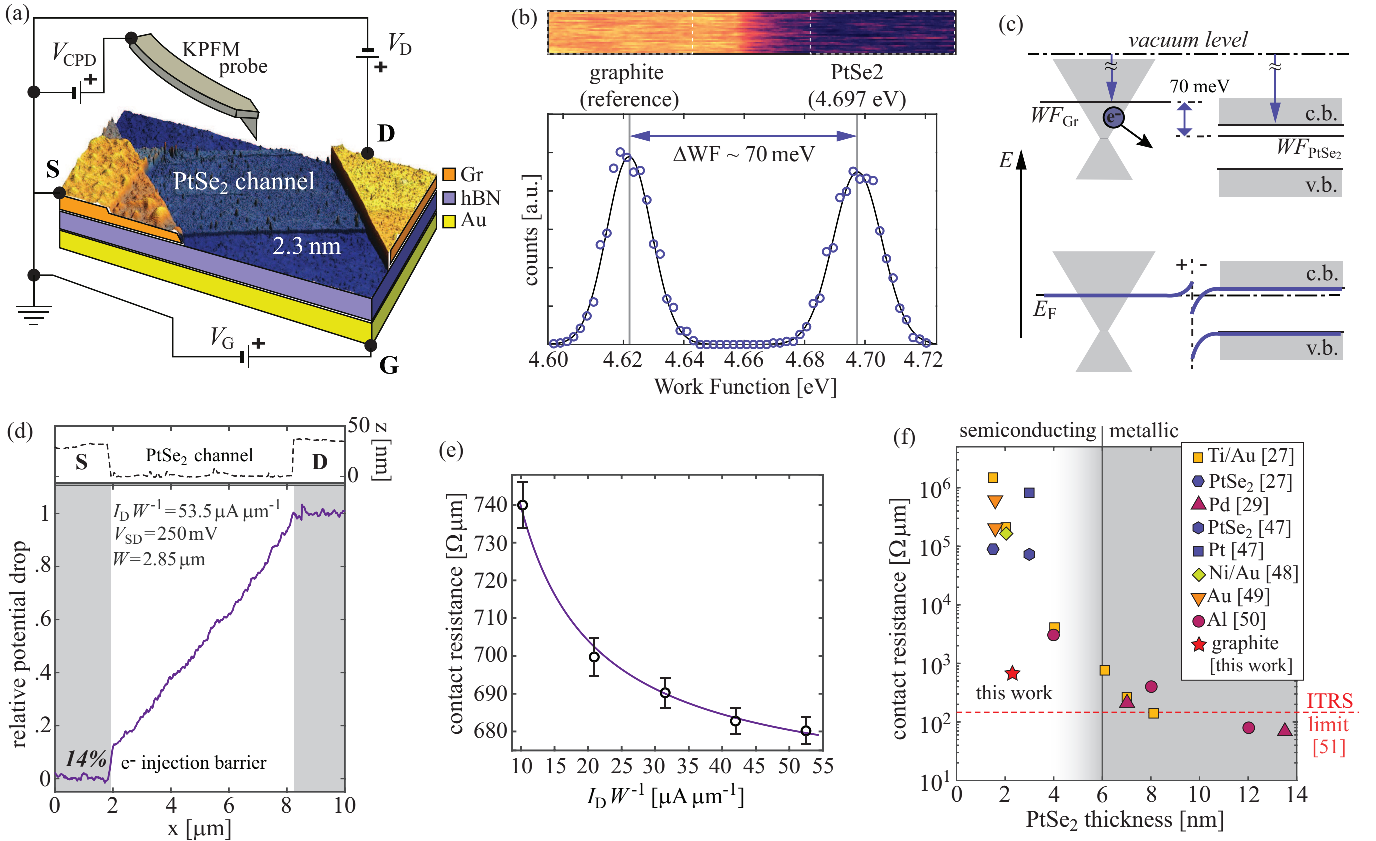

Figure. 3: **Work Function (WF) differences, band alignment, and electric potential profiles:** (a) 3D topography map of the $PtSe_2$ channel superimposed to the schematic representation of the KPFM setup (not to scale) with electrical connections. (b–top) WF difference between graphite and $PtSe_2$, presenting the contact potential difference map scanning across the graphite/$PtSe_2$ edge (top). Darker V_{CPD} for the $PtSe_2$ region is a consequence of the higher work function with respect to graphite. (b–bottom) Histogram of the regions from the map indicated with dashed white lines in the CPD map. The difference of the work function between $PtSe_2$ and graphite was estimated from the peak–to–peak difference of the Gaussian fits to the histogram (solid lines). (c) Band diagram for the graphite–$PtSe_2$ system before and after the formation of the interface (with equal vacuum and Fermi levels, respectively). (d) *in–operando* KPFM recorded normalized potential drop across the channel, showing also the corresponding height profile. (e) Extracted contact resistance as function of the width–scaled drain current. The fit (solid line) presents the model combining a Schottky and Ohmic component of the contact resistance. (f) comparison of the reported contact resistance value (star) with the literature [27,29,47–50]. The dashed horizontal line in (f) indicates the 2024 ITRS limit for the contact resistance [51].

ering evaporated metallic contacts as Ti/Au [27], Ni/Au [48], Au [49], Pd [29], Pt [47], Al [50], and vdW contacts with metallic $PtSe_2$ [27, 47]. The reported values are correlated to the $PtSe_2$ thickness, indicating also a rough limit between metallic and semiconducting transition at ∼6 nm. In addition the, International Technology Roadmap for Semiconductors (ITRS) set target, for the year 2024, for the contact resistance (146 Ω μm) is indicated by a dashed horizontal line [30, 51]. While the values obtained for graphite/$PtSe_2$ contacts are still above the technology threshold, these are almost two order of magnitude lower values in comparison to the reported contact resistance in the similar $PtSe_2$ thickness range.

This record–low contact resistance can be attributed to the pristine van der Waals interface between $PtSe_2$ and graphite. This enables atomically sharp transition between the two materials and essentially forbids Fermi level pinning. Such interface is in contrast to conventional evaporated electrodes where the metal induced gap states and as well as defect induced gap states deteriorate the contact properties and increase the carrier injection barrier [21, 52]. Graphite electrodes are expected to form a similar low contact resistance junction even with the thicker $PtSe_2$ devices due to a minor change in the work function of $PtSe_2$ with respect to the change in number of layers; an increase of approximately 10 meV for the increase in thickness from 2 nm to 5 nm [53–55].

Conclusions

Our study demonstrates that graphite is as an excellent electrode material for contacting $PtSe_2$, a 2D semiconductor which can be grown at BEoL friendly temperatures (below 450°C). The graphite/$PtSe_2$ interface is particulary efficient for electron injection and accessing the conduction band of $PtSe_2$ for the field modulated transport. Our KPFM measurements reveal a record–low contact resistance of 680 Ω µm between $PtSe_2$ and graphite electrodes. These are some of the best contact properties to 2D semiconductors, and the values are very close to the ITRS 2024 limit of 146 Ω µm [51], especially in comparison to other contact interfaces to $PtSe_2$ below 4 nm thickness [27, 47–50].

As the devices do not suffer from high electron injection barriers, we have obtained high current densities, high I_{ON}/I_{OFF} ratios, and the apparent electron mobilities of up to 450 $cm^2\,V^{-1}\,s^{-1}$ at 10 K, and 50 $cm^2V^{-1}s^{-1}$ at room temperature. Integration of hBN provides an atomically smooth gate dielectric interface, with low density of interfacial traps. Consequently, our devices display negligible hysteresis during a large number of voltage sweeps. An effective oxide thickness scaled maximum hysteresis width below ∼36 $mV\,nm^{-1}$ was observed, which quenches to below 6 $mV\,nm^{-1}$ at sweeping speeds above 10 $V\,s^{-1}$.

Methods

$PtSe_2$ crystal growth

$PtSe_2$ single crystals were grown by using Cu-Se fluxes. High-purity Pt, Se and Cu elements were placed in an alumina crucible with molar ratio of 1:8:8 in glove box. Then the alumina crucible was sealed inside a tantalum ampule under argon atmosphere. After that, the tantalum ampule was sealed in an evacuated quartz tube. The quartz tube is heated to 600℃ over 10 hours with a 20–hour dwell time. The temperature was then increased to 1050℃ and held for 10 hours before slowly cooling the tube down to 900℃ at a rate of 1℃ per hour. Finally, the crystals were separated from the flux through centrifugation, yielding millimeter sized single crystals at the bottom of the crucible.

2D materials, organic masks, and device fabrication

Flakes of 2D materials were mechanically exfoliated from bulk crystal and transferred onto 300 nm SiO_2/Si substrate using commercially available Nitto tape and polydimethylsiloxane (Gel-Pak-DLG-X4). Thin flakes were identified via optical contrast, AFM and Raman measurements. 50 nm/5 nm thick Au/Cr electrodes were prepared using laser lithography (DaLi) and thermal evaporation. Their shape resembled to five parallel strips. A pair of strips on each side was used for bias/current sensing/sourcing to graphite electrodes, which capped the pair of electrodes. The middle Au strip was used as the bottom gate and was covered with a hBN.

Electrical characterization Electrical characterization for room temperature and 77 K were done using Keithley 2636A Source-Meter attached to the Instec probe station. The samples were contacted with Au coated Ti electrical cantilever microprobes. The temperatures were monitored via mK2000 temperature controller connected to the probe station with a temperature resolution of 0.01 K. Low temperature (less than 77 K) electrical measurements were performed in a cryogenic (Lake Shore) probe station also employing Keithley 2636A Source-Meter.

AFM and FM-KPFM measurements AFM and FM-KPFM measurements were performed using an Horiba/AIST-NT Omegascope AFM system. Nunano SPARK 350 Pt probes were used with a spring constant of 42 Nm^{-1}, resonant frequency 350 kHz, and tip radius of 30 nm. FM-KPFM measurements were carried out in a two-pass mode, with the probe lifted by 15 nm in the second pass. Topography and CPD images were processed in the open-source software Gwyddion v2.56.

Raman spectroscopy Raman measurements were performed using a Horiba LabRam HR Evolution confocal Raman spectrometer using 1800 lines/mm gratings. A 532 nm laser source was used to excite the samples with an excitation power of 0.1–3.2 mW. The laser spot was focused by a 100x, 0.9 NA objective.

DFT calculations Structural optimization and calculation of the electronic properties are performed using density functional theory within the generalized gradient approximation of Perdew-Burke-Ernzerhof for the exchange-correlation functional, as implemented in the Vienna ab-initio simulation package [56]. The total energy convergence threshold is set to 10^{-6} eV and all structures are optimized until the Hellmann–Feynman forces stay below 0.005 eV/Å. We use a energy cutoff of 520 eV for the plane wave expansion. The first Brillouin zones of the two-layered $PtSe_2$, graphene, and six-layered graphite are sampled on $15 \times 15 \times 1$ k-meshes, while a $9 \times 9 \times 1$ k-mesh is used for the heterostructure model. Periodic boundary conditions are used with 20 Å vacuum slabs to create two-dimensional models. The spin-orbit coupling is not taken into account after checking that it has minor effects on the electronic properties.

---

[1] 2D materials for future heterogeneous electronics. M.C. Lemme, D. Akinwande, C. Huyghebaert, and C. Stampfer *Nat. Commun.*

2022, 13(1), p.1392

[2] Considerations for ultimate CMOS scaling. K.J. Kuhn *IEEE T-ED* **2012**, 59(7), pp.1813-1828.

[3] FinFET versus gate-all-around nanowire FET: performance, scaling, and variability. D. Nagy, G. Indalecio, A.J. Garcia-Loureiro, M.A. Elmessary, K. Kalna, and N. Seoane, *IEEE Journal of the Electron Devices Society* **2018**, 6, pp.332-340.

[4] Nano-CMOS gate dielectric engineering. H. Wong, *Crc Press* **2011**, 32, 45.

[5] A 45nm Logic technology with high-k+metal gate transistors, strained silicon, 9 Cu interconnect layers, 193nm dry patterning, and 100 percent Pb-free packaging. K. Mistry, et al. *In 2007 IEEE International Electron Devices Meeting* **2007**, 247–250.

[6] Graphene and two-dimensional materials for silicon technology. D. Akinwande, C. Huyghebaert, C.H. Wang, M.I. Serna, S. Goossens, L.J. Li, H.S.P. Wong, and F.H. Koppens, *Nature* **2019**, 573(7775), pp.507-518.

[7] More than Moore. *IEEE* **2022**, IRDS More Moore, Technical Report Piscataway, NJ, USA.

[8] Ultrafast machine vision with 2D material neural network image sensors. L. Mennel, J. Symonowicz, S. Wachter, D.K. Polyushkin, A.J. Molina-Mendoza, and T. Mueller *Nature* **2020**, 579(7797), pp.62-66.

[9] Logic-in-memory based on an atomically thin semiconductor. G. Migliato Marega, Y. Zhao, A. Avsar, Z. Wang, M. Tripathi, A. Radenovic, and A. Kis *Nature* **2020**, 587(7832), pp.72-77.

[10] 2D materials enabled next generation integrated optoelectronics: from fabrication to applications. Z. Cheng, R. Cao, K. Wei, Y. Yao, X. Liu, J. Kang, J. Dong, Z. Shi, H. Zhang, and X. Zhang, *Advanced Science* **2021**, 8(11), p.2003834.

[11] Graphene-based integrated photonics for next-generation datacom and telecom. M. Romagnoli, V. Sorianello, M. Midrio, F.H. Koppens, C. Huyghebaert, D. Neumaier, P. Galli, W. Templ, A. D'Errico, and A.C. Ferrari, *Nature Reviews Materials* **2018**, 3(10), pp.392-414.

[12] Recent advances in quantum effects of 2D materials. Y. Yi, Z. Chen, X.F. Yu, Z.K. Zhou, and J. Li, *Advanced Quantum Technologies* **2019**, 2(5-6), p.1800111.

[13] Nanomaterials for quantum information science and engineering. A. Alfieri, S.B. Anantharaman, H. Zhang, and D. Jariwala, *Advanced Materials* **2022**, p.2109621.

[14] The development of integrated circuits based on two-dimensional materials. K. Zhu, C. Wen, A.A. Aljarb, F. Xue, X. Xu, V. Tung, X. Zhang, H.N. Alshareef, and M. Lanza, *Nature Electronics* **2021**, 4(11), pp.775-785.

[15] Transistors based on two-dimensional materials for future integrated circuits. S. Das, A. Sebastian, E. Pop, C.J. McClellan, A.D. Franklin, T. Grasser, T. Knobloch, Y. Illarionov, A.V. Penumatcha, J. Appenzeller, and Z. Chen *Nature Electronics* **2021**, 4(11), pp.786-799.

[16] Electrical contacts to two-dimensional semiconductors. A. Allain, J. Kang, K. Banerjee, and A. Kis, *Nature materials* **2015**, 14(12), pp.1195-1205.

[17] More than Moore M. Chhowalla, D. Jena, and H. Zhang *Nature Reviews Materials* **2016**, 1(11), pp.1-15.

[18] Challenges for Nanoscale CMOS Logic Based on Two-Dimensional Materials. T. Knobloch, S. Selberherr, and T. Grasser, *Nanomaterials* **2022**, 1(11), 12(20), p.3548..

[19] High electric field carrier transport and power dissipation in multilayer black phosphorus field effect transistor with dielectric engineering. F. Ahmed, Y.D. Kim, M.S. Choi, X. Liu, D. Qu, Z. Yang, J. Hu, I.P. Herman, J. Hone, and W.J. Yoo, *Advanced Functional Materials* **2017**, 27(4), p.1604025.

[20] Approaching the quantum limit in two-dimensional semiconductor contacts. W. Li et al. *Nature* **2023**, 613(7943), pp.274-279.

[21] Ultralow contact resistance between semimetal and monolayer semiconductors. P.C. Shen, et al. *Nature* **2021**, 593(7858), pp.211-217.

[22] Approaching the Schottky–Mott limit in van der Waals metal–semiconductor junctions. Y. Liu, J. Guo, E. Zhu, L. Liao, S.J. Lee, M. Ding, I. Shakir, V. Gambin, Y. Huang, and X. Duan, *Nature* **2018**, 557(7707), pp.696-700.

[23] All van-der-Waals Barrier-Free Contacts for High-Mobility Transistors. X. Zhang, H. Yu, W. Tang, X. Wei, L. Gao, M. Hong, Q. Liao, Z. Kang, Z. Zhang, and Y. Zhang, *Advanced Materials* **2022**, 34(34), p.2109521

[24] Highly stable and tunable chemical doping of multilayer WS_2 field effect transistor: Reduction in contact resistance. H.M. Khalil, M.F. Khan, J. Eom, and H. Noh, *ACS applied materials and interfaces* **2015**, 7(42), pp.23589-23596.

[25] Tuning electrical conductance of MoS_2 monolayers through substitutional doping. H. Gao, J. Suh, M.C. Cao, A.Y. Joe, F. Mujid, K.H. Lee, S. Xie, P. Poddar, J.U. Lee, K. Kang, and P. Kim *Nano Letters* **2020**, 32, 45.

[26] $PtSe_2$ field-effect transistors: New opportunities for electronic devices. A. AlMutairi, D. Yin, and Y. Yoon, *IEEE Electron Device Letters* **2017**, 39(1), pp.151-154.

[27] Doping-free all $PtSe_2$ transistor via thickness-modulated phase transition. T. Das, E. Yang, J.E. Seo, J.H. Kim, E. Park, M. Kim, D. Seo, J.Y. Kwak, and J. Chang, *ACS Applied Materials and Interfaces* **2021**, 13(1), pp.1861-1871

[28] High electron mobility and air stable 2D layered $PtSe_2$ FETs. Y. Zhao, J. Qiao, Z. Yu, P. Yu, K. Xu, S.P. Lau, W. Zhou, Z. Liu, X. Wang, W. Ji, and Y. Chai, *Advanced Materials* **2017**, 29(5), p.1604230.

[29] Thickness-modulated metal-to-semiconductor transformation in a transition metal dichalcogenide. A. Ciarrocchi, A. Avsar, D. Ovchinnikov, and A. Kis, *Nature communications* **2018**, 9(1), p.919.

[30] Intrinsic limit of contact resistance in the lateral heterostructure of metallic and semiconducting $PtSe_2$. E. Yang, J.E. Seo, D. Seo, and J. Chang, *Nanoscale* **2020**, 12(27), pp.14636-14641.

[31] Interaction-and defect-free van der Waals contacts between metals and two-dimensional semiconductors. G. Kwon, Y.H. Choi, H. Lee, H.S. Kim, J. Jeong, K. Jeong, M. Baik, H. Kwon, J. Ahn, E. Lee, and M.H. Cho, *Nature Electronics* **2022**, 5(4), pp.241-247

[32] Electronic properties of graphene–$PtSe_2$contacts. S. Sattar and U. Schwingenschlogl, *ACS Applied Materials and Interfaces* **2017**, 9(18), pp.15809-15813.

[33] $PtSe_2$/graphene hetero-multilayer: gate-tunable Schottky barrier height and contact type. C. Xia, J. Du, L. Fang, X. Li, X. Zhao, X. Song, T. Wang, and J. Li, *Nanotechnology* **2018**, 29(46), p.465707.

[34] Large-area high quality $PtSe_2$ thin film with versatile polarity. W. Jiang, X. Wang, Y. Chen, G. Wu, K. Ba, N. Xuan, Y. Sun, P. Gong, J. Bao, H. Shen and T. Lin, *InfoMat* **2019**, 1(2), pp.260-267.

[35] Physics of semiconductor devices. S.M. Sze, Y. Li, and K.K. Ng, *John wiley and sons* **2021**, p.5.

[36] Black phosphorus field-effect transistors. L. Li, Y. Yu, G.J. Ye, Q. Ge, X. Ou, H. Wu, D. Feng, X.H. Chen, and Y. Zhang, *Nature nanotechnology,* **2014**, 39(5), pp.372-377

[37] The performance limits of hexagonal boron nitride as an insulator for scaled CMOS devices based on two-dimensional materials. T. Knobloch, et al. *Nature Electronics* **2021**, 34(2), pp.98-108.

[38] Charge scattering and mobility in atomically thin semiconductors. N. Ma and D.Jena, *Physical Review X* **2014**, 4(1), p.011043.

[39] Energetic mapping of oxide traps in MoS_2 field-effect transistors

Y.Y. Illarionov, T. Knobloch, M. Waltl, G. Rzepa, A. Pospischil, D.K. Polyushkin, M.M. Furchi, T. Mueller, and T. Grasser, *2D Materials* **2017**, 4(2), p.025108.

[40] Improved hysteresis and reliability of MoS_2 transistors with high-quality CVD growth and Al_2O_3 encapsulation Y.Y. Illarionov, K.K. Smithe, M. Waltl, T. Knobloch, E. Pop, and T. Grasser, *IEEE Electron Device Letters* **2017**, 38(12), pp.1763-1766

[41] Reliability of scalable MoS_2 FETs with 2 nm crystalline CaF_2 insulators Y.Y. Illarionov, A.G. Banshchikov, D.K. Polyushkin, S. Wachter, T. Knobloch, M. Thesberg, M.I. Vexler, M. Waltl, M. Lanza, N.S. Sokolov, T. Mueller and T. Grasser *2D Materials* **2019**, 6(4), p.045004.

[42] Surface potential profiling and contact resistance measurements on operating pentacene thin-film transistors by Kelvin probe force microscopy. K.P. Puntambekar, P.V. Pesavento, and C.D. Frisbie, *Applied Physics Letters* **2003**, 83(26), pp.5539-5541.

[43] Single-crystalline nanoribbon network field effect transistors from arbitrary two-dimensional materials. M.A. Aslam, et al, *npj 2D Materials and Applications,* **2022**, 6(1), p.76.

[44] Tuning the graphene work function by electric field effect. Y.J. Yu, Y. Zhao, S. Ryu, L.E. Brus, K.S. Kim, and P. Kim, *Nano letters* **2009**, 9(10), pp.3430-3434.

[45] Interfacial band engineering of MoS2/gold interfaces using pyrimidine-containing self-assembled monolayers: toward contact-resistance-free bottom-contacts. A. Matkovic, et al, *Advanced electronic materials* **2020**, 6(5), p.2000110.

[46] Twisted graphene in graphite: Impact on surface potential and chemical stability. T.H. Tran, R.D. Rodriguez, M. Salerno, A. Matković, C. Teichert, and E. Sheremet, *Carbon* **2021**, 176, pp.431-439.

[47] Barrier-free semimetallic PtSe2 contact formation in two-dimensional PtSe2/PtSe2 homostructure for high-performance field-effect transistors. Y.-H. Kim, M.-S. Kang, J.W. Choi, W. Jae, W.-Y. Lee, M.-J. Kim, N.-W. Park, Y.-G. Yoon, G.-S. Kim, and S.-K. Lee, *Applied Surface Science* **2023**, 638, 158061.

[48] High-performance hybrid electronic devices from layered $PtSe_2$ films grown at low temperature. C. Yim, et al, *ACS Nano* **2016**, 10(10), 9550–9558.

[49] Controlled doping of wafer-scale $PtSe_2$ films for device application. H. Xu, et al, *Advanced Functional Materials* **2019**, 29(4), 1805614.

[50] Wafer-scale fabrication of recessed-channel PtSe 2 MOSFETs with low contact resistance and improved gate control. L. Li, et al, *IEEE Transactions on Electron Devices* **2018**, 64(10), 4102–4108.

[51] International Technology Roadmap for Semiconuctors (ITRS) [Online]. Available: http://www.itrs.net/).

[52] Making clean electrical contacts on 2D transition metal dichalcogenides. Y. Wang and M. Chhowalla, *Nature Reviews Physics* **2022**, 4(2), pp.101-112.

[53] Structural, electronic and phononic properties of $PtSe_2$: from monolayer to bulk. A. Kandemir, B. Akbali, Z. Kahraman, S.V. Badalov, M. Ozcan, F. İyikanat, and H. Sahin, *Semiconductor Science and Technology* **2018**, 33(8), p.085002.

[54] 2D semimetal with ultrahigh work function for sub-0.1 V threshold voltage operation of metal-semiconductor field-effect transistors. T. Zhang et al. *Materials and Design* **2023**, p.112035.

[55] Highly Reliable Electrochemical Metallization Threshold Switch Through Conductive Filament Engineering Using Two-Dimensional $PtSe_2$ Insertion Layer. M.S. Kim, E. Park, S.G. Kim, J.H. Park, S.H. Kim, K.H. Han, and H.Y. Yu, *Advanced Materials Interfaces* **2023**, 10(7), p.2202296.

[56] From ultrasoft pseudopotentials to the projector augmented wave method. G. Kresse, and D. Joubert, *Physical Review B* **1999**, 59(3), pp.1758-1775.

Acknowledgements: This work is supported by the Austrian Science Fund (FWF) under grants no. I4323-N36 and Y1298-N. AM acknowledges the support from ERC Starting grant POL_2D_PHYSICS (101075821). EP and VT acknowledge the financial support by the Slovenian Research Agency under research program P1-0055. The authors acknowledge infrastructure support of the Montanuniversitaet Leoben (Raman AFM TERS lab). US and ST acknowledge the support from King Abdullah University of Science and Technology (KAUST). YS and DY acknowledge the funding from the National Natural Science Foundation of China (U2032204) and the Strategic Priority Research Program (B) of the Chinese Academy of Sciences (No. XDB33000000). KW and TT acknowledge support from the JSPS KAKENHI (Grant Numbers 20H00354 and 23H02052) and World Premier International Research Center Initiative (WPI), MEXT, Japan.

Author Contributions MAA and AM conceived the idea and coordinated the study. MAA prepared the samples, carried out experiments, data analysis and with US, TG and AM wrote the manuscript. ST performed the DFT simulations under the supervision of US. MAA with the support of MW and TG performed cryogenic measurements. AP and MAA performed the hysteresis related experiments under the supervision of TK. KW and TT provided hexagonal boron nitride crystals. DY and YS provided the $PtSe_2$ crystals. EP and VT designed and provided gold patterned substrates. AM acquired the main funding for the study. All the authors discussed the results and reviewed the manuscript.

Additional information

Supporting Information: The online version contains the supplementary information.

Competing financial interests: The authors declare no competing financial interests.

Keywords: $PtSe_2$, transistors, graphene, Schottky junction, contact resistance

5.4 Multi–layer palladium diselenide as a contact material for two–dimensional tungsten diselenide field–effect transistors

Gennadiy Murastov , **M. Awais Aslam**, Simon Leitner, Vadym Tkachuk, Iva Plutnarova, Egon Pavlica, Raul D. Rodriguez, Zdenek Sofer, and Aleksandar Matkovic 2024. Multi–layer paladium diselenide as a contact material for two–dimensional tungsten diselenide field–effect transistors.

This work proposes a strategy to fabricate WSe_2 devices for effective electron or hole injection with stable V_{th} and excellent subthreshold swing while employing $PdSe_2$ electrodes. Considering the low temperatures required for the $PdSe_2$ growth, it is a promising electrode candidate especially for up–scaling of 2D materials–based electronics and incorporation of ambipolar WSe_2 to post–CMOS architectures. The study demonstrates that $PdSe_2$ contacts favor hole injection while preserving the ambipolar nature of the channel material. This consequently yields high performance p-type WSe_2 devices with a minimal hysteresis of 55 mV and subthreshold swings ranging from 98 to 150 mV/dec. Further, we explore the tunability of the contact interface by selective laser alteration of the WSe_2 under the contacts, enabling pinning of the threshold voltage to the valence band of WSe_2, yielding pure p–type operation of the devices [105].

Status: Published in the peer-reviewed journal: MDPI Nanomaterials

Contribution of the author of the thesis: Conceived the idea of the study. Carried out complete data analysis and evaluation. Prepared the figures and wrote the manuscript with the support of all co-authors.

nanomaterials

MDPI

Article

Multi-Layer Palladium Diselenide as a Contact Material for Two-Dimensional Tungsten Diselenide Field-Effect Transistors

Gennadiy Murastov [1,†], Muhammad Awais Aslam [1,†], Simon Leitner [1], Vadym Tkachuk [2], Iva Plutnarova [3], Egon Pavlica [2], Raul D. Rodriguez [4], Zdenek Sofer [3] and Aleksandar Matković [1,*]

[1] Chair of Physics, Department Physics, Mechanics and Electrical Engineering, Montanuniversität Leoben, Franz Josef Strasse 18, 8700 Leoben, Austria; genboysk@gmail.com (G.M.); muhammad-awais.aslam@stud.unileoben.ac.at (M.A.A.); simon.leitner@stud.unileoben.ac.at (S.L.)
[2] Laboratory of Organic Matter Physics, University of Nova Gorica, Vipavska 13, SI-5000 Nova Gorica, Slovenia; vadym.tkachuk@ung.si (V.T.); egon.pavlica@ung.si (E.P.)
[3] Department of Inorganic Chemistry, University of Chemistry and Technology Prague, Technická 5, 166 28 Prague, Czech Republic; plutnari@vscht.cz (I.P.); zdenek.sofer@vscht.cz (Z.S.)
[4] Research School of Chemistry & Applied Biomedical Sciences, Tomsk Polytechnic University, Lenina ave. 30, 634034 Tomsk, Russia; raul@tpu.ru
* Correspondence: aleksandar.matkovic@unileoben.ac.at
† These authors contributed equally to this work.

Abstract: Tungsten diselenide (WSe_2) has emerged as a promising ambipolar semiconductor material for field-effect transistors (FETs) due to its unique electronic properties, including a sizeable band gap, high carrier mobility, and remarkable on–off ratio. However, engineering the contacts to WSe_2 remains an issue, and high contact barriers prevent the utilization of the full performance in electronic applications. Furthermore, it could be possible to tune the contacts to WSe_2 for effective electron or hole injection and consequently pin the threshold voltage to either conduction or valence band. This would be the way to achieve complementary metal–oxide–semiconductor devices without doping of the channel material.This study investigates the behaviour of two-dimensional WSe_2 field-effect transistors with multi-layer palladium diselenide ($PdSe_2$) as a contact material. We demonstrate that $PdSe_2$ contacts favour hole injection while preserving the ambipolar nature of the channel material. This consequently yields high-performance *p*-type WSe_2 devices with $PdSe_2$ van der Waals contacts. Further, we explore the tunability of the contact interface by selective laser alteration of the WSe_2 under the contacts, enabling pinning of the threshold voltage to the valence band of WSe_2, yielding pure *p*-type operation of the devices.

Keywords: palladium diselenide; tungsten diselenide; tungsten selenium oxide; semi-metal; laser treatment; contact engineering; field-effect transistor; pMOS; van der Waals electronics; 2D materials

Citation: Murastov, G.; Aslam, M.A.; Leitner, S.; Tkachuk, V.; Plutnarova, I.; Pavlica, E.; Rodriguez, R.D.; Sofer Z.; Matković, A. Multi-Layer Palladium Diselenide as a Contact Material for Two-Dimensional Tungsten Diselenide Field-Effect Transistors. *Nanomaterials* **2024**, *1*, 0. https://doi.org/

Academic Editors: Filippo Giannazzo, Simonpietro Agnello, Luca Seravalli and Federica Bondino

Received: 15 January 2024
Revised: 28 February 2024
Accepted: 1 March 2024
Published:

Copyright: © 2024 by the authors. Licensee MDPI, Basel, Switzerland. This article is an open access article distributed under the terms and conditions of the Creative Commons Attribution (CC BY) license (https://creativecommons.org/licenses/by/4.0/).

1. Introduction

Two-dimensional (2D) materials, and especially 2D semiconductors, are emerging as ever-more promising platforms to be added into very-large-scale integration (VLSI) technologies [1,2]. This is driven by the shrinking pitch sizes required to achieve higher integration density, energy efficiency, and speed of electronic circuits [3,4]. To achieve this feat, comprehensive studies have been undertaken to offer 2D channel materials and insulators [5,6] with performance parameters comparable to those of silicon-based technologies. Both traditional (Al_2O_3/HfO_2) and 2D insulators have shown promising results in developing complex architectures [7,8]. Similarly, a huge library of 2D semiconductors is available for the purpose of choosing *p*-type, *n*-type, or ambipolar channel materials [9,10]. In this regard, ambipolar WSe_2 has garnered keen interest in the scientific community due to its potential applications towards complementary metal–oxide–semiconductor (CMOS) technology, solar cells, water splitting, light emitting, and gas sensing [11–15]. Moreover,

patterned nanoribbons of WSe_2 have been shown to offer high electrical performance and the possibility to be coupled with metallic nanoparticles, which offers exciting possibilities in optoelectronic applications and tunable catalysis [16,17]. Like other 2D materials, the properties of WSe_2 can be tuned via thickness [18], plasma treatment [19], strain [20], and choice of contacts [21,22].

However, the development of technology-relevant metal–semiconductor interfaces remains a significant bottleneck for the integration of 2D semiconductors into VLSI [1,23]. This is also true for achieving high-quality contacts to ambipolar WSe_2. The existing metal electrode deposition technologies cause the degradation of the 2D materials at the contact interface by the formation of metal-induced gap states (MIGS) and defect-induced gap states. In turn, these gap states result in the formation of large barriers at the junctions, consequently lowering the device performance and increasing energy consumption [24,25]. In addition to the creation of potential barriers, MIGS also alter transport fundamentally by changing transmission around the transport gap. An example of this can be seen in metallization-induced change of the quantum limits of contact resistance in one-dimensional contacts to semiconducting graphene nanoribbons [26]. There have been several efforts to find suitable contact materials and contact deposition methods to realise the full potential of 2D material-based circuits. These include the use of edge contacts [27,28], low-work-function metals [29], ultra-high vacuum evaporation [30], buffer layers [31], self-assembled dipolar monolayers [32], and dry stamping of metal electrodes [33,34]. In particular, metallised edge contacts are commonly the best-performing technology in large-area 2D material-based devices [27,28]. However, this is not the case for one-dimensional (1D) or quasi-1D nanostructures of 2D materials such as nanoribbons and nanowires, as phosphorene nanodevices with edge contacts [35,36].

More recently, semi-metallic contacts such as bismuth, antimony, and graphene have shown promising results [37–39]. However, semi-metal depositions involve heating of the substrate up to 100 °C to achieve a particular orientation of the metal (Sb $011\bar{2}$ on MoS_2), which tends to introduce defects into heat-sensitive 2D semiconductors with ambipolar functionality, such as WSe_2 [40,41] and black phosphorus [42]. In case of graphene contacts, the growth of graphene films as top electrodes would require very high temperatures [43], hindering direct growth as the incorporation path to the back-end-of-line (BEoL) processes. However, ambipolar 2D materials are critical for CMOS electronic applications. It is essential to develop contacts which preserve the ambipolar behaviour while providing sufficient on-state currents and I_{ON}/I_{OFF} ratios relevant for technological aspects. To address this challenge, significant efforts have been made, including the use of In and Pd contacts to WSe_2 [44,45].

The use of $PdSe_2$ as a contact material was first demonstrated by Oyedele et al., who employed defective $Pd_{17}Se_{15}$ as contacts with $PdSe_2$ to demonstrate a low Schottky barrier [46] and later by Seo et al. for the realization of $PdSe_2$-based CMOS devices [47]. $PdSe_2$ has also been used to contact MoS_2 in a junction field effect transistor as a top gate due to its promising optoelectronic properties which include long-wavelength infrared photo responsivity [48–51]. With a layer-dependent bandgap in the infrared region, $PdSe_2$ itself is a unique member of the transition metal dichalcogenide family with potential uses in optoelectronic devices [52]. It behaves as a semi-metal for thicknesses above 20 nm and transforms to a semi-conducting state for thinner layers [53,54]. Large-area $PdSe_2$ can be grown at temperatures as low as 250 °C [55], unlike graphite, which makes it critical for BEoL integration as a van der Waals electrode material. Moreover, graphite contacts dope the WSe_2 towards a dominant n-type electrical response, therefore disrupting the ambipolar nature of WSe_2 [56].

In this work, we propose $PdSe_2$ contacts to WSe_2 which demonstrate high I_{ON}/I_{OFF} ratio and high on-state currents while maintaining the intrinsic ambipolar behaviour of the channel material. To further tune the behaviour of our devices, we propose localised laser treatment of WSe_2 at the contact regions to demonstrate dominant p-type FETs with high threshold voltage stability. This can allow for the co-integration of p-type and ambipolar

devices in a circuit without the need to change the contact material nor the need to introduce any dopants into the channel.

2. Materials and Methods

2.1. $PdSe_2$ Crystal Growth

$PdSe_2$ crystals were synthesised by direct reaction of elements in a quartz glass ampoule. Powder palladium (99.99%, −100 mesh, Safina, Vestec, Czech Republic) and selenium granules (99.9999%, 2–4 mm granules, Wuhan Xinrong New Material Co., Wuhan, China) corresponding to 3 g of $PdSe_2$ were placed in a quartz ampoule (25 × 100 mm) with additional selenium corresponding to 1% in excess. The ampoule was melt sealed under a high vacuum (1×10^{-3} Pa) using an oxygen–hydrogen torch and placed in muffle furnace. The ampoule was heated at 850 °C using a heating rate of 1 °C/min, and after 12 h it was cooled to room temperature at a cooling rate of 0.1 °C/min. The ampoule with formed $PdSe_2$ crystals was opened in an argon-filled glove box.

2.2. Device Fabrication

Using laser lithography (DaLi) and thermal evaporation, 45 nm/5 nm stripe-like Au/Cr electrodes were patterned onto a 300 nm SiO_2/Si substrate. hBN flakes were used as a bottom gate oxide on top of one the Au pads. Multi-layer $PdSe_2$ or crystal (kish) graphite flakes were placed on top of the WSe_2 flakes as source and drain electrodes. Flakes of 2D materials were mechanically exfoliated from bulk single crystals using commercially available Nitto tape and polydimethylsiloxane (PDMS) Gel–Pak–DLG–X4. The flakes were selected based on optical contrast and transferred one by one to build up the devices. The thickness of the hBN used for the devices was approximately 20 nm, considering a value for the relative dielectric constant of ϵ_r = 3.5 [57]. Further, optical microscopy, atomic force microscopy (AFM), and Raman spectroscopy measurements were performed to confirm the layer thickness, uniformity, and exact device geometries.

2.3. Electrical Characterization

Room temperature (RT) and low-temperature (78 K) electrical characterizations were performed using a Keithley 2636A Source Meter attached to an Instec probe station. The samples were contacted via Au-coated Ti electrical cantilever microprobes. The mK2000 temperature controller was used to monitor the temperature with a resolution of 0.01 K. The cooling and heating rates were 20 °C/min and 10 °C/min, respectively.

2.4. FET Figures of Merit (FOM) Extraction and Device Modelling

The off-state current (I_{OFF}) was defined as the minimum in $I_D(V_G)$ curves, while the on-state current (I_{ON}) was defined as the maximum obtained in $I_D(V_G)$ for the electron or hole branch. The maximum current is limited by the amount of the electrostatic field that can be applied through the back gate, and I_{ON} was estimated 5 to 8 V away from the threshold voltage (V_{th}). The threshold voltage was estimated by extrapolation of the linear fit to the point of intersection of the I_D = 0 A line. The linear fit was performed in the V_G region shifted by 2 V from the onset voltage point (V_{on}) and by 4 V to 5 V from the V_{on}. The onset voltage point was defined as the V_G point from which the I_D continuously increases from the gate leakage levels (usually 0.5–2 × 10^{-11} A). The middle of the region between V_{on} and V_{th} was used to estimate the sub-threshold swing (SS) values.

Modelling of the FET output curves was performed using the ideal transistor operating in the linear regime, shifted by the V_{th} via a capacitor at the gate. To model the non-ideal and non-linear behaviour of the contacts, a linear resistor and a Schottky diode were added in series to the ideal transistor. The current through the transistor was described as: $I_D = (\mu C_{ox} W/L) \cdot ((V_G - V_{th}) \cdot V_{FET} + (V_{FET}^2/2))$. Here, V_{FET} corresponds to the fraction of the total V_D bias that is experienced by the ideal transistor, C_{ox} is the area-specific gate dielectric capacitance, and μ is the intrinsic mobility. Upon reaching the limit of the linear regime—defined as the maximum $I_D(V_{FET})$ value of the model—the maximum current

level was kept independent of the V_{FET}, describing the saturation of the device. The ohmic component of the contact resistance is defined by a linear resistor, with its corresponding potential drop described as $V_{ohmic} = R_{ohmic} \cdot I_D$. The non-linear component of the contact resistance is described by: $V_{junction} = V_{thermal} \ln(1 + I_D/I_0))$. Here, $V_{thermal} = k_B T/e$ and k_B stands for the Boltzmann's constant, T is fixed to the set temperature of the experiment, and e is the unit charge. I_0 represents the reverse current of the Schottky diode. Considering that $V_D = V_{FET} + V_{ohmic} + V_{junction}$ the system is solved in a self-consistent manner using three fitting parameters: μ, R_{ohm}, and I_0. In the first fitting iteration, the parameters are assumed to be independent of V_G and are fitted to the sequence of the electrical output curves for the hole or the electron branch. In the second iteration, for each V_G the parameters are allowed to vary by $\pm$20% from the previously determined values. The contact resistance is further expressed as a device width-scaled (W) value: $WR_C = W((V_{ohmic} + V_{junction})/I_D)$.

2.5. Laser Treatment of WSe_2

The freshly exfoliated channel WSe_2 was laser-treated (532 nm, 100$\times$ objective) under ambient conditions using a motorised sample stage. The laser modification of WSe_2 was performed prior to the transfer of $PdSe_2$ contacts. The laser power was set to 50 mW. A point-to-point scan was carried out with a resolution of 0.2 µm, and a fixed exposure time of 0.1 s for each point.

2.6. AFM and In Operando KPFM Measurements

Horiba/AIST-NT Omegascope AFM system was used for the AFM topography measurements, with Nunano SPARK 350 Pt probes (spring constant of 42 Nm^{-1}, resonant frequency 330 kHz, and tip radius of 30 nm). Topography images were processed in the open-source software Gwyddion v2.56 [58], applying zero-order line correction and three-point plane averaging.

In operando Kelvin Probe Force Microscopy (KPFM) measurements were carried out on $PdSe_2$-contacted devices under the ambient conditions. To prevent device degradation during prolonged ambient operation, the devices for the KPFM experiments were top capped by an additional 10 nm thick hBN flake. For the device biasing during the KPFM measurements, a Keithley 2636A Source Meter was used, and the device ground (source) was connected to the ground of the KPFM feedback loop. KPFM was operated in a frequency-modulated two-pass regime with a second-pass lift height of 8 nm, yielding a total of about 18 nm distance between the probe and the hBN capped channel. To extract electrostatic potential drops across the channel of an operating device, a single line in the middle of the device was repeatedly scanned while the external bias was applied. To compensate for the work function and stray field differences, each potential drop is normalised to the cross-sections recorded with V_D = 0 V, following the procedure detailed in Ref. [32].

2.7. Raman Spectroscopy

Raman spectroscopy measurements were performed using a Horiba LabRam HR Evolution confocal Raman spectrometer with 1800 lines/mm gratings. A 532 nm laser was used with an excitation power in the range of 0.1–3.2 mW. The laser spot was focused by a 100$\times$, 0.9 NA objective.

3. Results and Discussions

3.1. Electrical Characteristics of WSe_2 FETs with Graphite and $PdSe_2$ Electrodes

Figure 1a depicts a schematic representation of the 2D layer stacks along with optical images of the typical devices with graphite (Gr) and $PdSe_2$ contacts. Figure 1b,c present in a semi-log scale the device width-scaled electrical transfer curves, source–drain current as a function of the applied local back gate bias $I_D(V_G)$, comparing the two different types of van der Waals contacts (Gr and $PdSe_2$) to multilayered WSe_2. For each transfer curve, five subsequent forward and backward V_G sweeps were carried out at 2 V/s. In both cases,

a small hysteresis of 200 mV was observed. The measurements were carried out at 78 K to minimise charge-trap-related effects and unintentional doping effects from the trapped water and air at the interfaces [16,59,60]. Graphite-contacted devices showed a dominant *n*-type behaviour which was previously reported and attributed to the band alignment that favours electron injection from the graphite towards the channel material [56,61]. In Figure 1b, the second device (Device 2) also exhibits notably high current in the hole branch, however, the threshold voltage remains closer to the electron branch, as expected for the efficient electron injection from graphite electrodes [56].

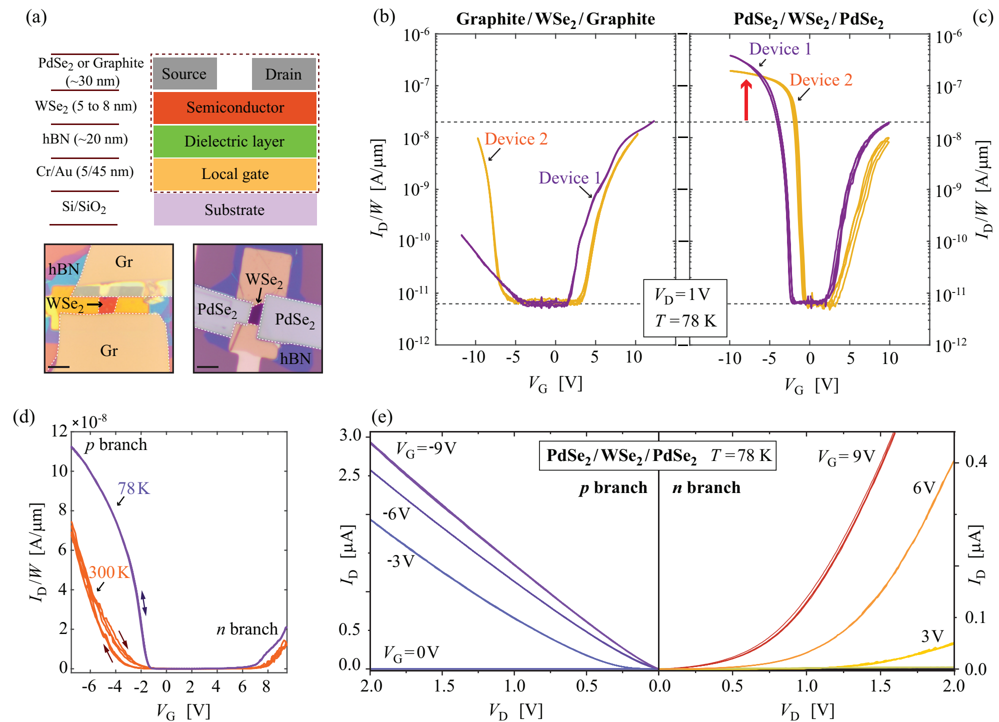

Figure 1. Electrical characteristics of graphite- and $PdSe_2$-contacted WSe_2 FETs: (**a**) Schematic representation of device configuration with optical images of WSe_2 FETs (scale bar: 10 μm). (**b**,**c**) Semi-log electrical transfer curves of devices with graphite (Gr) and $PdSe_2$ contacts, respectively. The I_D in (**b**,**c**) is scaled by the mean width of the channels to allow for better comparison of the current values between the different devices. The horizontal dashed lines that interconnect (**b**,**c**) serve as a guide to see the reached on- and off-state current levels. The red arrow in (**c**) indicates over an order of magnitude larger current of the hole branch in the case of $PdSe_2$ contacts. (**d**) Comparison of the device width-scaled electrical transfer curves ($PdSe_2$ contacted device) measured at 300 K (orange) and 78 K (purple), presented in linear scale. The arrows indicate the direction of the V_G sweep, highlighting an increase in the hysteresis observed at 300 K. (**e**) Output curves for the hole and electron branches at 78 K (2×10^{-2} mbar) of a device with $PdSe_2$ contacts. Note that the current values for the *n*-branch are approximately one order of magnitude lower than for the *p*-branch.

The main difference in the electrical transfer curves between Gr and $PdSe_2$-contacted devices occurs at the negative V_G values, i.e., in the hole branch. In contrast to graphite-contacted devices, when $PdSe_2$ is used as a contact, the FETs were found to exhibit dominant *p*-type behaviour and an increased device performance for both electron and hole branches. This is explained by the favoured level alignment of the $PdSe_2$ with the hole branch of the WSe_2 due to the higher work function of $PdSe_2$ in comparison to graphite. The I_{ON}/I_{OFF} ratio for $PdSe_2$ ($\sim 4 \times 10^4$) was one order of magnitude better than that of graphite contacts. Horizontal dashed lines that interconnect Figure 1b,c serve as a guide to help compare the current levels. For the WSe_2 devices reported in the literature, the I_{ON}/I_{OFF} ratio varies

over several orders of magnitude [11]: from 10^2 (e.g., $NbSe_2$ contacts to the *n*-branch [56]) up to 10^9 with more elaborate device architectures and high-k dielectrics [18]. With respect to the electrode engineering to access the *p*-branch, $NbSe_2$- and Pt-contacted WSe_2 were reported to reach the values in the range 10^4–10^7 [18,56].

Furthermore, $PdSe_2$-contacted devices maintained an intrinsic behaviour which is evident by an almost equidistant V_{on} for both electron and hole branches with reference to $V_G = 0$ V. This was not the case for graphite-contacted devices where larger V_G was required to reach the on state of the *p*-branch compared to the *n*-branch, therefore indicating a disruption in the intrinsic doping levels. On average, we observe a V_{on} for the hole branch to be at (-4.5 ± 0.9) V and at (-1.9 ± 1.3) V respectively for the Gr and $PdSe_2$ contacts; similar values for the V_{on} were observed for the electron branch: (2.5 ± 1.7) V and (3.0 ± 0.8) V respectively for the Gr and $PdSe_2$ contacts.

A comparison between 300 K and 78 K width-scaled transfer curves of a $PdSe_2$-contacted device are presented in Figure 1d. The temperature primarily impacts the phonon-related carrier scattering in the channel, the Schottky junction-related potential drop, and gate dielectric interface charge trap states. Consequently, at lower temperatures we observe an overall increase in the drain currents and mobilities for both branches (by a factor of $\sim$2 comparing 78 K and 300 K), quenching of the hysteresis with respect to the forward and backward V_G sweeping, and a minor reduction in the V_{th} values.

Figure 1e represents the electrical output curves for the $PdSe_2$-contacted channel; the source–drain current as a function of the applied source–drain bias is $I_D(V_D)$. Especially at more negative V_G values (on state of the *p*-branch), the electrical output curves of the *p*-branch exhibit linear behaviour. For the *n*-branch, the overall I_D values are about one order of magnitude lower than that of the *p*-branch and show significant deviation from the linear behaviour at lower V_D values regardless of the applied V_G. All of these observations indicate that a significantly larger barrier exists for the electron than for the hole injection from $PdSe_2$ into WSe_2. At low temperatures, within the applied V_D range and for V_G more than 0.5 V away from the V_{th}, we did not observe the current saturation. However, within the same bias range at room temperature, saturation can be achieved (see Figure 2).

3.2. Contact Resistance of the $PdSe_2$/WSe_2 Interface

The contact resistance of the interface between $PdSe_2$ and WSe_2 was evaluated independently by two approaches: parameter extraction via device modelling and direct measurements by in operando KPFM. In the first approach, we have modelled the sequence of the electrical output data by applying an equivalent electrical scheme as shown in Figure 2a (see also Section 2). The system was solved in a self-consistent manner and fitted to the set of output curves either for the hole or for the electron branch, as presented in Figure 2b,c. Parameters of the ohmic (R_{ohm}) and non-linear Schottky component (I_0) of the contact resistance were extracted, and width-scaled contact resistance (WR_C) was expressed considering specific points of operation (fixed V_D, V_G, and, consequently, I_D values). We obtain $WR_C = (2.84 \pm 0.53) \times 10^6$ Ωμm for the hole branch and $WR_C = (3.72 \pm 0.69) \times 10^8$ Ωμm for the electron branch. The values are reported for the operation at 300 K, with V_G set 5 V away from the V_{th} in both cases of the hole and the electron branches, and under 1.5 V of source–drain bias. In particular, the need to include the non-linear Schottky element in the model is evident in a strong downward bending of the output curves at lower V_D, as pointed out by the red arrows in Figure 2c. Especially in the electron branch case, at lower I_D the contact resistance and the entire device operation is Schottky junction-dominated, and almost all of the applied V_D is taken by this junction as the most resistive element in the circuit. At higher I_D, the $V_{junction}$ still dominates over V_{ohmic} by a factor of 5 to 10.

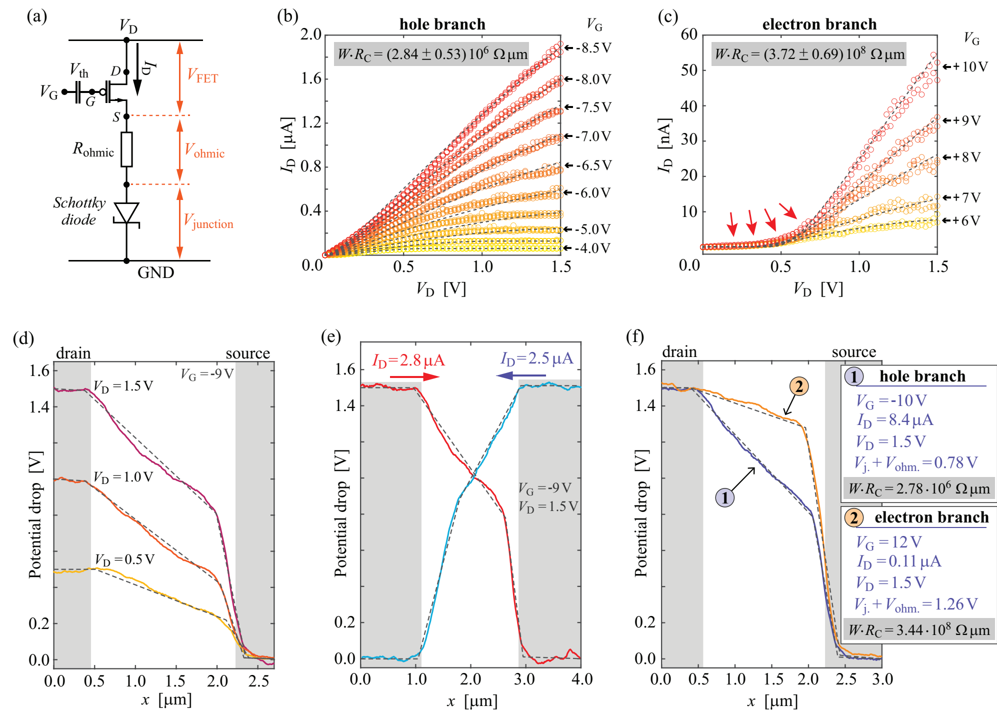

Figure 2. Contact resistance of the $PdSe_2/WSe_2$ interface: (**a**) equivalent electrical scheme used for the self-consistent modelling of the output curves. (**b**,**c**) Electrical output curves of a $PdSe_2/WSe_2/PdSe_2$ device measured at 300 K for the hole and electron branches, respectively. Circles represent the measured I_D values at set different V_G as indicated in the right corner of the sub-panels (**b**,**c**). The dashed lines are a model for the entire data set. Red arrows in (**c**) indicate a severe downward bending of the output curves at lower V_D. Contact resistance values (WR_C) extracted by modelling the curves from (**b**,**c**) are indicated in each sub-panel. (**d**–**f**) in operando KPFM potential profiles recorded as single lines across the channel, measured under ambient conditions. Solid lines present the work function difference corrected potential drops, and the dashed lines are linear fits to the experimental curves. (**d**) A sequence of the potential drops with varied V_D. (**e**) Alternating the source and drain contacts, which demonstrates that the steep potential drop is related to the grounded electrode. (**f**) Comparison of the potential drops at V_D = 1.5 V, with V_G setting the device in an on state of the hole and electron branches, labelled with (1) and (2), respectively. Insets in (**f**) provide the operation points and the extracted WR_C values from the KPFM measurements.

In the second approach to evaluating the contact resistance of the $PdSe_2/WSe_2$ interface, we have used in-operando KPFM. This technique measures the electric potential several nanometres above the channel during device operation. Therefore, it resolves the potential drops between the electrodes, and allows independent distinguishing of the potential drops that correspond to the drain (not observed in our case), the channel, and the source [16,32]. An example of the potential drop profiles is presented in Figure 2d in the hole branch on state and for varied V_D between 0.5 V and 1.5 V. Four regions are clearly distinguishable in the potential drop profiles: flat potential values corresponding to the source and drain regions of the scan, a monotone drop of the potential along the channel, and a much steeper drop at the contact to the source electrode. Linear fits to these elements are presented by dashed black lines. The steeper drop connected to the transition between the channel-related potential drop and the source contact region is directly related to the $V_{junction} + V_{ohmic}$ in the device model. Knowing the I_D values during the potential drop profile measurements and the width of the device, it is possible to express the observed junction-related potential drop as the width-scaled contact resistance.

Figure 2e presents the potential drop profiles when the connections between the source and the drain are exchanged, effectively reversing the current flow direction. We observe

that the contact resistance associated potential drop is connected to the grounded source electrode, i.e., that the $PdSe_2/WSe_2$ interface is rectifying. This proves the predominant Schottky nature of the contact resistance, as also suggested by the model.

Lastly, when biased under very similar operation points as in the case of the contact resistance extraction from the electrical output data sets (Figure 2f), we obtain the following device width-scaled contact resistance values obtained from in operando KPFM: $WR_C = 2.78 \times 10^6$ Ωµm for the hole-branch and $WR_C = 3.44 \times 10^8$ Ωµm for the electron branch.

The obtained WR_C values imply that $PdSe_2$ is an effective hole injector. This is seen from the two orders of magnitude larger contact resistance of the electron branch under similar operation conditions. Furthermore, the contact resistance of the $PdSe_2/WSe_2$ interface for *p*-type operation performs similar to the commonly employed evaporated metallic contacts [62,63] while preserving the intrinsic doping levels and the ambipolar nature of the WSe_2. Reported values for WSe_2 contact resistance range from 10^8 Ω µm to 10^5 Ω µm with electrostatic gating and down to 10^4 Ω µm for electrolyte gating that can induce very high density states in WSe_2 [45,56,62]. Some of the lowest values reported for the contact resistance (1.1×10^5 Ω µm) are with Pt electrodes, where MIGS cannot be excluded at the electrode interface [45].

3.3. Optimizing Contact Interface via Laser-Driven Oxidation of WSe_2

Recent work has shown that the application of mild oxygen plasma can be an effective way to reduce the Schottky barrier in multilayer WSe_2 FETs [64–66]. The plasma treatment causes the formation of a conductive tungsten selenium oxide (WSe_yO_x). The oxide was found to form in a layer-by-layer manner [64,65], effectively generating a WSe_yO_x/WSe_2 heterostructure that acts as a facilitator for the hole injection [66,67]. However, it is important to protect the channel active area during the plasma treatment to avoid device degradation. We wanted to investigate if a laser-based approach could open a way to achieve similar modification of WSe_2, as with the mild plasma treatment. An advantage of the laser-driven oxidation approach is straightforward patterning by laser scanning. Using laser irradiation (532 nm, 50 mW) under the ambient conditions, we have observed a similar oxidation process of WSe_2.

To explore the influence of the WSe_yO_x layer on the contact properties between WSe_2 and $PdSe_2$, we have irradiated an area of the WSe_2 flake that is slightly larger than the contact area with $PdSe_2$. After the laser treatment, $PdSe_2$ flakes were transferred and used as contacts. Figure 3a(*i*–*iii*) show the schematic representation of the laser treatment and the device assembly process for the WSe_yO_x-modified contacts. Figure 3b(*i*–*iii*) represent the corresponding optical images of the flake and the final device, where only one side of the flake was treated by the laser. Figure 3c presents a zoomed-in region of the interface to highlight the parts of the ablated layers, oxidised layers, and remaining pristine WSe_2 layers.

AFM was performed to observe the morphological and height changes due to laser treatment. The results are presented in Figure 4a,b. AFM image before laser treatment shows large bubbles formed at the interface between WSe_2 and hBN, as well as between hBN and SiO_2 interface. This is expected for 2D material heterostructures assembled under ambient conditions and using PDMS stamps due to the entrapment of air and water [68–70]. Such interfaces result in localised charge-trap and scattering centres, and a flat interface is desired to achieve better performance [71,72]. Interestingly, laser treatment resulted in the removal and migration of these bubbles from the scan area, even at the regions not directly exposed to the laser irradiation. This is illustrated in Figure 4b. Such behaviour can be attributed to the self-cleaning property of 2D materials under a systematic sweep of the laser spot which allows local heating and migration of the trapped water/air bubbles at the interfaces [71,72]. The arrows in Figure 4b represent the direction of laser sweeping, and the dashed rectangle indicates the laser-exposed area. Figure 4a,b (bottom) show the change in height of the flake before and after the treatment. The resultant height corresponds to a thickness of 3.9 nm. This indicates the ablation of about five mono-layers of WSe_2, and the remaining flake effectively

forms a WSe_yO_x/WSe_2 heterostructure. Combined with Raman spectroscopy data (Figure 4c) we estimate that after the laser treatment, about three layers of WSe_2 remain, with about 2 nm of WSe_yO_x formed on top [64–66]. Raman spectroscopy was also performed to verify the crystal quality of the laser-modified flakes. Figure 4c presents the Raman spectra before and after the laser treatment of a WSe_2 flake. The increase in the Raman intensity of the A_{1g} mode (shown in the inset) after the treatment validates the thinning of WSe_2 with the oxidation of top layers. Such an increase in the intensity of the peaks is related to the thinning of WSe_2 and an increase in the phonon lifetime [45,73]. An increase in phonon lifetime should be also observed in the according change in the device-apparent field-effect mobility. However, for both treated and the untreated devices, the apparent hole mobilities were within the sample-to-sample variation.

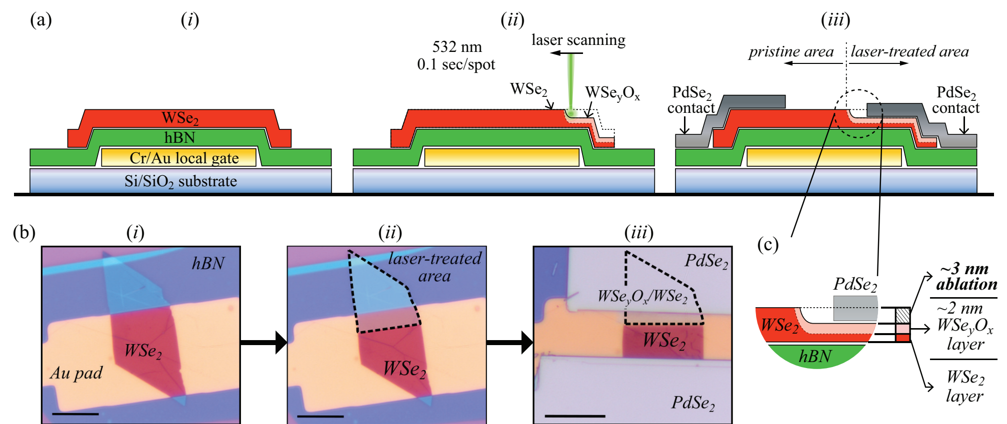

Figure 3. Laser treatment of WSe_2: ((**a**) *i*–*iii*) schematic cross-section of the laser-treated devices (not to scale), presenting the laser treatment process of the electrode interface step by step. ((**b**) *i*–*iii*) optical micrographs (scale 5 µm) of a representative device corresponding to each fabrication step in ((**a**) *i*–*iii*). ((**a**,**b**) *i*) The heterostack of WSe_2/hBN on a local gate electrode prior to the laser treatment, and ((**a**,**b**) *ii*) after the top part of the WSe_2 flake was scanned by the laser (exposed part of the WSe_2 flake is indicated by the dashed lines). ((**a**,**b**) *iii*) The same device after stamping of $PdSe_2$ contacts. In the presented case, only one side of the channel–electrode interface was laser-treated. (**c**) A zoom in on the schematic in ((**a**) *iii*) highlighting the part of the ablated WSe_2 layer, part of the oxidised WSe_yO_x layer, and the unmodified part of the WSe_2 layer.

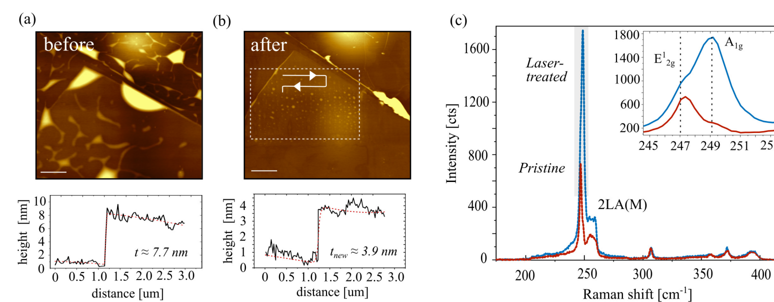

Figure 4. Topography changes and Raman investigation of laser-treated WSe_2: (**a**) Atomic force microscopy (AFM) image of a WSe_2 flake on hBN before laser exposure with the corresponding line profile (height) of the flake. The predominant morphological features are water/air bubbles trapped at the WSe_2/hBN and hBN/SiO_2 interfaces. (**b**) The same area as in (**a**) treated with a 50 mW 532 nm laser beam. The exposed region is marked with a dashed rectangle, and the laser scanning direction is indicated with an arrow. The corresponding height profiles are presented at the bottom of the topography images. (**a**,**b**) Lateral scale bar 2 µm, z-scale 25 nm. (**c**) Raman spectrum before and after laser irradiation, recorded with 5 mW, 532 nm, and 5×10 s acquisition parameters. The main WSe_2 peaks are preserved and enhanced in intensity after the laser treatment. Inset (**b**) presents a zoomed-in region of the main $E^1{}_{2g}$ and A_{1g} modes.

3.4. Electrical Characteristics of WSe_2 FETs with $WSe_2/WSe_yO_x/PdSe_2$ Electrode Interface

Figure 5a represents the electrical transfer curves for the WSe_2 device with both source and drain electrode interfaces modified by the laser treatment. The device showed a notable decrease in I_{ON}. However, highly stable *p*-type devices were realised with respect to V_{th} variations between subsequent sweeps at room temperature operation and also under varied V_G sweeping rates. V_{th} for the hole branch of the WSe_yO_x-modified contacts was found to be at (-0.42 ± 0.06) V, which is about four times lower than the $PdSe_2/WSe_2$ interface. More importantly, the sample-to-sample-, forward/backward sweep-, and multiple sweep-related variations in the V_{th} value are almost completely reduced. The dominant *p*-type behaviour with the quenching of the electron branch can be associated with WSe_yO_x, which acts as an efficient hole injection layer [66,67]. The WSe_yO_x/WSe_2 layer also extends beyond the contact regions into the channel (for about 1 µm) to ensure that the contact is not made directly with the unmodified WSe_2. Consequently, WSe_yO_x could also introduce interface traps in the channel active area. To test this, we have probed the stability of the devices by examining the hysteresis voltage (V_H), as a difference in the V_{th} between the forward and backward sweeping electrical transfer curves. V_H values for the varied V_G sweep rates are shown in Figure 5b. The device remained stable at high sweeping rates (up to 15 V/s) with a negligible hysteresis of 55 mV. An increase in the hysteresis of up to 150 mV was noted at low sweeping rates. The hysteresis values correspond well to the pristine $PdSe_2/WSe_2/PdSe_2$ devices, indicating that the WSe_yO_x layers did not affect device stability. The observed hysteresis is likely related to the interface between hBN and WSe_2 or is inherent to the WSe_2 layers.

Two-dimensional semiconductors commonly show large variations in the V_{th} at varying drain voltages which also impacts the device stability [6,74,75]. To test this, we subjected our device to a V_D ranging from 0.5 V to 2.0 V. The device maintained the same V_{th} for forward and backward sweeps with a V_D-independent hysteresis of 98 mV. The subthreshold swing (SS) values were also significantly improved from 200 mV/dec for the non-treated to 100 mV/dec for the treated devices. It is worth mentioning that these devices operated without a top encapsulation and therefore, a high-k dielectric encapsulation, optimization of the hBN thickness, and integration into dual-gate geometries can further improve WSe_2 FET performance. The obtained SS values, especially for the laser-treated devices, perform better than commonly reported back-gate implemented FETs, where the SS values range from 2500 mV/dec to 400 mV/dec [11,18,20]. Some of the lowest reported SS values for WSe_2 devices (95 mV/dec) were achieved by utilizing 20 nm of HfO_2 as the gate insulator and *p*-branch matching Pt contacts [45].

We have also fabricated asymmetric devices where only one side of the channel was treated with the laser (as also shown in Figure 3). An example of the electrical transfer curves observed for such devices is presented in Figure 5d. A large hysteresis window was observed, which directly depends on the choice of the drain electrode, i.e., the device exhibits rectifying behaviour with respect to the induced hysteresis. For the case where the laser-treated region was used as a drain, a stable *p*-branch was realised with negligible hysteresis, represented by a solid black curve in Figure 5d. A pronounced hysteresis of 2 V was only present for the *n*-branch. This was observed to be in stark contrast to the behaviour of the same device when the non-treated region was used as the drain. In that case, a *p*-branch hysteresis of 4 V was observed. In both cases, the hysteresis was stable for multiple forward–backward sweeps as indicated by the arrows. Such behaviour can be associated with large differences between the number of carriers available underneath the contact regions. As one end of the channel is intentionally favouring hole injection and prohibiting electron injection, the other stays in its original form. Such large and stable rectifying hysteretic behaviour could be employed in novel concepts as computing in memory and self-reconfiguring electronics [76,77].

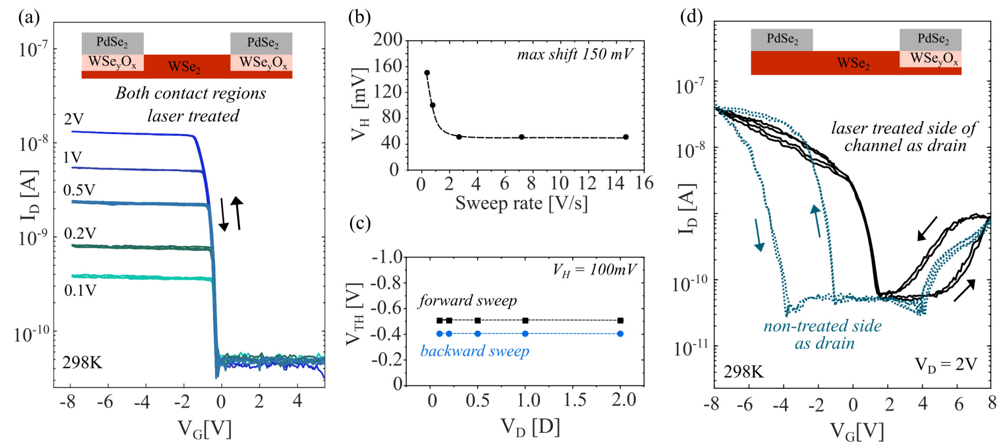

Figure 5. Electrical response of $WSe_2/WSe_yO_x/PdSe_2$ electrode interface: (**a**) Semi-log scale electrical transfer curves of a WSe_2 device with both source and drain electrode interfaces treated by a laser prior to stamping $PdSe_2$ contacts measured at 298 K, 2×10^{-2} mbar). (**b**) V_H plot as a function of a scan speed (measured at 298 K, 2×10^{-2} mbar). (**c**) Position of the V_{th} for both forward and backward V_G sweeping with varied V_D. The difference indicates the hysteresis (V_H) is independent of V_D. (**d**) Semi-log scale electrical transfer curves for an asymmetric WSe_2 FET with only one contact pad treated by the laser. The dotted lines represent the drain electrode connected to the non-treated $PdSe_2$ contact side, while source and drain were swapped for the solid black line. The arrows indicate the V_G sweeping direction.

4. Conclusions

In summary, we have introduced $PdSe_2$ contacts to WSe_2 FETs that enable effective hole injection, enhanced *p*-type performance, and preserve the intrinsic ambipolar response of WSe_2. $PdSe_2$ contacts allow essentially hysteresis-free electrical response while maintaining high on-state currents and I_{ON}/I_{OFF} ratio enhancement by one order of magnitude in comparison to graphite-contacted devices. Considering the low temperatures required for the $PdSe_2$ growth, it is a promising electrode candidate especially when considering the potential that $PdSe_2$ brings for the upscaling of 2D-material-based electronics and the incorporation of ambipolar WSe_2 to post-CMOS architectures.

We extended the study to also contact laser-treated WSe_2, where the laser irradiation induces the formation of a conductive WSe_yO_x layer at the electrode interface. In this case, we observed highly stable *p*-type behaviour of the devices with a two-fold improvement in the subthreshold swing, stabilization of the V_{th} for the hole branch. Interestingly, if only one electrode interface is modified by the laser treatment, asymmetric WSe_2 FETs were achieved, which exhibited pronounced and stable hysteretic behaviour of only one (electron or hole) branch. The hysteresis was dependent on the direction of applied drain voltage. Such device response can be used to design in-memory computing and reconfigurable electronic concepts based purely on 2D interfaces.

Author Contributions: G.M. and M.A.A. conceived the idea for the study. M.A.A. and A.M. performed data analysis and wrote the manuscript. G.M. and S.L. prepared the 2D material heterostacks and carried out the experiments. I.P. and Z.S. provided the $PdSe_2$ crystals. V.T. and E.P. fabricated the gold pad substrates. R.D.R. supervised Raman and AFM measurements. S.L. and A.M. performed the experiments and data analysis/modelling related to the extraction of the contact resistance. A.M. acquired the main funding for the study. All authors have read and agreed to the published version of the manuscript.

Funding: This work is supported by the Austrian Science Fund (FWF) under grants no. I4323-N36 and Y1298-N. A.M. acknowledges the support provided by the ERC grant POL_2D_PHYSICS (101075821). Z.S. was supported by ERC–CZ program (project LL2101) from Ministry of Education Youth and Sports (MEYS) and used large infrastructure from project reg. No. CZ.02.1.01/0.0/0.0/15_003/0000444

financed by the EFRR. R.D.R. acknowledges the Russian Science Foundation grant № 22–12–20027, and the funding from the Tomsk region administration. V.T. and E.P. acknowledge funding by the Slovenian Research and Innovation Agency (ARIS) under research program P1–0055. The authors acknowledge infrastructure support of the Montanuniversitaet Leoben (Raman AFM TERS lab).

Data Availability Statement: The data generated within this study and the samples related to this study are available from the corresponding author upon reasonable request.

Conflicts of Interest: The authors declare no conflicts of interest.

References

1. Cao, W.; Bu, H.; Vinet, M.; Cao, M.; Takagi, S.; Hwang, S.; Ghani, T.; Banerjee, K. The future transistors. *Nature* **2023**, *620*, 501–515.
2. Zhu, K.; Wen, C.; Aljarb, A.A.; Xue, F.; Xu, X.; Tung, V.; Zhang, X.; Alshareef, H.N.; Lanza, M. The development of integrated circuits based on two-dimensional materials. *Nat. Electron.* **2021**, *11*, 775–785.
3. Ahmad, W.; Gong, Y.; Abbas, G.; Khan, K.; Khan, M.; Ali, G.; Shuja, A.; Tareen, A.K.; Khan, Q.; Li, D. Evolution of low-dimensional material-based field-effect transistors. *Nanoscale* **2021**, *10*, 5162–5186.
4. Rawat, A.; Gupta, A.K.; Rawat, B. Performance projection of 2D material-based CMO inverters for sub-10-nm channel length. *IEEE Trans. Electron. Devices* **2021**, *68*, 3622–3629.
5. Fiori, G.; Bonaccorso, F.; Iannaccone, G.; Palacios, T.; Neumaier, D.; Seabaugh, A.; Banerjee, S.K.; Colombo, L. Electronics based on two-dimensional materials. *Nat. Nanotechnol.* **2014**, *9*, 768–779.
6. Li, J.; Chen, X.; Zhang, D.W.; Zhou, P. Van-der-Waals heterostructure based field effect transistor application. *Crystals* **2017**, *8*, 8.
7. Illarionov, Y.Y.; Knobloch, T.; Jech, M.; Lanza, M.; Akinwande, D.; Vexler, M.I.; Mueller, T.; Lemme, M.C.; Fiori, G.; Schwierz, F.; et al. Insulators for 2D nanoelectronics: The gap to bridge. *Nat. Commun.* **2020**, *118*, 3385.
8. Arora, A.; Ganapathi, K.L.; Dixit, T.; Miryala, M.; Masato, M.; Rao, M.S.R.; Krishnan, A. Thickness-Dependent Nonlinear Electrical Conductivity of Few-Layer Muscovite Mica. *Phys. Rev. Appl.* **2022**, *17*, 064042.
9. Zhou, J.; Lin, J.; Huang, X.; Zhou, Y.; Chen, Y.; Xia, J.; Wang, H.; Xie, Y.; Yu, H.; Lei, J.; et al. A library of atomically thin metal chalcogenides. *Nature* **2018**, *556*, 355–359.
10. Di Bartolomeo, A. Emerging 2D materials and their van der Waals heterostructures. *Nanomaterials* **2020**, *10*, 579.
11. Cheng, Q.; Pang, J.; Sun, D.; Wang, J.; Zhang, S.; Liu, F.; Chen, Y.; Yang, R.; Liang, N.; Lu, X.; et al. WSe_2 2D p-type semiconductor-based electronic devices for information technology: Design, preparation, and applications. *InfoMat* **2020**, *102*, 656–697.
12. Kumar, R.; Goel N.; Hojamberdiev, M.; Kumar, M. Transition metal dichalcogenides-based flexible gas sensors. *Sens. Actuator A Phys.* **2020**, *303*, 111875.
13. Sumesh, C.K.; Peter, S.C. Two-dimensional semiconductor transition metal based chalcogenide based heterostructures for water splitting applications. *Dalton Trans.* **2019**, *48*, 12772–12802.
14. Maniyar, A.; Choudhary, S. Visible region absorption in TMDs/phosphorene heterostructures for use in solar energy conversion applications. *RSC Adv.* **2020**, *10*, 31730–31739.
15. Wang, C.; Yang, F.; Gao, Y. The highly-efficient light-emitting diodes based on transition metal dichalcogenides: From architecture to performance. *Nanoscale Adv.* **2020**, *2*, 4323–4340.
16. Aslam, M.A.; Tran, T.H.; Supina, A.; Siri, O.; Meunier, V.; Watanabe, K.; Taniguchi, T.; Kralj, M.; Teichert, C.; Sheremet, E.; et al. Single-crystalline nanoribbon network field effect transistors from arbitrary two-dimensional materials. *npj 2D Mater. Appl.* **2022**, *6*, 76.
17. Murastov, G.; Aslam, M.A.; Tran, T.H.; Lassnig, A.; Watanabe, K.; Taniguchi, T.; Wurster, S.; Nachtnebel, M.; Teichert, C.; Sheremet, E.; et al. Photoinduced edge-specific nanoparticle decoration of two-dimensional tungsten diselenide nanoribbons. *Commun. Chem.* **2023**, *6*, 166.
18. Pudasaini, P.R.; Oyedele, A.; Zhang, C.; Stanford, M.G.; Cross, N.; Wong, A.T.; Hoffman, A.N.; Xiao, K.; Duscher, G.; Mandrus, D.G.; et al. High-performance multilayer WSe_2 field-effect transistors with carrier type control. *Nano Res.* **2018**, *11*, 722–730.
19. Nan, H.; Zhou, R.; Gu, X.; Xiao, S.; Ostrikov, K.K. Recent advances in plasma modification of 2D transition metal dichalcogenides. *Nanoscale* **2019**, *11*, 19202–19213.
20. Kozhakhmetov, A.; Stolz, S.; Tan, A.M.Z.; Pendurthi, R.; Bachu, S.; Turker, F.; Alem, N.; Kachian, J.; Das, S.; Hennig, R.G.; et al. Controllable p-type doping of 2D WSe_2 via vanadium substitution. *Adv. Funct. Mater.* **2021**, *31*, 2105252.
21. Grützmacher, S.; Heyl, M.; Nardi, M.V.; Koch, N.; List-Kratochvil, E.J.W.; Ligorio, G. Local Manipulation of the Energy Levels of 2D TMDCs on the Microscale Level via Microprinted Self-Assembled Monolayers. *Adv. Mater. Interf.* **2023**, *10*, 2300276.
22. Pang, Y.-D.; Wu, E.-X.; Xu, Z.-H.; Hu, X.-D.; Wu, S.; Xu, L.-Y.; Liu, J. Effect of electrical contact on performance of WSe_2 field effect transistors. *Chin. Phys. B* **2021**, *30*, 068501.
23. Liu, Y.; Duan, X.; Shin, H.-J.; Park, S.; Huang, Y.; Duan, X. Promises and prospects of two-dimensional transistors. *Chin. Phys. B* **2021**, *519*, 43–53.
24. Liao, W.; Zhao, S.; Li, F.; Wang, C.; Ge, Y.; Wang, H.; Wang, S.; Zhang, H. Interface engineering of two-dimensional transition metal dichalcogenides towards next-generation electronic devices: Recent advances and challenges. *Nanoscale Horiz.* **2020**, *5*, 787–807.
25. Rai, A.; Movva, H.C.P.; Roy, A.; Taneja, D.; Chowdhury, S.; Banerjee, S.K. Progress in contact, doping and mobility engineering of MoS2: An atomically thin 2D semiconductor. *Crystals* **2018**, *8*, 316.

26. Poljak, M.; Matić, M. Metallization-induced quantum limits of contact resistance in graphene nanoribbons with one-dimensional contacts. *Materials* **2021**, *14*, 3670.
27. Jain, A.; Szabó, Á.; Parzefall, M.; Bonvin, E.; Taniguchi, T.; Watanabe, K.; Bharadwaj, P.; Luisier, M.; Novotny, L. One-dimensional edge contacts to a monolayer semiconductor. *Nano Lett.* **2019**, *19*, 6914–6923.
28. Cheng, Z.; Yu, Y.; Singh, S.; Price, K.; Noyce, S.G.; Lin, Y.-C.; Cao, L.; Franklin, A.D. Immunity to contact scaling in MoS_2transistors using in situ edge contacts. *Nano Lett.* **2019**, *19*, 5077–5085.
29. Das, S.; Chen, H.-Y.; Penumatcha, A.V.; Appenzeller, J. High performance multilayer MoS_2 transistors with scandium contacts. *Nano Lett.* **2013**, *13*, 100–105.
30. English, C.D.; Shine, G.; Dorgan, V.E.; Saraswat, K.C.; Pop, E. Improved contacts to MoS_2 transistors by ultra-high vacuum metal deposition. *Nano Lett.* **2016**, *16*, 3824–3830.
31. Kwon, G.; Choi, Y.; Lee, H.; Kim, H.; Jeong, J.; Jeong, K.; Baik, M.; Kwon, H.; Ahn, J.; Lee, E.; et al. Interaction-and defect-free van der Waals contacts between metals and two-dimensional semiconductors. *Nat. Electron.* **2022**, *5*, 241–247.
32. Matković, A.; Petritz, A.; Schider, G.; Krammer, M.; Kratzer, M.; Karner-Petritz, E.; Fian, A.; Gold, H.; Gärtner, M.; Terfort, A.; et al. Interfacial band engineering of MoS_2/gold interfaces using pyrimidine-containing self-assembled monolayers: Toward contact-resistance-free bottom-contacts. *Adv. Electron. Matter.* **2020**, *6*, 2000110.
33. Liu, Y.; Guo, J.; Zhu, E.; Liao, L.; Lee, S.-J.; Ding, M.; Shakir, I.; Gambin, V.; Huang, Y.; Duan, X. Approaching the Schottky–Mott limit in van der Waals metal–semiconductor junctions. *Nature* **2018**, *557*, 696–700.
34. Liu, G.; Tian, Z.; Yang, Z.; Xue, Z.; Zhang, M.; Hu, X.; Wang, Y.; Yang, Y.; Chu, P.K.; Mei, Y.; et al. Graphene-assisted metal transfer printing for wafer-scale integration of metal electrodes and two-dimensional materials. *Nat. Electron.* **2022**, *5*, 275–280.
35. Poljak, M.; Matić, M.; Župančić, T.; Zeljko, A. Lower limits of contact resistance in phosphorene nanodevices with edge contacts. *Nanomaterials* **2022**, *12*, 656.
36. Poljak, M.; Matić, M. Optimum Contact Configurations for Quasi-One-Dimensional Phosphorene Nanodevices *Nanomaterials* **2023**, *13*, 1759.
37. Shen; Su, P.C.; Lin, C.; Chou, Y.; Cheng, A.S.; Park, C.C.; Chiu, J.H.; Lu, M.H.; Tang, A.Y.; Tavakoli, H.L.; M, M.; et al. Ultralow contact resistance between semimetal and monolayer semiconductors. *Nature* **2021**, *593*, 211–217.
38. Mootheri, V.; Arutchelvan, G.; Banerjee, S.; Sutar, S.; Leonhardt, A.; Boulon, M.; Huyghebaert, C.; Houssa, M.; Asselberghs, I.; Radu, I.; et al. Graphene based Van der Waals contacts on MoS_2 field effect transistors. *2D Mater.* **2020**, *8*, 015003.
39. Ryu, H.; Kim, D.; Kwon, J.; Park, S.K.; Lee, W.; Seo, H.; Watanabe, K.; Taniguchi, T.; Kim, S.; van der Zande, A.M.; et al. Fluorinated Graphene Contacts and Passivation Layer for MoS_2 Field Effect Transistors. *Adv. Electron. Matter.* **2022**, *8*, 2101370.
40. Li, Z.; Wang, Y.; Jiang, J.; Liang, Y.; Zhong, B.; Zhang, H.; Yu, K.; Kan, G.; Zou, M. Temperature-dependent Raman spectroscopy studies of 1–5-layer WSe_2. *Nano Res.* **2020**, *13*, 591–595.
41. Liu; Tan, Y.; Chou, C.; Nayak, H.; Wu, A.; Ghosh, D.; Chang, R.; Hao, H.Y.; Wang, Y.; Kim, X.; S, J.; et al. Thermal oxidation of WSe_2 nanosheets adhered on SiO_2/Si substrates. *Nano Lett.* **2015**, *15*, 4979–4984.
42. Illarionov, Y.Y.; Waltl, M.; Rzepa, G.; Knobloch, T.; Kim, J.-S.; Akinwande, D.; Grasser, T. Highly-stable black phosphorus field-effect transistors with low density of oxide traps. *npj 2D Mater. Appl.* **2017**, *1*, 23.
43. Wang, J.-B.; Ren, Z.; Hou, Y.; Yan, X.-L.; Liu, P.-Z.; Zhang, H.; Zhang, H.-X.; Guo, J.-J. A review of graphene synthesis at low temperatures by CVD methods. *New Carbon Mater.* **2020**, *35*, 193–208.
44. Liu, W.; Kang, J.; Sarkar, D.; Khatami, Y.; Jena, D.; Banerjee, K. Role of metal contacts in designing high-performance monolayer n-type WSe_2 field effect transistors. *Nano Lett.* **2013**, *13*, 1983–1990.
45. Zhang, L.; Zhang, Y.; Sun, X.; Jia, K.; Zhang, Q.; Wu, Z.; Yin, H. High-performance multilayer WSe_2 p-type field effect transistors with Pd contacts for circuit applications. *J. Mater. Sci. Mater. Electron.* **2021**, *32*, 17427–17435.
46. Oyedele, A.D.; Yang, S.; Feng, T.; Haglund, A.V.; Gu, Y.; Puretzky, A.A.; Briggs, D.; Rouleau, C.M.; Chisholm, M.F.; Unocic, R.R.; et al. Defect-mediated phase transformation in anisotropic two-dimensional $PdSe_2$ crystals for seamless electrical contacts. *J. Am. Chem. Soc.* **2019**, *141*, 8928–8936.
47. Seo, J.-E.; Park, E.; Das, T.; Kwak, J.Y.; Chang, J. Demonstration of $PdSe_2$ CMOS Using Same Metal Contact in $PdSe_2$ n-/p-MOSFETs through Thickness-Dependent Phase Transition. *Adv. Electron. Mater.* **2022**, *8*, 2200485.
48. Long, M.; Wang, Y.; Wang, P.; Zhou, X.; Xia, H.; Luo, C.; Huang, S.; Zhang, G.; Yan, H.; Fan, Z.; et al. Palladium diselenide long-wavelength infrared photodetector with high sensitivity and stability. *Adv. Electron. Mater.* **2019**, *13*, 2511–2519.
49. Gu, Y.; Cai, H.; Dong, J.; Yu, Y.; Hoffman, A.N.; Liu, C.; Oyedele, A.D.; Lin, Y.C.; Ge, Z.; Puretzky, A.A.; et al. Two-dimensional palladium diselenide with strong in-plane optical anisotropy and high mobility grown by chemical vapor deposition. *Adv. Mater.* **2020**, *32*, 1906238.
50. Sun, J.; Shi, H.; Siegrist, T.; Singh, D.J. Electronic, transport, and optical properties of bulk and mono-layer $PdSe_2$. *Appl. Phys. Lett.* **2015**, *107*, 153902.
51. Liang, Q.; Wang, Q.; Zhang, Q.; Wei, J.; Lim, S.X.; Zhu, R.; Hu, J.; Wei, W.; Lee, C.; Sow, C.; et al. High-performance, room temperature, ultra-broadband photodetectors based on air-stable $PdSe_2$. *Adv. Mater.* **2019**, *31*, 1807609.
52. Wang, Y.; Pang, J.; Cheng, Q.; Han, L.; Li, Y.; Meng, X.; Ibarlucea, B.; Zhao, H.; Yang, F.; Liu, H.; et al. Applications of 2D-layered palladium diselenide and its van der Waals heterostructures in electronics and optoelectronics. *Nano–Micro Lett.* **2021**, *13*, 143.
53. Liang, Q.; Chen, Z.; Zhang, Q.; Wee, A.T.S. Pentagonal 2D transition metal dichalcogenides: $PdSe_2$ and beyond. *Adv. Funct. Mater.* **2022**, *32*, 2203555.

54. Oyedele, A.D.; Yang, S.; Liang, L.; Puretzky, A.A.; Wang, K.; Zhang, J.; Yu, P.; Pudasaini, P.R.; Ghosh, A.W.; Liu, Z.; et al. PdSe2: Pentagonal two-dimensional layers with high air stability for electronics. *J. Am. Chem. Soc.* **2017**, *139*, 14090–14097.
55. Withanage, S.S.; Khondaker, S.I. Low pressure CVD growth of 2D $PdSe_2$ thin film and its application in $PdSe_2$-$MoSe_2$ vertical heterostructure. *2D Mater.* **2022**, *9*, 025025.
56. Sata, Y.; Moriya, R.; Masubuchi, S.; Watanabe, K.; Taniguchi, T.; Machida, T. n-and p-type carrier injections into WSe_2 with van der Waals contacts of two-dimensional materials. *Jpn. J. Appl. Phys.* **2017**, *56*, 04CK09.
57. Laturia, A.; Van de Put, M.L.; Vandenberghe, W.G. Dielectric properties of hexagonal boron nitride and transition metal dichalcogenides: From monolayer to bulk. *npj 2D Mater. Appl.* **2018**, *2*, 6.
58. Nečas, D.; Klapetek, P. Gwyddion: An open-source software for SPM data analysis. *Open Phys.* **2012**, *10*, 181–188.
59. Zhou, L.; Ge, C.; Yang, H.; Sun, Y.; Zhang, J. A high-pressure enhanced coupling effect between graphene electrical contacts and two-dimensional materials thereby improving the performance of their constituent FET devices. *J. Mater. Chem. C* **2019**, *7*, 15171–15178.
60. Watson, A.J.; Lu, W.; Guimarães, M.H.D.; Stöhr, M. Transfer of large-scale two-dimensional semiconductors: Challenges and developments. *2D Mater.* **2021**, *8*, 032001.
61. Pan, Y.; Rahaman, M.; He, L.; Milekhin, I.; Manoharan, G.; Aslam, M.A.; Blaudeck, T.; Willert, A.; Matković, A.; Madeira, T.I.; et al. Exciton tuning in monolayer WSe_2 via substrate induced electron doping. *Nanoscale Adv.* **2022**, *4*, 5102–5108.
62. Allain, A.; Kang, J.; Banerjee, K.; Kis, A. Electrical contacts to two-dimensional semiconductors. *Nat. Mater.* **2015**, *14*, 1195–1205.
63. Wang, Y.; Chhowalla, M. Making clean electrical contacts on 2D transition metal dichalcogenides. *Nat. Rev. Phys.* **2022**, *4*, 101–112.
64. Lee, K.; Ngo, T.D.; Lee, S.; Shin, H.; Choi, M.S.; Hone, J.; Yoo, W.J. Effects of Oxygen Plasma Treatment on Fermi-Level Pinning and Tunneling at the Metal–Semiconductor Interface of WSe_2 FETs. *Adv. Electron. Mater.* **2023**, *9*, 2200955.
65. Ngo, T.D.; Choi, M.S.; Lee, M.; Ali, F.; Hassan, Y.; Ali, N.; Liu, S.; Lee, C.; Hone, J.; Yoo, W.J. Selective Electron Beam Patterning of Oxygen-Doped WSe_2 for Seamless Lateral Junction Transistors. *Adv. Sci.* **2022**, *9*, 2202465.
66. Moon, I.; Lee, S.; Lee, M.; Kim, C.; Seol, D.; Kim, Y.; Kim, K.H.; Yeom, G.Y.; Teherani, J.T.; Hone, J.; et al. The device level modulation of carrier transport in a 2D WSe_2 field effect transistor via a plasma treatment. *Nanoscale* **2019**, *11*, 17368–17375.
67. Kang, W.–M.; Lee, S.T.; Cho, I.–T.; Park, T.H.; Shin, H.; Hwang, C.S.; Lee, C.; Park, B.–G.; Lee, J.–H. Multi-layer WSe_2 field effect transistor with improved carrier-injection contact by using oxygen plasma treatment. *Solid-State Electron.* **2018**, *140*, 2–7.
68. Li, Q.; Song, J.; Besenbacher, F.; Dong, M. Two-dimensional material confined water. *Acc. Chem. Res.* **2015**, *48*, 119–127.
69. Jain, A.; Bharadwaj, P.; Heeg, S.; Parzefall, M.; Taniguchi, T.; Watanabe, K.; Novotny, L. Minimizing residues and strain in 2D materials transferred from PDMS. *Nanotechnology* **2018**, *29*, 265203.
70. Wang, W.; Clark, N.; Hamer, M.; Carl, A.; Tovari, E.; Sullivan-Allsop, S.; Tillotson, E.; Gao, Y.; de Latour, H.; Selles, F.; et al. Clean assembly of van der Waals heterostructures using silicon nitride membranes. *Nat. Electron.* **2023**, *6*, 981–990.
71. Purdie, D.G.; Pugno, N.M.; Taniguchi, T.; Watanabe, K.; Ferrari, A.C.; Lombardo, A. Cleaning interfaces in layered materials heterostructures. *Nat. Commun.* **2018**, *9*, 5387.
72. Jeon, D.; Kim, H.; Gu, M.; Kim, T. Imaging Fermi-level hysteresis in nanoscale bubbles of few-layer MoS_2. *Commun. Mater.* **2023**, *4*, 62.
73. Zhang, R.; Drysdale, D.; Koutsos, V.; Cheung, R. Controlled layer thinning and p-type doping of WSe_2 by vapor XeF_2. *Adv. Funct. Mater.* **2017**, *27*, 1702455.
74. Park, W.; Pak, Y.; Jang, H.Y.; Nam, J.H.; Kim, T.H.; Oh, S.; Choi, Sung M.; Kim, Y.; Cho, B. Improvement of the bias stress stability in 2D MoS_2 and WS_2 transistors with a TiO_2 interfacial layer. *Nanomaterials* **2019**, *9*, 1155.
75. Ye, M.; Zhang, D.; Yap, Y.K. Recent advances in electronic and optoelectronic devices based on two-dimensional transition metal dichalcogenides. *Electronics* **2017**, *6*, 43.
76. Fei, W.; Trommer, J.; Lemme, M.C.; Mikolajick, T.; Heinzig, A. Emerging reconfigurable electronic devices based on two-dimensional materials: A review. *InfoMat* **2022**, *4*, e12355.
77. Feng, C.; Wu, W.; Liu, H.; Wang, J.; Wan, H.; Ma, G.; Wang, H. Emerging Opportunities for 2D Materials in Neuromorphic Computing. *Nanomaterials* **2023**, *13*, 2720.

Disclaimer/Publisher's Note: The statements, opinions and data contained in all publications are solely those of the individual author(s) and contributor(s) and not of MDPI and/or the editor(s). MDPI and/or the editor(s) disclaim responsibility for any injury to people or property resulting from any ideas, methods, instructions or products referred to in the content.

5.5 List of co-author publications

1. Ivić, J., Petritz, A., Irimia, C.V., Kahraman, B., Kanbur, Y., Bednorz, M., Yumusak, C., **Aslam, M.A.**, Matković, A., Saller, K. and Schwarzinger, C., Schühly, W., Smeds, A.I., Salinas, Y., Schiek, M., Mayr, F., Xu, C., Teichert, C., Osiac, M., Sariciftci, N.S., Stadlober, B., Irimia-Vladu, M., 2022. Pinaceae Fir Resins as Natural Dielectrics for Low Voltage Operating, Hysteresis-Free Organic Field Effect Transistors. Advanced Sustainable Systems, 6(10), 2200234, 1-20.

2. Tran, T.H., Rodriguez, R.D., Cheshev, D., Villa, N.E., **Aslam, M.A.**, Pešić, J., Matković, A. and Sheremet, E., 2022. A universal substrate for the nanoscale investigation of two-dimensional materials. Applied Surface Science, 604, 154585.

3. Pan, Y., Rahaman, M., He, L., Milekhin, I., Manoharan, G., **Aslam, M.A.**, Blaudeck, T., Willert, A., Matković, A., Madeira, T.I. and Zahn, D.R., 2022. Exciton tuning in monolayer WSe_2 via substrate induced electron doping. Nanoscale Advances, 4(23), 5102-5108.

4. Khan, M.Z., Peil, O.E., Sharma, A., Selyshchev, O., Valencia, S., Kronast, F., Zimmermann, M., **Aslam, M.A.**, Raith, J.G., Teichert, C., Zahn, D.R., and Matković, A., 2023. Probing magnetic ordering in air stable iron-rich van-der-Waals minerals. Advanced Physics Research, 2(12), 1-13.

5. Murastov, G., **Aslam, M.A.**, Tran, T.H., Lassnig, A., Watanabe, K., Taniguchi, T., Wurster, S., Nachtnebel, M., Teichert, C., Sheremet, E., Rodriguez, R.D., and Matković, A., 2023. Photoinduced edge-specific nanoparticle decoration of two-dimensional tungsten diselenide nanoribbons. Communications Chemistry, 6(1), 166, 1-9.

6. Coppola, M.E., Petritz, A., Irimia, C.V., Yumusak, C., Mayr, F., Bednorz, M., Matkovic, A., **Aslam, M.A.**, Saller, K., Schwarzinger, C. and Ionita, M.D., Schiek, M., Smeds, A.I., Salinas, Y., Brüggemann, O., D'Orsi, R., Mattonai, M., Ribechini, E., Operamolla, A., Teichert, C., Xu, C., Stadlober, B., Sariciftci, N.S., and Irimia-Vladu, M., 2023. Pinaceae Pine Resins (Black Pine, Shore Pine, Rosin, and Baltic Amber) as Natural Dielectrics for Low Operating Voltage, Hysteresis-Free, Organic Field Effect Transistors. Global Challenges, 2300062, 1-34.

7. Hoffmann, C., Murastov, G., Tromm, J.V., Moog, J.B., **Aslam, M.A.**, Matković, A., and Milovanovic, D., 2023. Electric potential at the interface of membraneless organelles gauged by graphene. Nano Letters, 23, 23, 10796–10801.

8. Gabbett, C., Kelly, A., Coleman, E., Doolan, L., Carey, T., Synnatschke, K., Liu, S., Dawson, A., O'Suilleabhain, D., Munuera, J., Caffrey, E., Boland J., Sofer, Z., Ghosh, G., Kinge, S., Siebbeles, L.D.A., Yadav, N., Vij, J.K., **Aslam, M.A.**, Matković, A., Coleman, J.N., Differentiating the effect of material and junction resistances in nano-networks. *Under review in Nature Communications January 2024*.

MONTANUNIVERSITÄT LEOBEN
www.unileoben.ac.at

M.Sc.
Muhammad Awais Aslam
Auer Von Welsbach Str. 16. Tur 37
9500 Villach

To the Dean of graduate Studies of the Montanuniversitaet Leoben

Declaration of Approval for the Digital Publication of Scientific Theses

I am aware that the thesis entitled "Single Crystalline 2D Material Nanoribbon Networks: Optical and Electrical Properties " will be subject to a plagiarism assessment and may be stored by Montanuniversität Leoben for an unlimited period of time.

I agree that the University Library of Montanuniversität Leoben may publish the thesis open access in the World Wide Web. For embargoed theses this will be done after the embargo expires.

Note: in case you refuse the open access publication in the World Wide Web, the thesis will only be published in printed form (after a possible embargo has expired) in the University Library (dissertations also in the Austrian National Library).

I hereby agree with the open access publication of my thesis on the World Wide Web:

☑ Yes

O No

Date 09.03.2024

Signature Author